

POLITECNICO DI TORINO

Master degree course in Electronic Engineering

Master Degree Thesis

Design and analysis of clocking structures for pNML technology



**Politecnico
di Torino**

Supervisor:

Prof. Mariagrazia GRAZIANO

Co-Supervisors:

PhD. Fabrizio RIENTE

Prof. Marco VACCA

Candidate:

Michele D'AMARO

Academic year 2020/2021

Abstract

For more than 30 years CMOS technology has led the electronic scenario by means of the constant scaling of transistor sizes but according to the International Technology Roadmap of Semiconductors (ITRS) CMOS scaling is now approaching its physical limits and economical limits. In this scenario alternative technologies are studied to overcome the limitations of charge-based technologies.

One promising and interesting “Beyond CMOS” technology listed in ITRS is Nano-Magnet Logic (NML). This technology offers several advantages: inherent non-volatility, radiation hardness, low power dissipation, ultra-high density data storage and processing giving new possibilities in the design of logic circuits, like the possibility to mix logic and memory in the same device. NML uses single domain nanomagnets for logic computations and the magnetization can be in-plane (iNML) or out-of-plane (or perpendicular, pNML). The only two possible states of the magnetization vector represent the binary logic states “0” and “1” and single-domain nanomagnets interact with magneto-static field coupling to propagate the information. To guarantee this, an external magnetic field is applied to the nanomagnet that is used like a signal clock, generated by an on-chip inductor.

The goal of this thesis work is to characterize a possible structure based on pNML to extract all the figures of merit and the parameters useful for more complex circuits.

A first part describes the NML theory and the state-of-art of the current research giving a glimpse to basic logic gates like NAND and NOR gates whose functionality has already been demonstrated experimentally. The principle of working is explained, highlighting the crucial parameters in the design of this technology.

In the second part the structure is simulated and optimized through the COMSOL Multiphysics software and the extracted data are studied in MATLAB. Three soft-magnetic cladding materials with different perpendicular magnetic anisotropy (PMA) are compared via parametric analysis and an estimate for power consumption is given in order to make the structure suitable to be used as a model in a “black box” approach for future works. More complex structures are analyzed for more applications. The results show that clocking of pNML devices in the MHz frequency range with on-chip inductors is feasible.

Contents

List of Figures	III
List of Tables	VII
1 Introduction	1
1.1 Basic fields	2
1.2 Ampere’s law	3
1.3 Forms of magnetism	4
1.4 Hysteresis loop	6
1.5 Soft magnetic materials	7
1.6 Goals of the thesis	8
2 NanoMagnet Logic	10
2.1 Historical background	10
2.2 Working principle	11
2.2.1 Nanomagnetic logic	12
2.2.2 Perpendicular nanomagnetic logic	14
2.3 State-of-the-art	16
3 Methodology	22
3.1 Software	22
3.2 Geometry	22
3.3 Materials	27
3.4 Interface	28
3.5 Mesh	31
3.6 Study	31
4 Start of simulations	32
4.1 From 2D to 3D	32
4.2 Material choice	40
4.3 Parametric analysis	42
4.4 Cell field	43

5	Structure design	44
5.1	Array structures	44
5.2	Horizontal array	45
5.2.1	Two wires array	45
5.2.2	Three wires array	48
5.2.3	Five wires array	53
5.3	Vertical Array	54
5.3.1	Two wires array	54
5.3.2	Four wires array	60
6	Characterization	64
6.1	Frequency and cladding	64
6.2	Interlayer dielectric	68
6.3	pNML thickness	70
6.4	pNML area	72
7	Conclusions	78
	Bibliography	80
	Appendix	A
	From 2D to 3D	A
	-B-H curves	A
	-Field of 2D structure	C
	-3D analysis	D
	Material choice	G
	Parametric analysis	H
	Cell field	I
	Two wires array	J
	Array structures	K
	Frequency and cladding	L

List of Figures

1.1	Paramagnetic order (Wikipedia)	5
1.2	Ferromagnetic order (Wikipedia)	5
1.3	Antiferromagnetic order (Wikipedia)	6
1.4	Hysteresis loop [1]	6
1.5	Eddy currents representation[2]	8
2.1	Several basic elements with QCA [1]: a) Quantum cell, b) wire, c) inverter, d) fanout and e) majority gate	12
2.2	States and coupling for the iNML implementation [3]	13
2.3	iNML complete clock system [4]	14
2.4	Schematic of logic and signal propagation [5]: a) "1" and "0" logic, b) Wire and c) Signal propagation in wire	15
2.5	Copper wires [6]	16
2.6	First clock phase with both the wires excited	17
2.7	Second clock phase with only the right wire excited.	17
2.8	Global strain: a) 3D structure and b) Top view	18
2.9	Stairs-type global strain clocking scheme	18
2.10	Simulation results with global strain clocking scheme	18
2.11	Spin Hall effect clocking [7]: a) SHE physics and b) Current pulse with 3 magnets	19
2.12	Voltage-induced clocking scheme [8]: a) 3D structure and b) 4 disks Clocking scheme	20
2.13	On-chip meander clocking scheme [9]: a) Zoom on the slit and b) Top view	21
3.1	pNML domain: a) View in 2D and b) View in 3D	23
3.2	pNML+wire domains: a) View in 2D and b) View in 3D	23
3.3	pNML+wire+dielectric domains: a) View in 2D and b) View in 3D	24
3.4	pNML+wire+dielectric+cladding domains: a) View in 2D and b) View in 3D	24
3.5	pNML+wire+dielectric+cladding+air domains: a) View in 2D and b) View in 3D	25
3.6	Cut plane	26
3.7	Reference cell	26

3.8	Interlayer dielectric	27
3.9	Periodic Boundary Conditions: a) Magnetic Insulation and b) Perfect Magnetic Conductor	29
3.10	Boundaries for Magnetic Insulation	30
3.11	Boundaries for Perfect Magnetic Conductor	30
4.1	Structure of on-chip clocking inductor from [9]:(a) Zoom cross-section and (b) Top view	32
4.2	2D structure	33
4.3	B-H curves of soft magnetic materials	33
4.4	Perpendicular magnetic induction across the pNML region	34
4.5	Top view of 3D structure	35
4.6	3D view of the structure	35
4.7	3D view of the field	35
4.8	3D field at $l = 120\mu m$	36
4.9	3D field at $l = 200\mu m$	36
4.10	Cutline along x axis	36
4.11	Cutline along y axis	36
4.12	Comparison between different lengths: a) along x and b) along y	37
4.13	Comparison between structures: a) before shape modification and b) after shape modification	38
4.14	3D field distribution without the shape modification	38
4.15	3D field distribution with the shape modification	38
4.16	Comparison between 1D fields: a) before shape modification and b) after shape modification	39
4.17	Structure with straight wire	40
4.18	Structure with real wire	40
4.19	Comparison between structures: a) before wire modification and b) after wire modification	40
4.20	Top view of reference cell	41
4.21	Half cutline along x axis	41
4.22	Comparison between soft magnetic materials with same current	41
4.23	Comparison between different spacing widths	42
4.24	Field of the cell structure: a) along x and b) along y	43
5.1	Horizontal array with bottom wire: a) 3D view and b) Top view	45
5.2	Field along y axis of horizontal array with bottom wire	46
5.3	Horizontal array with top wire: a) 3D view and b) Top view	47
5.4	Field along y axis of horizontal array with top wire	47
5.5	Complete horizontal array with $80\mu m$ additional wires	48
5.6	Field of complete horizontal array with $80\mu m$ additional wires: a) along x and b) along y	49
5.7	Complete horizontal array with $200\mu m$ additional wires	49

5.8	Field of complete horizontal array with 200um additional wires: a) along x and b) along y	50
5.9	Comparison between structure with one wire and 3 wires: a) along x and b) along y	51
5.10	Structure with additional wires at the original position	52
5.11	Structure with additional wires at the new position	52
5.12	Comparison between fields with different position of additional wires: a) along x and b) along y	52
5.13	Complete horizontal array with 5 wires	53
5.14	Comparison between fields with different number of additional wires: a) along x and b) along y	53
5.15	3D view of array structure along z	54
5.16	Internal view of array structure with 2 wires	54
5.17	2D view of array structure	55
5.18	2D view of cell structure	55
5.19	Comparison between fields with the array structure with the normal cladding: a) along x and b) along y	56
5.20	3D view of array structure with flat cladding	56
5.21	2D view of array structure with flat cladding	56
5.22	Comparison between fields with the array structure with the flat cladding: a) along x and b) along y	57
5.23	3D view of array structure with shaped cladding	57
5.24	2D view of array structure with shaped cladding	57
5.25	Comparison between fields with the array structure with the shaped cladding: a) along x and b) along y	58
5.26	3D view of array structure with supershaped cladding	59
5.27	3D view of array structure with shaped cladding	59
5.28	2D view of array structure with supershaped cladding	59
5.29	2D view of array structure with shaped cladding	59
5.30	Comparison between fields with the array structure with the super-shaped cladding: a) along x and b) along y	59
5.31	3D view of array structure shaped cladding with 4 wires	60
5.32	Internal view of array structure with 4 wires	60
5.33	2D view of array structure with shaped cladding with 4 wires	61
5.34	Comparison between fields with the array structure with the shaped cladding 4 wires: a) along x and b) along y	61
5.35	3D structure with super shaped cladding 4 wires: a) from left and b) from right	62
5.36	2D view of array structure with shaped cladding 4 wires	62
5.37	2D view of array structure with super shaped cladding 4 wires	62
5.38	Comparison between fields with the array structure with the super shaped cladding 4 wires: a) along x and b) along y	63

6.1	Frequency analysis with $t_{cl} = 1\mu m$: a) along x and b) along y	65
6.2	Cladding thickness reduction t_{cl} : a) $1\mu m$ and b) $0.5\mu m$	65
6.3	Frequency analysis with $t_{cl} = 0.5\mu m$: a) along x and b) along y	66
6.4	Frequency analysis with $t_{cl} = 0.25\mu m$: a) along x and b) along y	66
6.5	Frequency analysis with $t_{cl} = 0.125\mu m$: a) along x and b) along y	67
6.6	Comparison of different cladding thicknesses at $300MHz$ with the same current: a) along x and b) along y	67
6.7	Comparison of different cladding thicknesses at $300MHz$ with the same field: a) along x and b) along y	68
6.8	Thickness of interlayer dielectric t_{il}	69
6.9	Decreasing of interlayer thickness: a) along x and b) along y	69
6.10	Increasing of interlayer thickness: a) along x and b) along y	70
6.11	Further increasing of interlayer thickness: a) along x and b) along y	70
6.12	Thickness of pNML t_{pnml}	71
6.13	Cutlines along z	71
6.14	Comparison of different heights along z of the pNML thickness: a) along x and b) along y	72
6.15	Comparison of different heights along z of the pNML thickness with $50mT$: a) along x and b) along y	72
6.16	pNML area with w_s and l	73
6.17	Comparison of different widths: a) along x and b) along y	73
6.18	Comparison of different widths with $50mT$: a) along x and b) along y	74
6.19	Decreasing of different lengths: a) along x and b) along y	75
6.20	Decreasing of different lengths with $50mT$: a) along x and b) along y	75
6.21	Increasing of different lengths: a) along x and b) along y	76
6.22	Increasing of different lengths with $50mT$: a) along x and b) along y	76
6.23	Final comparison before and after characterization: a) along x and b) along y	77

List of Tables

3.1	Parameters of the structure	27
3.2	Parameters of the cladding materials	28
4.1	Current values for 50 mT for all the materials	42
5.1	Comparison of values between OneWire and ThreeWires	51
5.2	Comparison of values between ThreeWires and SuperDense	52
5.3	Comparison of values between ThreeWires and FiveWires	54
5.4	Comparison of values between OneWire and ShapedCladding	58
5.5	Comparison of values between OneWire and SuperShapedCladding	60
5.6	Comparison of values between OneWire and SuperShapedCladding4Wires (SSC4)	63
5.7	Comparison of values between SuperShapedCladding4Wires (SSC4) and SuperShapedCladding4WiresEco (SSC4Eco)	63
6.1	Parameters for the characterization	64
6.2	Comparison of different thicknesses	68
6.3	Comparison of different widths	74
6.4	Comparison of different lengths decreasing	75
6.5	Comparison of different lengths increasing	76
6.6	Comparison of values before and after characterization	77

Chapter 1

Introduction

In 1965 Gordon Moore predicted to the Electronics magazine that the number of transistors on a chip would roughly double every year. The continuous improvement in the development of integrated circuits (ICs) made him right. Since then, Moore's Law has been the driving force for down-scaling of device dimensions and interconnecting wires, bringing along the positive impacts of higher integration densities, lower power consumption and increased performance.

However, nowadays it is getting more and more difficult to maintain the scaling trend with regard to both, physical and material limitations as well as economic profitability [10, 11]. It is true that through several innovations (e.g. Strain, High-k+Metal Gate, TriGate (FinFET) [12, 13, 14]) this boundary has been repeatedly moved forward. In any case, the physical limit of scaling is inevitable, making it necessary to think about the future "beyond CMOS". Looking for solutions, two main approaches are pursued: the investigation of new technologies and three-dimensional (3D) integration.

The first approach contains a new requirement on information processing technologies. Not only continual miniaturization should be enabled, but a new form of computational architecture must be accomplished, where logic and memory are combined in a single device [15]. Magnetic materials can provide both features: a remanent magnetization state serving as memory and a stray field, which can be exploited for interaction between magnetic, ultra small-scaled unities to perform logic operation. Here, perpendicular Nanomagnetic logic (pNML) proves as a very promising candidate for beyond-CMOS technology [16].

The second approach concerns the 3D integration of CMOS circuits. The full use of the third dimension may provide the longed for solutions due to better device scalability and improved packing density [11]. Furthermore, in 2007 the ITRS roadmap [17] predicted 3D integration as a key technique to overcome the so-called "wiring crisis" [1]. This involves with the complex wiring of shrinking transistors and the increasing transistor number on chip.

This thesis work shows that it is possible to combine both approaches and to realize 3D integrated pNML. As magnetic stray fields act in all three dimensions, this attribute can be exploited to propagate magnetic signals not only in the horizontal direction but also in the vertical direction. Furthermore, no wiring is needed, because signal propagation and computing are done by magnetic fields.

1.1 Basic fields

In this section some basic notions of magnetism will be given. For the description of the magnetic phenomena two fundamental field quantities are required: the magnetic field \mathbf{H} [A/m or Oe] and the magnetic flux density \mathbf{B} [T or Wb/m^2]. The relation between \mathbf{H} and \mathbf{B} in vacuum is:

$$\mathbf{B} = \mu_0 \mathbf{H} \quad (1.1)$$

The permeability μ_0 amounts to $4\pi \cdot 10^{-7} \left[\frac{T \cdot m}{A} \right]$. \mathbf{B} is a fundamental field in Maxwell's equations, which is created by currents or time-varying electric fields. \mathbf{H} is an auxiliary field in Maxwell's equations, which is created by magnetic dipoles, where the poles of the dipole themselves are the sources of field [1]. Inside these, the relation between \mathbf{B} and \mathbf{H} changes:

$$\mathbf{B} = \mu_0 (\mathbf{H} + \mathbf{M}) \quad (1.2)$$

where \mathbf{H} has 4 possible contributions: current due to free charges in the material, an external applied field, the time-varying electric field and the demagnetization field and \mathbf{M} stands for magnetization vector per unit volume and takes into account that the intrinsic magnetic moments (spins) of the bound electrons line up on average in a certain direction.

Diamagnetic and paramagnetic materials possess no inherent magnetic moment, but a magnetization \mathbf{M} can still be evoked by the excitation with the field \mathbf{H} . For these kind of materials, the relation between \mathbf{M} and \mathbf{H} is linear:

$$\mathbf{M} = \chi_m \mathbf{H} \quad (1.3)$$

where χ_m is the magnetic susceptibility, a dimensionless proportionality constant that quantifies the degree of magnetic polarization (magnetization) of the material following the application of a magnetic field. Substituting \mathbf{M} in (1.2) gives:

$$\mathbf{B} = \mu_0 (1 + \chi_m) \mathbf{H} = \mu_0 \mu_r \mathbf{H} \quad (1.4)$$

where μ_r is called relative permeability and depends on the investigated material. In ferromagnetic materials like cobalt or nichel, the relation between \mathbf{M} and \mathbf{H} is non-linear, showing a hysteretic behavior. This behavior is discussed later on.

1.2 Ampere's law

The law states that the integral along a closed line ∂S of the magnetic field \mathbf{B} is equal to the algebraic sum of the electric currents I_i concatenated to ∂S multiplied by the magnetic permeability constant of the vacuum μ_0 :

$$\oint_{\partial S} \mathbf{B} \cdot d\mathbf{r} = \mu_0 \sum_i I_i = \mu_0 I \quad (1.5)$$

The concatenated currents have positive sign if their verse and that of the integration line are coincident, otherwise they are negative. In particular, since the circulation of \mathbf{B} is not zero, the magnetic field is not conservative.

Local form

Applying Stokes's theorem to the circulation of \mathbf{B} gives:

$$\oint_{\partial S} \mathbf{B} \cdot d\mathbf{r} = \int_S \nabla \times \mathbf{B} \cdot d\mathbf{S} \quad (1.6)$$

And since

$$I = \int_S \mathbf{J} \cdot d\mathbf{S} \quad (1.7)$$

where the density current \mathbf{J} is not zero only in the part of surface S intersected by the line, the Ampere's law becomes:

$$\int_S \nabla \times \mathbf{B} \cdot d\mathbf{S} = \mu_0 \int_S \mathbf{J} \cdot d\mathbf{S} \quad (1.8)$$

By equating the integrands the local form of Ampere's law is obtained:

$$\nabla \times \mathbf{B} = \mu_0 \mathbf{J} \quad (1.9)$$

Non-stationary case

The relationship (1.9) holds only in the stationary case, as shown by applying the divergence to both members. For the former one has $\nabla \cdot (\nabla \times \mathbf{B}) = 0$ and so, also $\nabla \cdot \mathbf{J}$ must be zero. But the continuity equation:

$$\nabla \cdot \mathbf{J} = -\frac{\partial \rho}{\partial t} \quad (1.10)$$

forces $\nabla \cdot \mathbf{J}$ to be zero only when $\frac{\partial \rho}{\partial t}$ is zero, that is in the stationary case. So this gives:

$$0 = \nabla \cdot \mathbf{J} + \frac{\partial \rho}{\partial t} = \nabla \cdot \left(\mathbf{J} + \epsilon_0 \frac{\partial \mathbf{E}}{\partial t} \right) \quad (1.11)$$

where the term $\epsilon_0 \frac{\partial \mathbf{E}}{\partial t}$ is called displacement current density. Including this one in (1.9) the Ampere-Maxwell law is:

$$\nabla \times \mathbf{B} = \mu_0 \left(\mathbf{J} + \epsilon_0 \frac{\partial \mathbf{E}}{\partial t} \right) \quad (1.12)$$

This expression shows how also the temporal variation of an electric field is the source of a magnetic field.

1.3 Forms of magnetism

Diamagnetism

In these materials the magnetization has the opposite direction to the magnetic field, so these materials are "repelled" but this effect is weak and it is very often canceled by the other mechanisms. Diamagnetism is observed in those materials whose molecules do not possess their own magnetic dipole moment and typical substances of this type are water and some metals such as mercury, gold, copper. The relationship between the vectors \mathbf{H} and \mathbf{M} is proportionally linear: $\mathbf{M} = \chi_m \mathbf{H}$. The relative magnetic permeability μ_r is less than or equal to 1 and therefore the magnetic susceptibility $\chi_m = \mu_r - 1$ is a negative constant: this is the reason why diamagnetic materials are "repelled" by the magnetic field, that is \mathbf{M} and \mathbf{H} have opposite direction [18].

Paramagnetism

Paramagnetism manifests itself with a magnetization having the same direction of the external field applied to the paramagnetic material itself.

It is observed in those materials such as aluminum, oxygen, calcium and platinum [18] whose molecules have their own magnetic dipole moment but do not retain magnetization in the absence of an applied external field (fig.1.1).

Magnetic susceptibility χ_m paramagnetic materials, in this case, is a pure positive number.

Ferromagnetism

Ferromagnetism is the property of some materials (iron, cobalt and nickel [18]) to get a very intense magnetization under the action of an external magnetic field and to remain magnetized for a long time when the field is removed (fig.1.2). Above a critical temperature T_c , called the ferromagnetic Curie temperature, the magnetization vanishes and the material becomes paramagnetic.

The relative magnetic permeability of the material χ_m is not constant as the fields

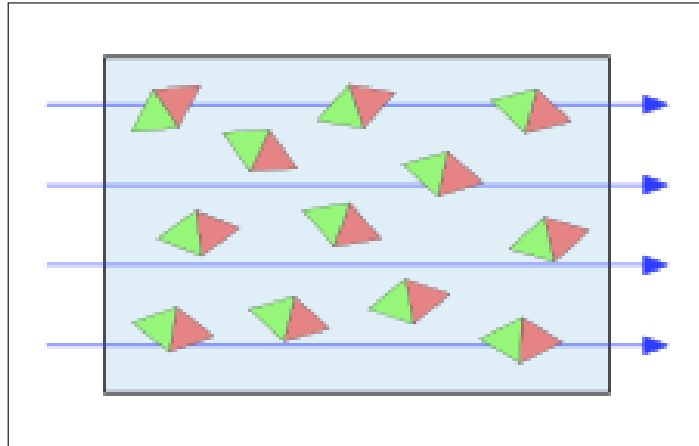


Figure 1.1: Paramagnetic order (Wikipedia)

vary, like it occurs in diamagnetic and paramagnetic materials: the relationship between the magnetic induction field \mathbf{B} and the magnetic field \mathbf{H} is therefore neither linear nor univocal. The law followed by the relationship between these vectors can be represented with an hysteresis loop.

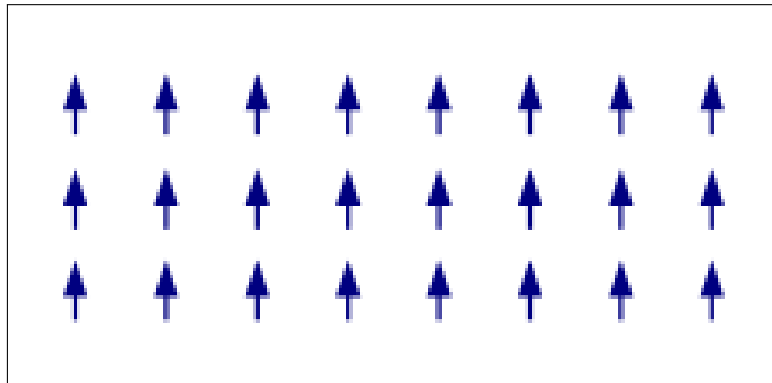


Figure 1.2: Ferromagnetic order (Wikipedia)

Antiferromagnetism

Antiferromagnetism is a characteristic property of some materials such as manganese, chromium, hematite. Contrary to what happens for ferromagnetic materials, the interaction between the atoms is such as to create a configuration of minimum energy when the spins are antiparallel, fig.1.3. The magnetization of these materials, below a certain temperature called Néel, and in the absence of an external magnetic field, is practically zero. Even when there is an external magnetic field, magnetic dipoles tend to maintain the antiferromagnetic arrangement.

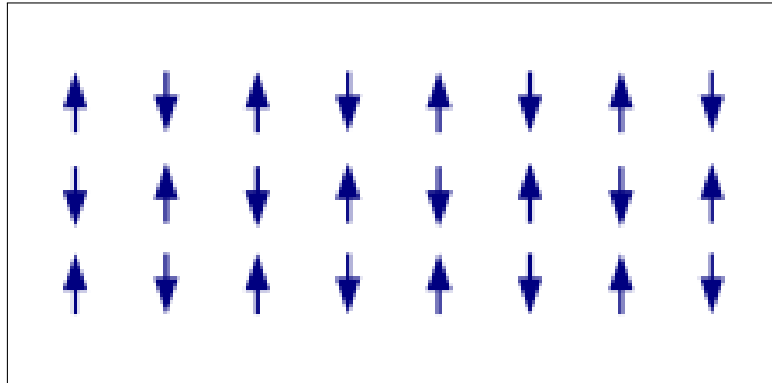


Figure 1.3: Antiferromagnetic order (Wikipedia)

1.4 Hysteresis loop

Larger magnets are divided into regions called domains. The total magnetization of the ferromagnetic specimen is a vector sum of the magnetic moments of each domain. Therefore the absolute value of the magnetization can have values between zero (the magnetic moments may cancel each other out, called demagnetized state) and a maximum value, called saturation magnetization M_S where the magnetic moments of each domain are aligned in one direction forming a single domain. In order to achieve the saturation magnetization an external field has to be applied. This process is strongly nonlinear therefore the relation between the magnetization and the applied field is described by the hysteresis loop, shown in fig.1.4.

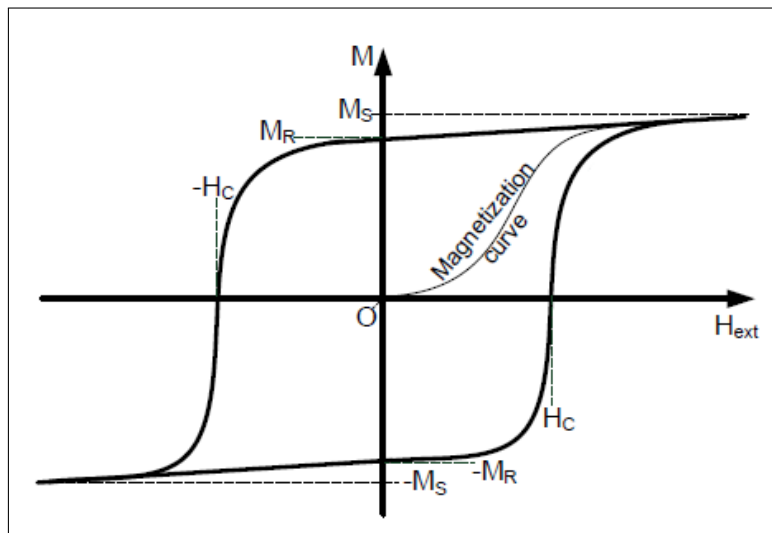


Figure 1.4: Hysteresis loop [1]

Assuming that the material is initially demagnetized, the curve starts at point O. By applying a magnetic field the magnetization grows until all magnetic moments align in the direction of H_{ext} and the maximum magnetization (M_S) is reached (in fig.1.4 this process is indicated by the 'Magnetization curve'). Reducing the field again to zero, the magnetization adopts higher values than before. This effect can be traced back to the irreversibility of the domain formation process. At zero field a remainder of the magnetization remains, called remanence magnetization M_R . To achieve zero magnetization again, the external field has to be further reduced to the value $-H_C$. This field, where $M = 0$, is called coercive field. A further reduction leads to the negative saturation of the specimen. Increasing the external field to positive values again, the behaviour is the same of the first curve.

The shape of the hysteresis curve may vary. The higher the energy required to change the magnetization direction, the higher is H_C . Furthermore the direction of the applied field in relation to the inherent magnetization direction of the investigated specimen modifies the form of the hysteresis.

The phenomenon of hysteresis is the result of two different effects: rotation of magnetization and changes in size or number of magnetic domains. In general, the magnetization varies (only in direction and not in magnitude) across a magnet, but if the magnets are sufficiently small, it does not. In these single-domain magnets, when a magnetic field is applied the magnetization responds by rotating.

1.5 Soft magnetic materials

The main advantage of the soft magnetic materials is that they can be easily magnetised and demagnetised [19]. They are used primarily to improve and/or channel the flux produced by an electric current applied to the structure.

The main parameter, often used as a figure of merit for soft magnetic materials, is the relative permeability μ_r , which says how quickly the material responds to the applied magnetic field. The other main parameters are the coercivity H_c , the electrical conductivity σ and the saturation magnetization M_S . The types of applications for soft magnetic materials are of two types: DC and AC.

For DC applications the main consideration for material selection is given to the permeability.

For AC applications the important consideration is how much energy is lost in the system based on its hysteresis loop.

Core loss

Core loss is extremely important in soft magnetics because it represents inefficiency so it is highly struggled by the designer. It is the result of three major components: hysteresis loss, eddy current loss and anomalous loss.

Hysteresis loss results from the fact that, once magnetized, it is not possible to recover all the energy when it is demagnetized. The wider and taller the hysteresis loop, the more hysteresis loss a material has so it is proportional to the area within the normal loop. The area of the loop is determined by H_c , M_s (saturation magnetization) and the shape of the loop. Hysteresis losses can be reduced by the reduction of the intrinsic coercivity, so that there is a consequent reduction in the area contained within the hysteresis loop.

Eddy current loss is the result of small circulating currents that are induced in the magnetic material when the flux carried by the magnetic material changes (fig.1.5). The amplitude of these small currents depends on the magnitude of the applied magnetic field and on the electrical resistivity of the material. Eddy current losses can be reduced by decreasing the electrical conductivity of the material or by laminating the material, which has an influence on overall conductivity and is also important because of skin effects at higher frequency.

Anomalous losses can be reduced by having a completely homogeneous material, within which the motion of domain walls will not be hindered.

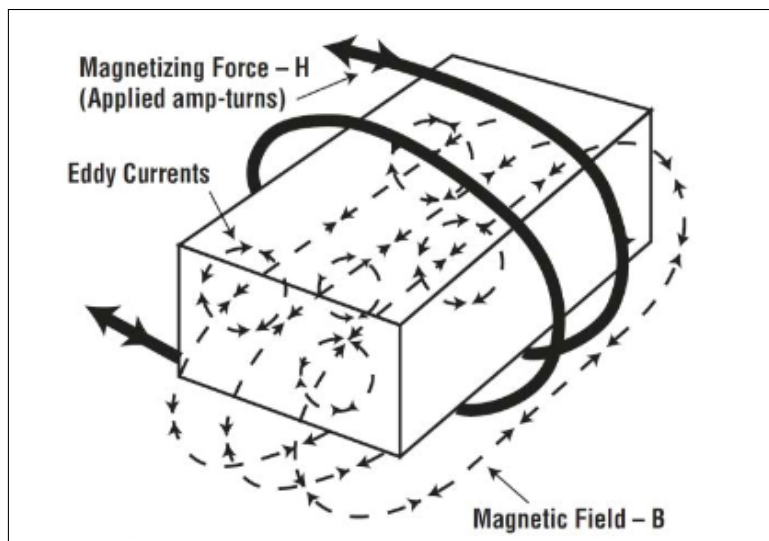


Figure 1.5: Eddy currents representation[2]

1.6 Goals of the thesis

The goal of this thesis work is, starting from the results in literature, to characterize a possible structure based on pNML technology, extracting all the figures of merit and the parameters useful to better understand the limits of this technology and then to improve them with the final scope to reach the performances of the CMOS technology and even overcome them.

In the first 2 chapters the aim is to give to the reader a theoretical background about the fundamentals of magnetism (if not known) and the technology itself, respectively 1 and 2, so that it is possible to have all the tools to understand this research area.

The chapter 3 aims to explain the strategies used in this work to simulate the structure in terms of software features and physical conditions to apply at the boundaries to mimic areal 3D world.

The chapter 4 goal was to give a first analysis and consequently extract a correct model of this device for several points of view: geometry, material, field amplitude and so on.

To improve this model in chapter 5 it was profoundly changed following the idea "same current, more field" to obtain a lower power consumption.

In the last chapter, 6, a real range of usability for every parameter was desired in order to have the full control of the structure knowing its limits.

Chapter 2

NanoMagnet Logic

The goal of this chapter is to give the basics notions about the pNML technology. Its historical evolution is discussed to be aware of the reasons that led to its development, then the principle of working is investigated with the aim to understand which is the critical element of the circuit and where the research is going to improve it, so that finally the actual state-of-the-art is presented to see which are the solutions implemented.

2.1 Historical background

The story of Magnetic Logic starts basically in the 1950s and 60s. An all-Magnetic Logic exploited ring cores enclosed by several input and output coils to provide logic operation. Other approaches were propagating domain walls (DW) and magnetic bubbles (Magnetic Bubble Logic, in [20]) in magnetic thin films. However, in terms of size, speed and costs of such magnetic components they were passed by the emerging transistors, MOSFET and ICs technology, and then by on-chip memory technologies too. Therefore, researches on Magnetic Logic devices stopped until the year 2000. Thereby, the discovery of the spin transfer torque (STT) for the integration of magnetic structures and the development of modern manufacturing equipment have been very important.

The new lifeblood of Magnetic Logic devices is based on the exploration of Quantum Cellular Automata (QCA). In this device the Coulomb force between electrons is used to perform logic operations from bistable quantum cells. Furthermore, the design of simple QCA devices like wires, inverter, AND / OR gates and later majority gates has been postulated [21, 22]. The promising features of QCA are: no interconnects, ultra-high-density and low-power dissipation. However, challenges in the uniformity of cell, fabrication problems and above all the required cryogenic temperature of operation delayed the explosion of this technology.

The implementation of magnetic materials for QCA led to the Magnetic Quantum Cellular Automata (MQCA) and was the breakthrough of QCA and thus the beginning of NanoMagnetic Logic (NML). MQCA use small magnetic dots (later called magnets) as quantum cells which interact through their magnetic stray field. The magnetization state of the magnetic dots becomes a state variable and is stable at room temperature. In [23] the magnetic majority gate is proposed as basic building block for Magnet Logic, including electrical integration and clocking of these magnetic circuits. After some time, MQCA gained more and more interest. Afterwards, the fabrication of the majority gate was finally demonstrated in 2006 using magnets with in-plane magnetization [24] and this was a big step forward in the development of NML. The advantages of QCA combined with the benefits of magnetic devices (non-volatility, stable operation at room temperature) are unique among the beyond-CMOS devices.

Magnetic Logic using propagating domain walls has been rediscovered in the form of Domain Wall Logic (DWL). Here, logic operations are performed by shifting different configurations of DWs in a structured in-plane material [25]. However, the sensitivity to geometric imperfections make these devices rather unsuitable as beyond-CMOS technology. But nowadays, DWL received growing interest again because of the application of magnetic materials with PMA in DW-based devices. The magnetization vector can be oriented in plane (in-plane Nanomagnetic Logic (iNML)) or out of plane (or perpendicular) (perpendicular NML, pNML). In principle, the first proposal of Magnetic Logic using magnets with out-of-plane magnetization was in 2002. However, the challenging fabrication of the suggested structures led to an forgetfulness of this technology until the year 2007. In 2007, Becherer et al. [26] from the Technische Universität München (TUM) started to investigate the Magnetic Logic using Cobalt (Co)/Platinum (Pt) magnets with out-of-plane magnetization. At the beginning of their researches, they explored the possibility to order phenomena in Focused Ion Beam (FIB) patterned Co/Pt multilayer films with PMA. The demonstration of magnetic ordering in FIB patterned wires of field-coupled Co/Pt magnets arrived in 2009 [27].

In recent years, research on Magnetic Logic devices has gained increasing interest in both iNML and pNML due to the scaling problem of conventional CMOS technology. In addition to the general features of NML (or MQCA), pNML provides independence from the shape and tunable switching behavior of the magnets and signal flow control. One of the milestones for the evolution of pNML was the demonstration of the majority gate using Co/Pt magnets with PMA [28].

2.2 Working principle

Magnetic devices are mainly used for data-storage applications, that is, the information is stored in the magnetization state of ferromagnetic materials. Other

advantageous aspects are the built-in non-volatility [29], the radiation hardness and the low power operation. In the last years, several implementations have been proposed. This thesis focuses on a different magnetic logic device, which exploits magnetic field coupling for processing logic operation, namely NML and in particular its 3D implementation, the pNML.

This section is organized as follows: the first part discusses all aspects of NML, namely, where it comes from and its features, the second part covers the differences with the pNML implementation of this technology.

2.2.1 Nanomagnetic logic

The origin of NML can be seen in the introduction of the QCA approach. QCA exploits interactions based on Coulomb force between quantum cells to transmit the signal and perform logic operation. The quantum cells are cells where only two discrete stable states are allowed encoding the binary states 0 and 1. Signal flow is achieved by bringing such cells together in the immediate vicinity and with the help of an external electric field as clock. The interacting cell system moves to reach the energetically lowest state, bringing forward the correct information for each cell, given fixed inputs. Consequently signal transmission and computation do not depend on metallic wiring or electric currents, resulting in improvement of energy efficiency [30, 31]. The notation quantum is because the interactions are based on the quantum effect of electrons. In fig.2.1 a series of basic elements is shown. The cell consists of 4 quantum dots located in a square. Each cell is composed by 2 electrons, which align in diagonal by means of their Coulomb repulsion.

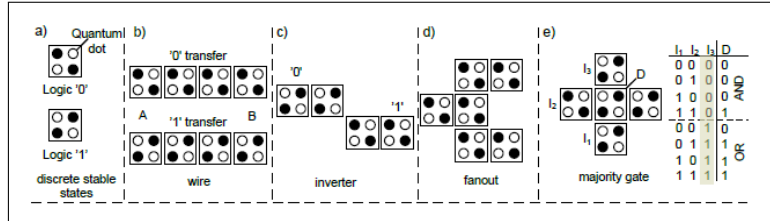


Figure 2.1: Several basic elements with QCA [1]: a) Quantum cell, b) wire, c) inverter, d) fanout and e) majority gate

In the year 2000, Cowburn and Welland [32] developed an MQCA so instead of using electrons they exploited the magnetization direction of nanoscaled ferromagnetic islands as bistable variable. The circular-shaped islands were strong enough to affect the magnetization state of the next neighbor cell. As regards the clock, an oscillating magnetic field was used as supplied energy to the system and as a clock. The experiment proved that propagation was due to field interaction between close ferromagnetic islands. Csaba et al. proposed pillar-shaped magnets, with the easy axis of the magnetization vector perpendicular to the film-plane [23]. The

simulations confirmed that the same displacement of the magnets as proposed in the QCA approach enabled majority decision and consequently logic operation but it turned out to be hard to fabricate. Therefore, a year later, Parish and Forshaw [33] proposed to use magnets with magnetization vector orientated in the film-plane, like in fig.2.2.

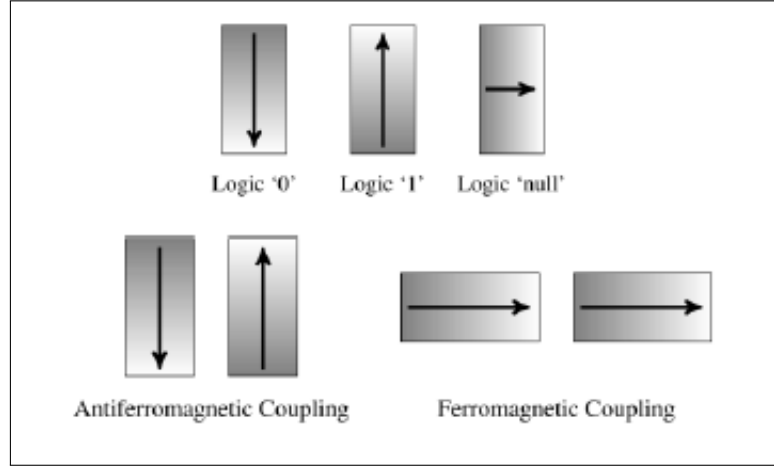


Figure 2.2: States and coupling for the iNML implementation [3]

Information flow in iNML is represented by magnetization vector propagation in a chain of field-coupled nanomagnets. The magnetization direction can represent a logical "1" (magnetization vector upwards) or a logical "0" (magnetization vector downwards). The magnetization switching is composed by two steps: nucleation of a domain wall (DW) and DW propagation in order to reverse the magnetization of the entire magnet. The nucleation spot is called Artificial Nucleation Center (ANC) and is located on one edge of a nanomagnet; it is determined by local ion irradiation, which locally reduces the energy required to change the magnetization. The position of the ANC ensures directed propagation and not vice versa (no opposite signal flow) and, with the DW motion, it is driven by a global alternating clocking field generated by an on-chip coil. The clocking cycle comprises one positive and one negative field pulse. In an initialized system (when all magnets are orientated to the lowest energy state) the signal advances by one half of a clocking cycle at time. The maximum clocking frequency is defined by the time needed for nucleation of the domain, DW propagation velocity and the size of the magnet. The clocking field amplitude H_{clock} is defined by the coercivity field H_c of the magnet, field in which a magnet is switched with 50% probability. Every magnet of a circuit is sensitive to one close magnet which imposes a stray field, this is the magnetic coupling $H_{coupling}$ and can hinder or allow the magnetization reversal of the following nanomagnet. Consequently, the effective field H_{eff} acting on the ANC is an overlap of an alternating clocking field and the coupling field. This can be written with the

following equations [34]:

$$H_{clock} = H_c(p = 50\%) \quad (2.1)$$

$$H_{eff} = H_{clock} \pm H_{coupling} \quad (2.2)$$

Actually, for an NML, the switching of a nanomagnet from state "1" to state "0" is favored if an intermediate state is present. When an external field is applied the previous state is erased and when the field is released, an input can more easily force the new magnetization state to the neighboring magnet (fig.2.3).

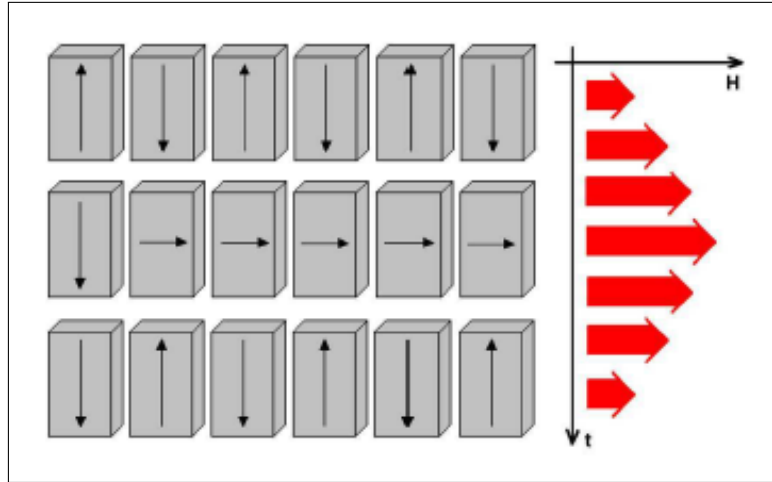


Figure 2.3: iNML complete clock system [4]

Such definition of the clocking field assures the correct signal propagation through the whole magnetic circuit.

It can be seen that the fabrication of in-plane NML was a significant step in the history of NML. Nonetheless, the experiments revealed imperfections and constraints of this technology, which led to look for more attractive implementations. A more promising approach in terms of reliability and design freedom is the pNML with Co/Pt magnets.

2.2.2 Perpendicular nanomagnetic logic

This thesis work deals with pNML, which is considered as the most interesting implementation of NML [35]. It uses nanomagnets with PMA, which interact among them by antiferromagnetic field-coupling because, like the iNML, the magnetization state of the magnets is a state variable and is encoded with logic "1" (magnetization up) or logic "0" (magnetization down). As before, the switching of the magnets is composed by the nucleation in the ANC and the DW propagation through the whole magnet. The energy needed to switch the magnets comes from the external alternating clocking field, perpendicular to the plane.

Logic operation in pNML with Co/Pt magnets can be explained on the basis of a magnetic chain, shown in fig.2.4 since it is the same idea, mentioned before.

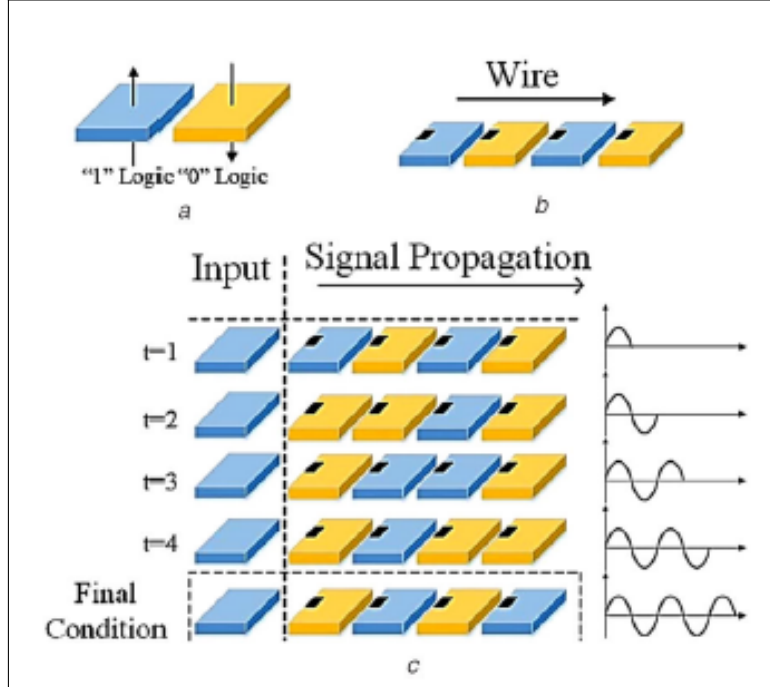


Figure 2.4: Schematic of logic and signal propagation [5]: a) "1" and "0" logic, b) Wire and c) Signal propagation in wire

As already mentioned, magnets of a pNML system, due to the strong crystalline anisotropy, possess a switching threshold [36], which needs to be overcome by an external clocking field. This clocking field provides all the required basic energy, so that magnetic ordering is ruled by the energy coming from the coupling fields of magnets, solely. The clocking concept can be explained on the basis of a magnetic wire, depicted in fig.2.4. All magnets in the wire, but the input magnet, are left-side irradiated, so the ANC is placed on the left and therefore they are governed by the dipole field of their left neighbor. When a clocking pulse H_{clock} is applied in the down direction, the coupling field of the input magnet forces the second magnet in the antiparallel state (i.e. down state). The magnetization state of all subsequent magnets is not known. Since the input magnet is not irradiated, it possesses a very high inherent switching field and the clocking pulse does not affect it [37]. Then a positive clocking pulse is applied. Now, the coupling field of the second magnet try to force the third magnet to switch in the 'up' state. It should be noted that the second magnet can not switch back because the coupling field of the input magnet is equal in direction to the external field and impedes the switching of the second magnet. To sum up, the correct switch of one subsequent magnet can be guaranteed after every clocking pulse.

Nowadays [38, 39], clocking of pNML devices is realized by on-chip coils, therefore, the clocking field is at the same time power supply and internal clock. The on-chip clock concept is the most critical aspect that prevents pNML from becoming a low-power technology. Indeed, the biggest contribution to the total power dissipation is due to the on-chip inductor, since the clocking concept concerns the speed and the operational reliability of NML circuitry. Novel approaches like propagating DWs or the Spin Hall effect are studied for ultra-low power on-chip clocking and some will be investigated in the following section.

But first, in order to be considered a serious beyond-CMOS technology candidate, electrical integration and so compatibility to CMOS has to be analyzed. Electrical I/O structures can be: modern STT devices or more classical current wires (as input) and hall sensing devices (as output). Modern STT devices exploit the Giant MagnetoResistance (GMR) or Tunnel MagnetoResistive (TMR) effect, which are both convenient to read (output) and write (input) the magnetization state. Such devices use the magnetoresistive effect between ferromagnetic layers with in between a nonmagnetic conductive layer (GMR) or a tunnel barrier (Magnetic Tunnel Junction (MTJ), in particular, based on the alignment of the magnetizations in both ferromagnetic layers, the electric resistance of the structure is either low (parallel) or high (antiparallel).

2.3 State-of-the-art

Several solutions for the generation of clock are investigated in this section.

Copper wires

In several works based on [6], [40] and [41] the copper wire carries a constant current that generates a magnetic field around it. The presence of the ferrite yoke surrounding the wire from three sides confines the magnetic flux close to the wire. The nanomagnets are placed on the top and are separated from the copper wire by a thin oxide layer. The nanomagnets are placed on the top and are separated from the copper wire by a thin oxide layer, fig.2.5.

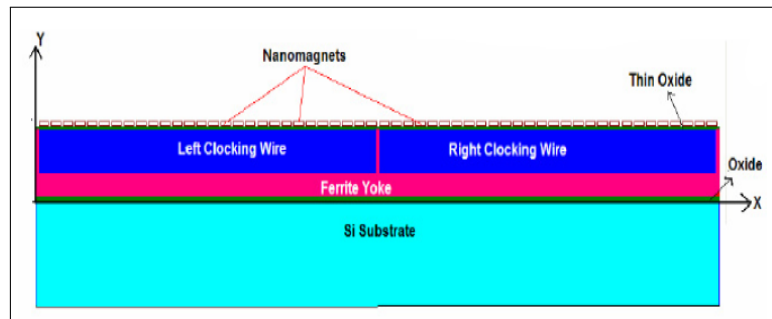


Figure 2.5: Copper wires [6]

During the first phase of the clock (fig.2.6), both wires are excited and all the nanomagnets experience an high magnetic field that nulls the state of the magnets. In the second clock phase (fig.2.7), only the right wire is excited and therefore only the nanomagnets on the right side are affected by an high magnetic field and are nulled. The left nanomagnets relax to the ground state and the magnetization state is determined by the their input on the left. The power dissipated by the structure was too high so it was abandoned.

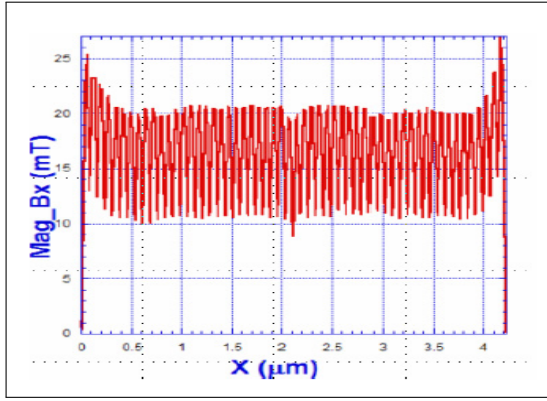


Figure 2.6: First clock phase with both the wires excited

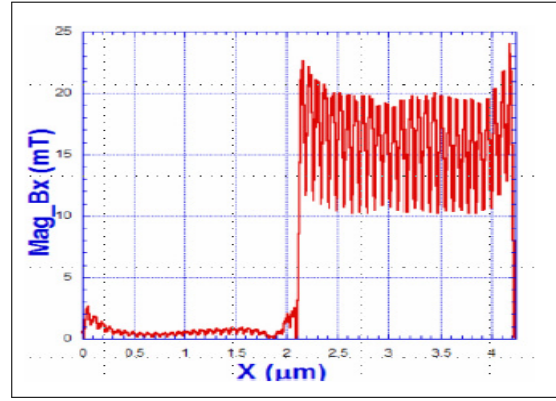


Figure 2.7: Second clock phase with only the right wire excited.

Global strain clocking scheme

A majority logic gate based on a 3-layers structure is proposed in [42], TerfenolD is selected as the magnetic layer and PMN-PT as piezoelectric layer material since it has the higher piezoelectric coefficient and can be construct on Silicon substrate, fig.2.8(a). The fig.2.8(b) shows the top view of majority logic gate which is composed by 3 type A nanomagnets, one type B nanomagnet and one type C nanomagnet, which differ from each other for the width and a variable thickness.

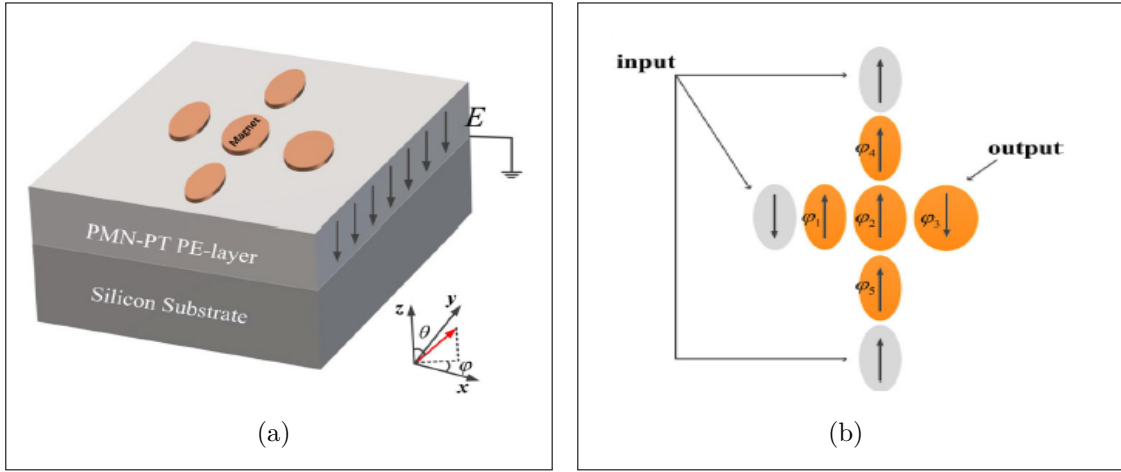


Figure 2.8: Global strain: a) 3D structure and b) Top view

Simulations were performed to obtain the correct size of nanomagnet thickness and hysteresis loops were extracted. Based on those results, a stairs-type global strain clocking scheme was designed, as depicted in fig.2.9, where Stress A, Stress B and Stress C are the stress values used for getting 90° magnetization switching of each type of nanomagnet, respectively. In fig.2.10 the simulation result is shown. Although the correctness of the magnetization, the complex and tricky process to realize such a structure with the piezoelectric material makes the global strain clocking scheme not easily adoptable.

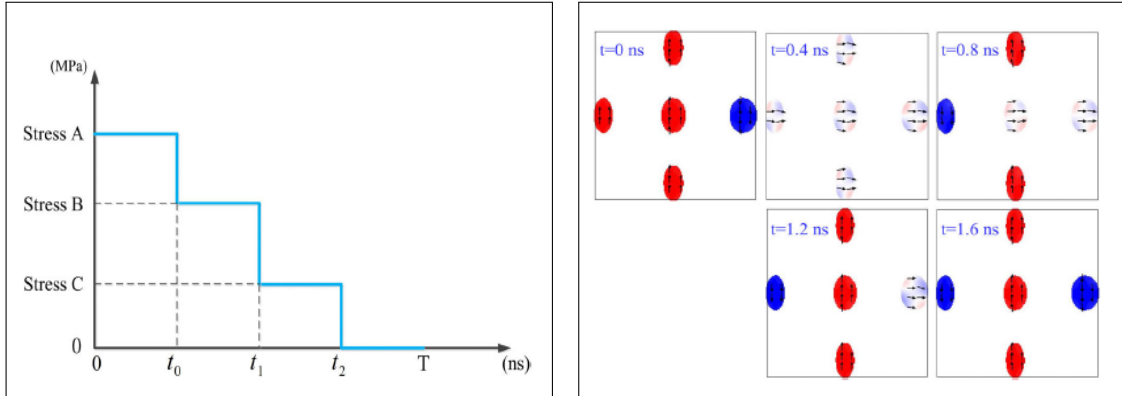


Figure 2.9: Stairs-type global strain clocking scheme

Figure 2.10: Simulation results with global strain clocking scheme

Spin Hall Effect

An interesting solution to avoid a clocking scheme is the exploiting of the so called Spin Hall Effect (SHE). Based on a previous work [43], a chain of 3 perpendicularly

polarized CoFeB nanomagnets on top of a Tantalum wire is built in [7, 44]. As concerns the Spin Hall physics, when an in-plane current flows through a resistive bar made of tantalum, electrons accumulate at the opposite surfaces of the bar (along the z direction) due to their spins of opposite polarities (fig.2.11,a) and this affects a CoFeB magnet placed on top of the tantalum. The CoFeB is a material characterized by a perpendicular magnetic anisotropy. If the influence is strong enough, the magnetization can be in-plane, where it is metastable. Then if the current is switched off, the magnet, from this metastable state, can move to an "up" or "down" state. Fig.2.11(b) shows that an unpolarized current flowing through the wire can control the perpendicular magnetization to a metastable state of all magnets but the input one, since the input magnet is designed not to be affected by the clock pulse. When the current is removed, the magnets would orient themselves in their lowest energy configuration. The problem here is that when the complexity of the circuit grows up and more than some few magnets are considered the SHE is not sufficient to "clock" the entire system.

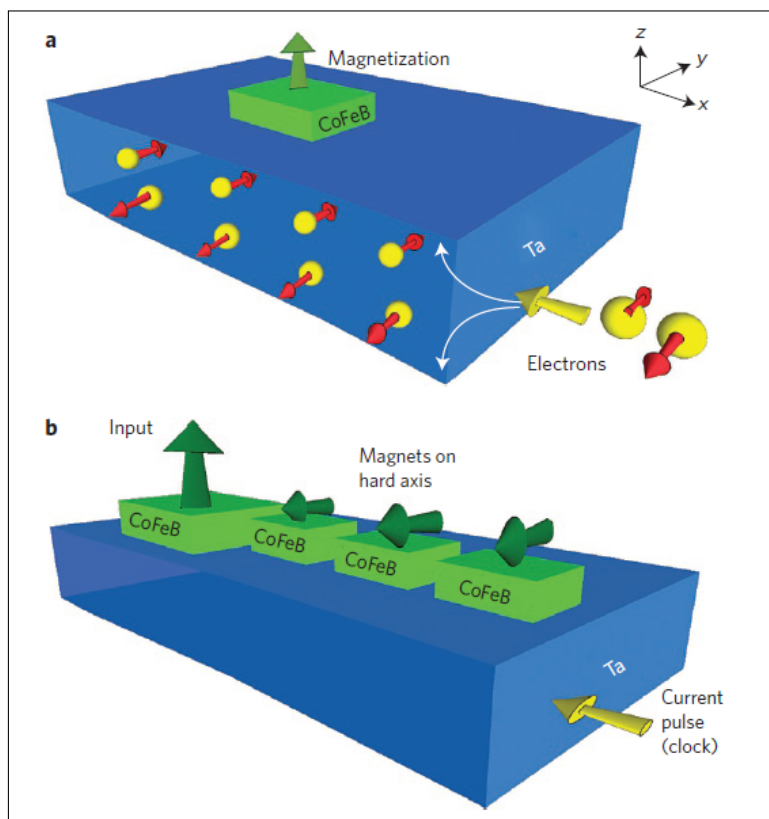


Figure 2.11: Spin Hall effect clocking [7]: a) SHE physics and b) Current pulse with 3 magnets

Voltage-induced strain clocking

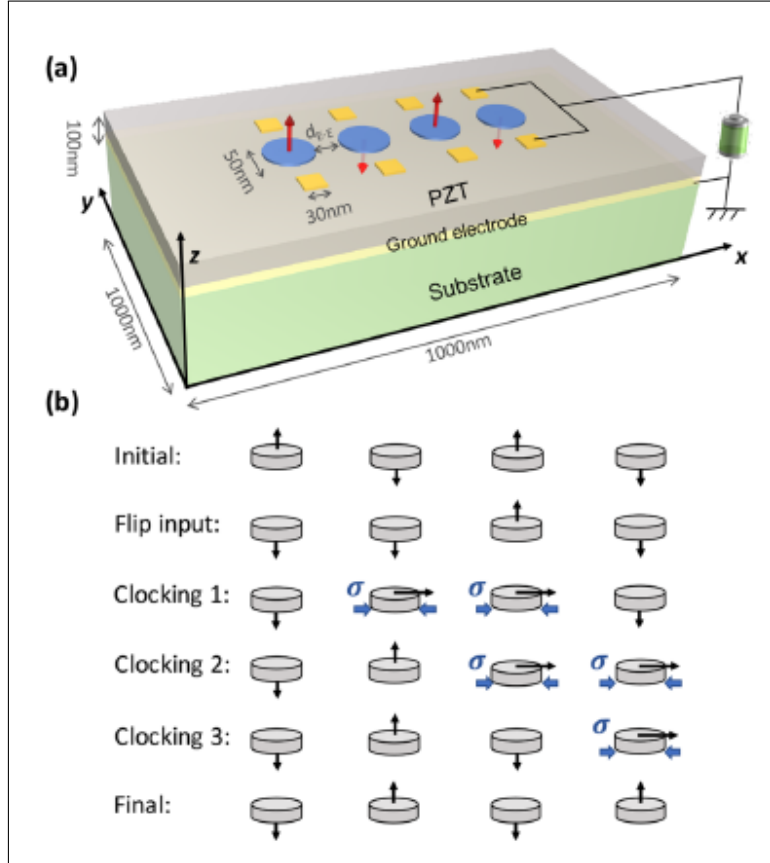


Figure 2.12: Voltage-induced clocking scheme [8]: a) 3D structure and b) 4 disks Clocking scheme

A 4 bit Bennett clocking system for different materials (Ni, CoFeB and Terfenol-D) with PMA is studied in [8]. The device consists of a multiferroic structure with a piezoelectric thin film, placed on a substrate, 4 magnetoelastic disks and ground/-surface electrodes that surround the disks along y . The piezoelectric material chosen is PZT-5H poled along the z direction and its 4 sides and bottom surfaces are mechanically fixed while the bottom surface is electrically grounded. A pair of square electrodes surround along y each disk, fig.2.12(a). Fig.2.12(b) reports information flow. The direction of the perpendicular magnetization M_z is used as coding. At start, a short voltage pulse is used to write new information in disk 1 changing its magnetization. When disk 1 changes its state, disk 2 does not readily update its state because the dipole coupling is not strong enough. Therefore, an additional clocking field is necessary and it is obtained applying the same voltage to disk 2 and disk 3. The so produced voltage-induced strain forces the magnetization to be

in-plane. Then, removing the voltage from disk 2 produces an unstable in-plane magnetic state while disk 3 is still mechanically strained and its magnetization has a much smaller influence on disk 2 compared to disk 1. So, the magnetization of disk 2 aligns with anti-parallel order to the disk 1 and the information in disk 1 is now passed to disk 2. The same follows for the other disks. As for the global strain, the piezoelectric material and in particular the Terfenol-D is not an easy material to simulate so it was not considered.

On-chip meander inductor

A possible efficient geometry for pNML clocking is shown in [9] adapted from [45]. A soft magnetic material layer is deposited so that the pNML is directly realized on top of the lower cladding armor. A dielectric layer is placed under and above the pNML and the current carrying copper wire and finally the top magnetic cladding layer covers the dielectric. Due to the high permeability of the soft magnetic layers, the generated magnetic flux is directed to the slit, the zone where the pNML sees a perpendicular field H_z . Basically, observing the top view the wire presence creates a meander pattern where the pNML is clocked, fig.2.13. This results the most promising solution so it is the one chosen for this thesis.

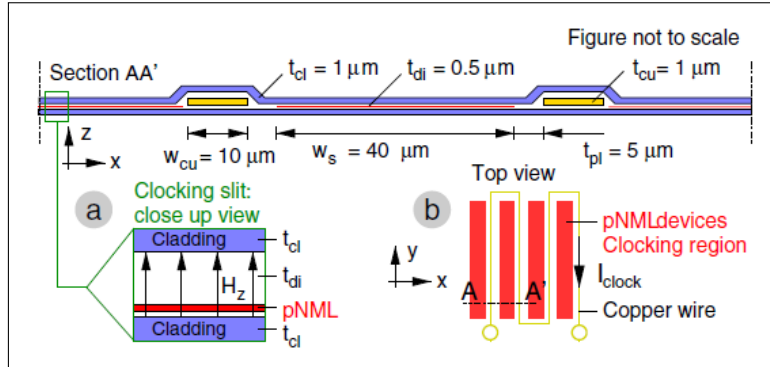


Figure 2.13: On-chip meander clocking scheme [9]: a) Zoom on the slit and b) Top view

Chapter 3

Methodology

In this chapter the focus is on the tools used in this thesis work. Every aspect of the software, from the parameters of the materials to be studied and the geometry building, up to the applied conditions to the structure and the mesh rendering, is discussed in order to ensure clarity of exposure and repeatability of simulations.

3.1 Software

The software selected for this work is COMSOL Multiphysics 5.5, a well-known cross-platform finite element analysis and solver software [46]. It allows for multiphysics simulations merging workflows for electromagnetic, mechanical, fluid, acoustics and chemical applications and more. In particular, all the simulations that will be discussed here, are performed by the AC/DC Module [47].

The AC/DC Module provides an effective environment for simulating AC/DC electromagnetism in 2D and 3D. With this module it is possible to run different types of simulations in an easy-to-use graphical user interface.

The data are then extracted from COMSOL and plotted with MATLAB to compare them.

3.2 Geometry

The definition of the geometry is the first step in the building of the structure. The **Block** and the **Hexahedron** features are used to compose the whole structure, where each block or hexahedron represents a different element of the structure and in COMSOL is called domain. Then to improve the visualization of the different parts and to simplify the modifications, the domains, which refer to the same object (wire, dielectric, etc) and in turn material, are merged by means of **Form composite domains** virtual operation in one single domain. In this way, only few domains without internal lines are present and each one has its own name in the

node **Definitions**. Plus, each dimension of the structure has its own parameter, so that it is easy to see the effects of changing dimensions.

The first domain, around which the structure is built, is the pNML as depicted in fig.3.1 in 2D and in 3D. The central one is twice as wide as the other 2 because it is the only one whole while the lateral ones represent other pNML for larger structures, this is the reason why they are halved. The parameters that define the domain are: width w_s is the spacing width between the 2 parallel sections of the wire from which $10\mu m$ are subtracted to get the width of the pNML along x axis, length l that is the same for all the domains and thickness t_{pnml} .

Then the domain of the wire is added (see fig.3.2). The parameters of the wire are the width w_{cu} and the thickness t_{cu} .

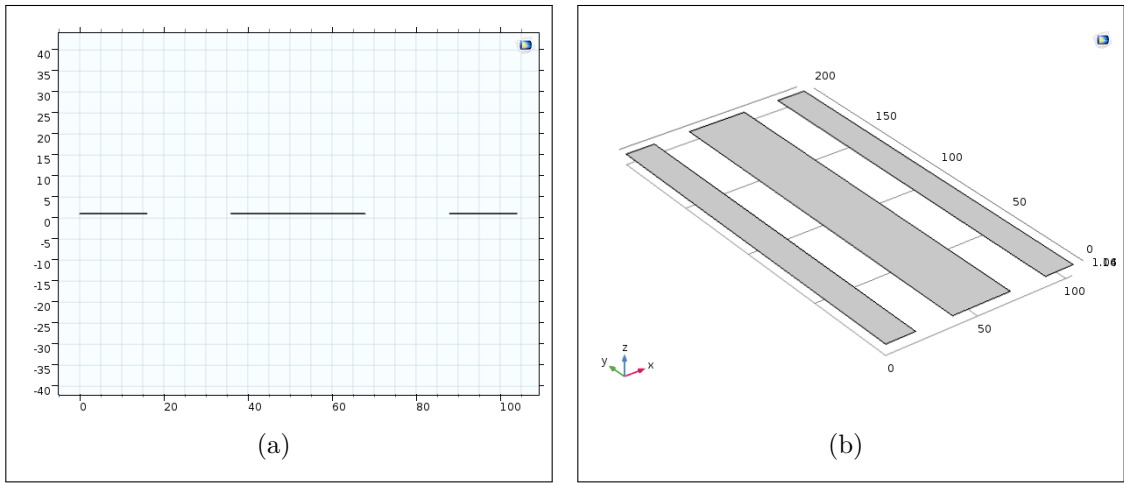


Figure 3.1: pNML domain: a) View in 2D and b) View in 3D

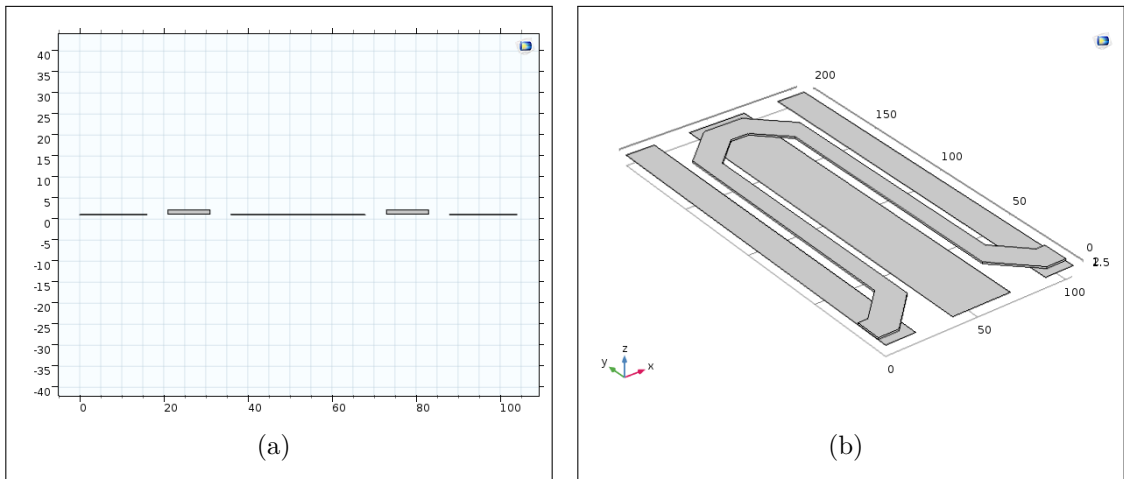


Figure 3.2: pNML+wire domains: a) View in 2D and b) View in 3D

These domains are firstly surrounded in every direction by the dielectric (fig.3.3) and secondly they are sandwiched by the cladding (fig.3.4). The parameters of the dielectric and cladding are: t_{di} , that is the thickness of the dielectric between lower cladding and pNML and between wire and pNML along the z axis; since the structure of dielectric is complex and composed by many parts where the precise single coordinates have to be inserted there is no a reference parameter for each of them, t_{pl} thickness of the dielectric between wire and upper cladding along the z axis and t_{cl} thickness of the cladding.

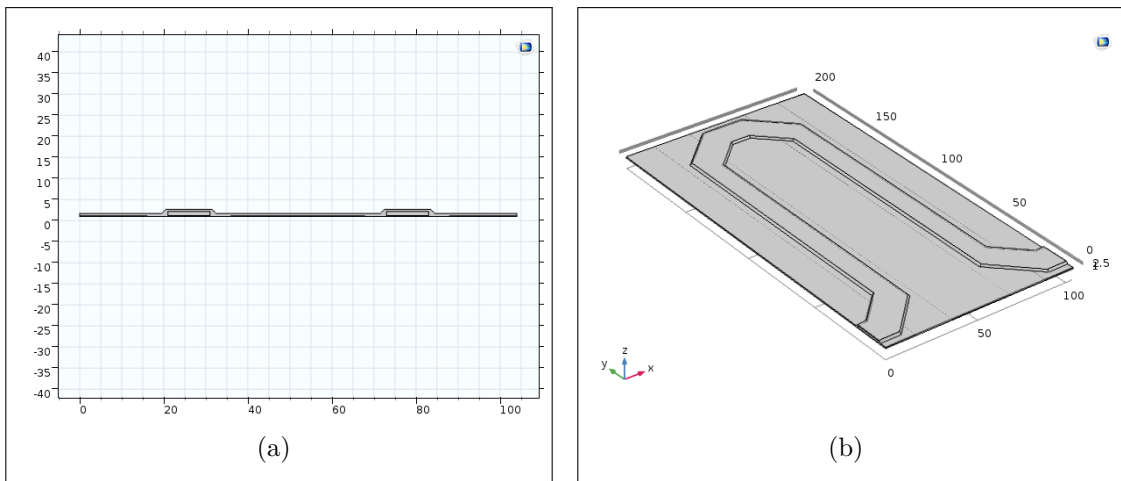


Figure 3.3: pNML+wire+dielectric domains: a) View in 2D and b) View in 3D

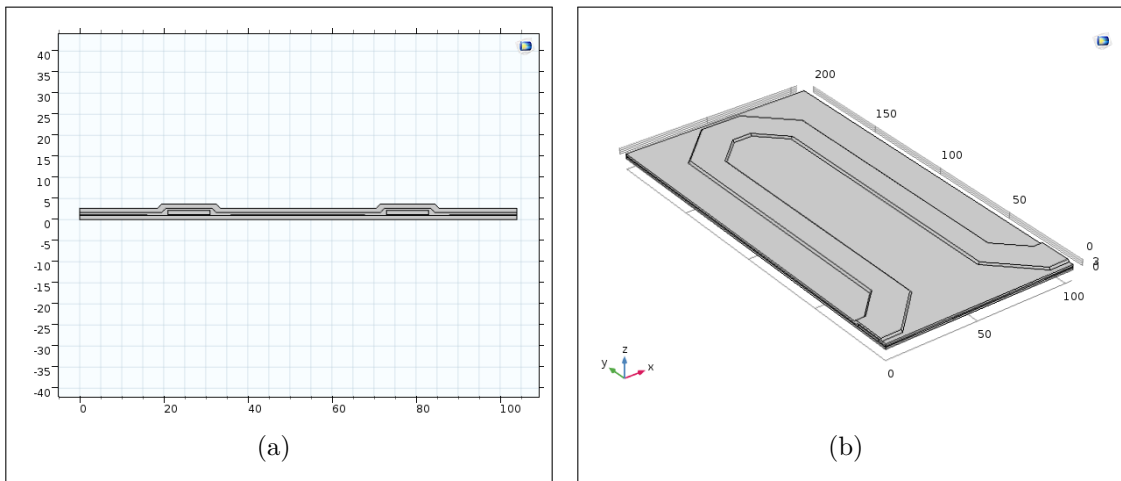


Figure 3.4: pNML+wire+dielectric+cladding domains: a) View in 2D and b) View in 3D

In the end, in transparency in fig.3.5 everything is encapsulated in a domain that

represents the air around the structure with thickness t_{air} . In the first simulations this domain surrounds the structure in all the directions but then, in order to exploit in a better way the symmetry, this air domain was limited to the top and bottom only and removed at the sides. For this reason, as can be seen in 2D view, in the air domain there are 2 small inner layers just at the top and bottom of the domain. These inner layers with thickness t_{inf} are necessary to get what COMSOL calls "infinite elements", i.e. a part of domain that extends to infinity. In this way nothing is present over and under the structure but air. In all the outer faces Periodic Boundary Conditions (PBC) are applied but these will be discussed later.

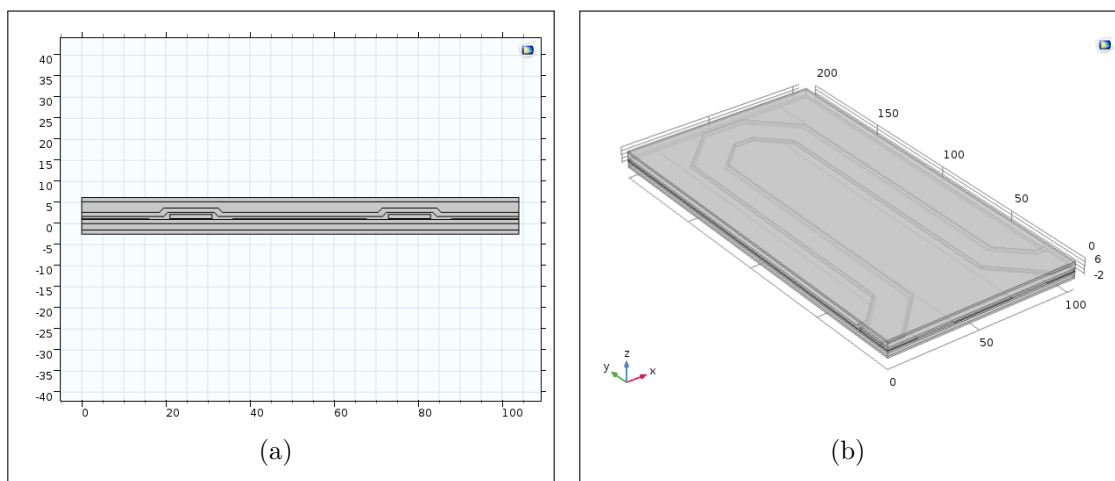


Figure 3.5: pNML+wire+dielectric+cladding+air domains: a) View in 2D and b) View in 3D

In order to simplify the simulations, in a second moment the symmetry of the structure with respect to the y axis was exploited (fig.3.6) so that just one half of this structure is simulated and used as reference cell, fig.3.7. In this way it is possible to understand the behaviour of the whole structure halving the computational cost of the simulations.

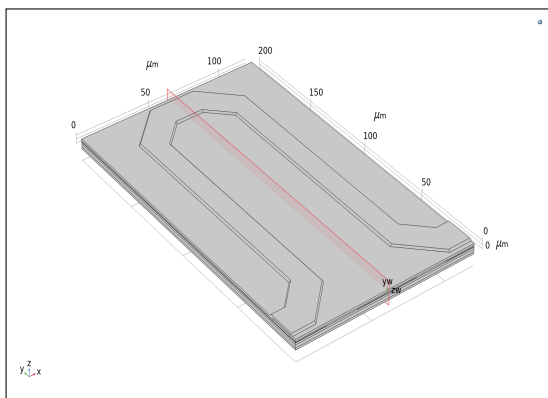


Figure 3.6: Cut plane

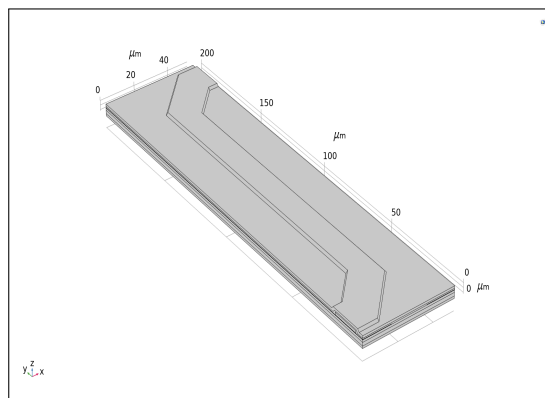


Figure 3.7: Reference cell

The simulations are done for several types of structures and when the structure has wires spread over several floors, between them another domain of dielectric of thickness t_{il} is included that, in this thesis, was called interlayer dielectric as in fig.6.8, where it is possible to note that in the middle of this one there is the pNML. This dielectric is merged with the already existing dielectric in one domain.

The table 3.1 summarizes all the parameters that describe the structure with their values. The following parameters complete the list:

- *corr factor* is an offset factor used to correct the x coordinate of the domains that are close to the point where the horizontal and tilted section of the curves meet, the point in the internal side of the curves. Since this point does not depend on parameters of the structure has become a parameter itself;
- l_{down} and l_{up} are just the lengths of the additional wires when structures with more than one wire are investigated;
- $i0$ is the initial current with which the first simulations were done;
- w is the width of the entire structure.

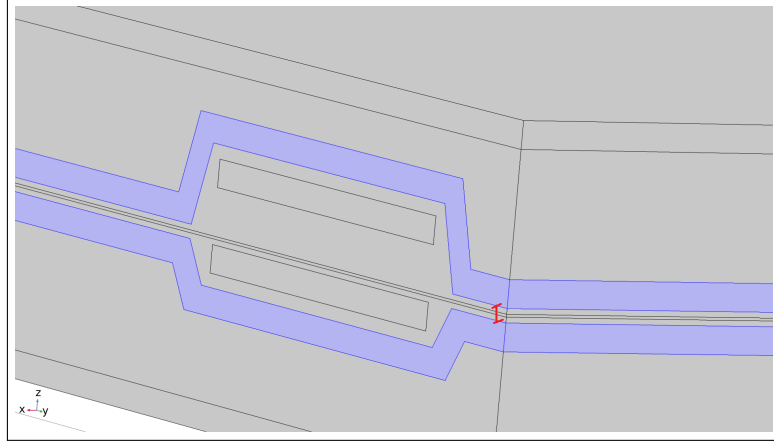


Figure 3.8: Interlayer dielectric

Name	Expression	Value	Description
$corr\ factor$	9.14213562	9.1421	correction factor[um]
i_0	0.0283	0.0283	initial current[A]
l	200	200	structure length[um]
l_{down}	200	200	bottom structure length[um]
l_{up}	200	200	top structure length[um]
t_{air}	2.5	2.5	air domain thickness[um]
t_{cl}	1	1	cladding thickness[um]
t_{cu}	1	1	copper wire thickness[um]
t_{di}	0.05	0.05	dielectric thickness[um]
t_{il}	0.5	0.5	interlayer thickness[um]
t_{inf}	1	1	infinite domain thickness[um]
t_{pl}	$0.5 * t_{cu}$	0.5	planarization dielectric thickness[um]
t_{pnml}	0.1	0.1	pnml thickness[um]
w	$2 * (w_s + w_{cu})$	116	structure width[um]
w_{cu}	10	10	copper wire width[um]
w_s	50	50	spacing width[um]

Table 3.1: Parameters of the structure

3.3 Materials

For the air, dielectric and wire domains the materials are taken directly from the database of COMSOL; respectively air, silicon dioxide (SiO₂) and copper (Cu). The pNML is made by Cobalt and Platinum multilayers (Co/Pt), chosen because

they show a strong Perpendicular Magnetic Anisotropy (PMA), which can be controlled by varying the number or the thickness of both the layers. Furthermore, Co has a strong saturation magnetization and therefore a good interaction of field coupled Co/Pt nanomagnets is obtained. From the fabrication point of view, Co/Pt multilayers deposition techniques are well known and an aspect to underline is the ability to regulate the magnetic anisotropy by Focused Ion Beam (FIB) irradiation. The data are taken from [9].

The materials examined in this work for the cladding are 3: an alloy of Cobalt, Zirconium and Tantalum (chemical symbol CoZrTa), an alloy of Nickel and Iron (chemical symbol NiFe) and an alloy of Nickel, Iron and Molybdenum called Superalloy (SPy). These are soft magnetic materials and they are exploited for their magnetic properties as explained in chapter 1. The CoZrTa and NiFe are described in [9] from which the material data are taken while SPy data come from [48].

In particular, the conductivities and the imaginary components of the relative permeability μ_r are obtained from [9] (where *freq* indicates the frequency) while the real components of the relative permeability μ_r of CoZrTa is obtained from [45], that of NiFe from [49] and that of SPy is computed from the B-H curve extracted from [48]. The table 3.2 summarizes all the parameters of these materials.

Material	Parameter	Value	Unit
CoZrTa	conductivity σ	1010000	S/m
	permeability μ_r (real component)	1000	1
	permeability μ_r (imaginary component)	$2e^{-9} * freq$	1
NiFe	conductivity σ	5000000	S/m
	permeability μ_r (real component)	4500	1
	permeability μ_r (imaginary component)	$2e^{-8} * freq$	1
SPy	conductivity σ	1740000	S/m
	permeability μ_r (real component)	35000	1
	permeability μ_r (imaginary component)	$2e^{-8} * freq$	1

Table 3.2: Parameters of the cladding materials

3.4 Interface

The interfaces in the AC/DC Module form a complete set of simulation tools for electromagnetic field simulations and cover almost all types of problems. In this thesis 2 interfaces are used: the **Magnetic and Electric Fields (mef)** interface and the **Magnetic Fields (mf)** interface.

Magnetic and Electric Fields

The **Magnetic and Electric Fields** interface is used to compute magnetic field and current distributions when the exciting current is driven by an applied voltage because when a current is used as coil excitation, the coil applies an external electric field in the direction of the current flow, computed as:

$$E_e = \frac{V}{L} \quad (3.1)$$

where L is equal to the physics interface thickness d for 2D models and the coil length in 3D models. V is an unknown applied potential and is solved for using an additional equation.

The main node is the **Ampere's Law and Current Conservation**, which adds the equation for the electric potential and magnetic vector potential. It is applied only to the coil, i.e. the domain of the wire.

On the contrary, the **Ampere's Law** node adds just Ampere's law for the magnetic field and provides an interface for defining the constitutive relations. This node is used for all the structure but when it is applied to the domain of the cladding the relationship between the magnetic flux density \mathbf{B} and the magnetic field \mathbf{H} is selected for "Magnetic losses" to describe the relative permeability as a complex quantity: $\mu_r = \mu' + i\mu''$, where μ' and μ'' are the real and imaginary parts, respectively. In this way the losses in the cladding are accounted. When this node is applied to the remaining domains is selected for "Relative permeability" so that the relationship is the linear one 1.4.

At the outer faces of the structure boundary conditions are applied.

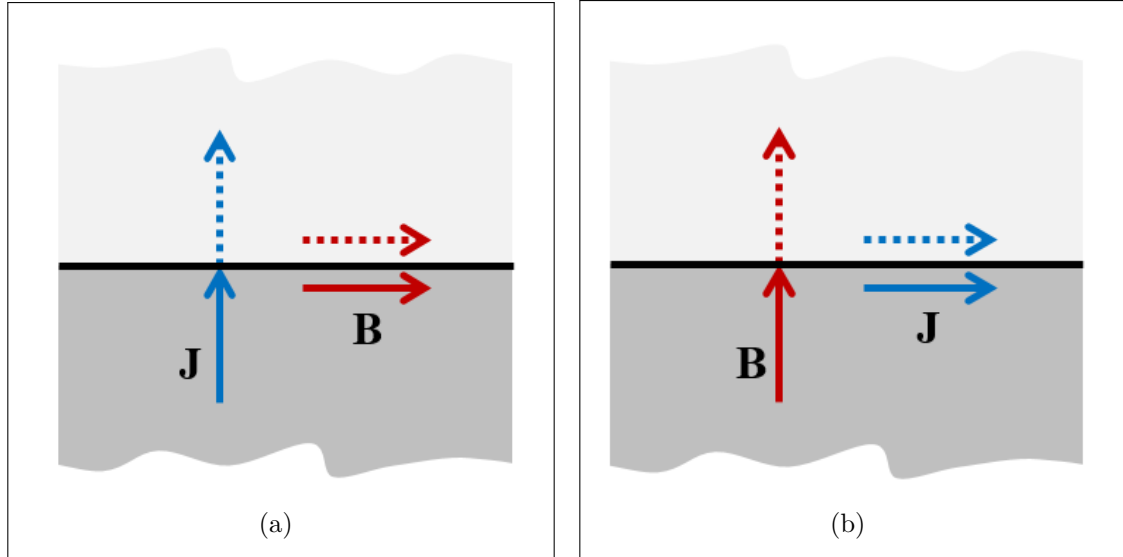


Figure 3.9: Periodic Boundary Conditions: a) Magnetic Insulation and b) Perfect Magnetic Conductor

The **Magnetic Insulation** node is the default boundary condition for the **Magnetic and Electric Fields** interface and it is used for the modeling of a symmetry type boundary condition. The node imposes symmetry for magnetic fields and "magnetic currents" (fig.3.9, a). That is, the magnetic field must be tangential to this boundary and, as a consequence, the current can only flow in the normal direction to the boundary plane. For this reason it is applied to the 4 sides (fig.3.10), because in this way this halved structure can be mirrored through the y axis (but also the x axis if the aim is to repeat the structure in more directions) and give the field of the whole curve. At the begin and the end of the coil the **Terminal** and **Ground** subnodes features are applied, since they provide a boundary or domain condition for connection to external circuits or with a specified voltage or current, and the zero potential, respectively.

The **Perfect Magnetic Conductor** boundary condition, on the other hand, represents a mirror symmetry plane for the current (fig.3.9, b). The current vector will be exactly mirrored beyond the plane and can have no normal component, so the current must flow tangentially. This boundary condition imposes that the magnetic field has no tangential component. This is the reason why it is applied to the 2 boundaries of the infinite elements of the air domain at the top and the bottom (fig.3.11).

With these conditions the current in this structure starts flowing from the **Terminal** node to the **Ground** node of the coil and, through the PBC applied to the lateral planes, comes in another **Terminal** node (it could be of the same coil or another one) to close the loop.

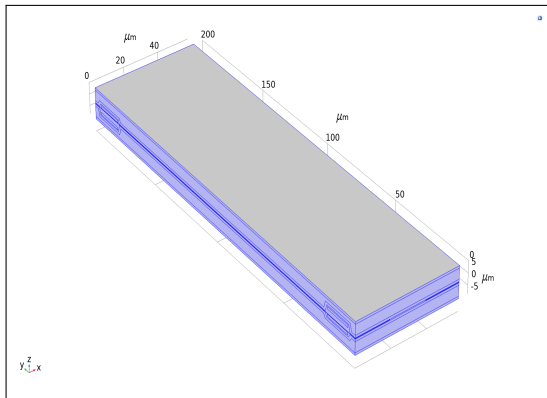


Figure 3.10: Boundaries for Magnetic Insulation

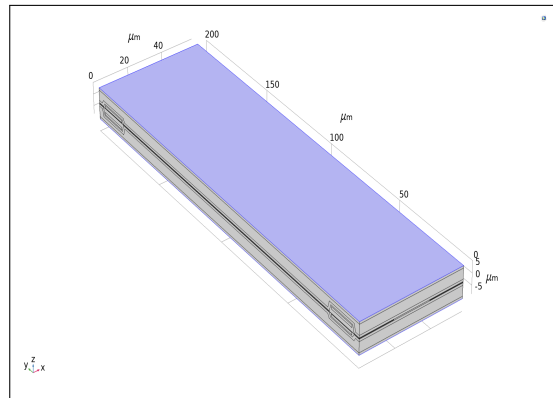


Figure 3.11: Boundaries for Perfect Magnetic Conductor

Magnetic Fields

When the analysis moves to higher frequencies the **Magnetic Fields** interface is more suitable to be used because here the main node is the **Ampere's Law** and

the **Ampere's Law and Current Conservation** node is no longer present. The only change to be considered is that now a new **Coil** node has to be added to manage the coil domain; it is used to model coils, cables and other conductors subject to a lumped excitation, such as an externally applied current or voltage and in this node the **Input** and **Output** subnodes replace the **Terminal** and the **Ground** ones, respectively. The other nodes (therefore including also boundary conditions, etc) are the same and are applied in the same way.

3.5 Mesh

2 nodes are added for the mesh: the **Free Tetrahedral** node to create an unstructured tetrahedral mesh everywhere and the **Swept** node only in the infinite elements domains. For the sizes, "Normal" was chosen for the tetrahedral and "Coarse" for the swept because it is less important what happens there so the computational cost can be reduced.

3.6 Study

Finally, the **Frequency domain** node is used for the simulation, where it is possible to set the frequency and choose between the interfaces if more than one are present. The only difference between the 2 interfaces analyzed above is that the **Magnetic Fields** needs a previous node called **Coil Geometry Analysis**. This node is used to compute the current flow in 3D models. This is a preprocessing step that must be solved before solving the main study step (for example, the Frequency domain). The boundary conditions are the **Input** and **Output** subnodes.

Chapter 4

Start of simulations

In this chapter a first analysis is reported. The starting point is a research based on [50], [9] and [45] from which the thesis work moves up.

In this research a possible geometry for efficient pNML clocking is shown. The idea is an on-chip inductor where, because of the high permeability of the soft magnetic layers, the magnetic flux is guided to the zone where the pNML is exposed to a perpendicular field H_z . Basically, the copper wire forms a meander pattern generating pNML clocking regions of equal size, which could be tens of micrometer wide and several millimeters long, fig.4.1.

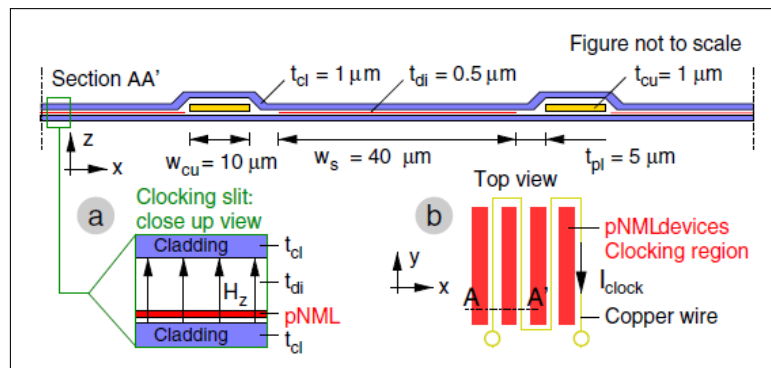


Figure 4.1: Structure of on-chip clocking inductor from [9]:(a) Zoom cross-section and (b) Top view

4.1 From 2D to 3D

The first structure simulated is the same of fig.4.1, a 2D structure reported in fig.4.2 where the cladding domain is highlighted. Every aspect regarding the geometry and applied PBC was already explained, therefore the fig.4.3 shows the B-H curves for the soft magnetic materials studied. The slope in the graph corresponds to the

permeability, so it is the lowest for CoZrTa, moderate for NiFe and the highest for SPy.

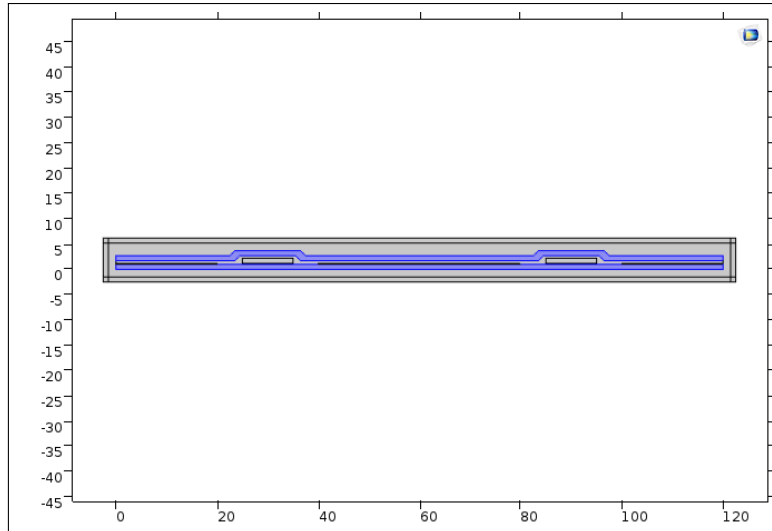


Figure 4.2: 2D structure

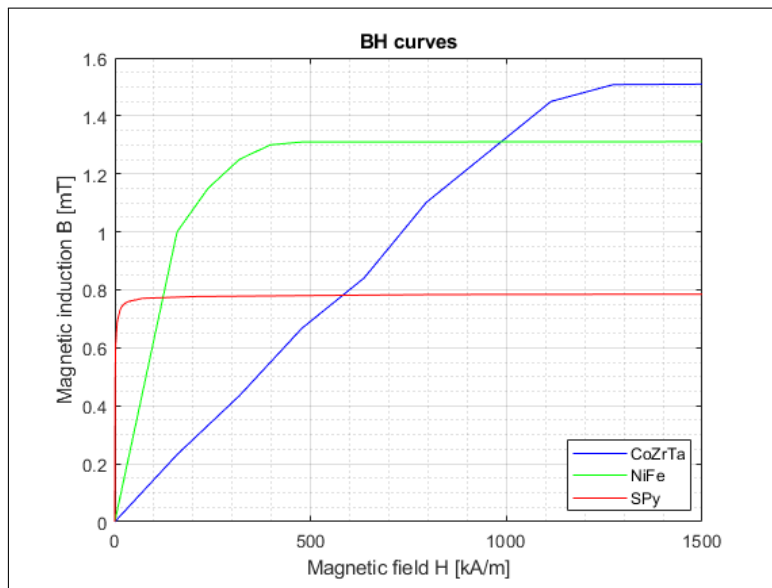


Figure 4.3: B-H curves of soft magnetic materials

The generated magnetic induction B_y across the pNML region (x direction in fig.4.1) for the 3 soft magnetic materials is plotted in fig.4.4. The fields data are computed for a current density of $J = 2 \cdot 10^9 A/m^2$ from which is computed

the value of i_0 at $1MHz$ and $50MHz$ frequency. As expected, SPy which has the highest μ_r gives the most homogeneous field amplitude.

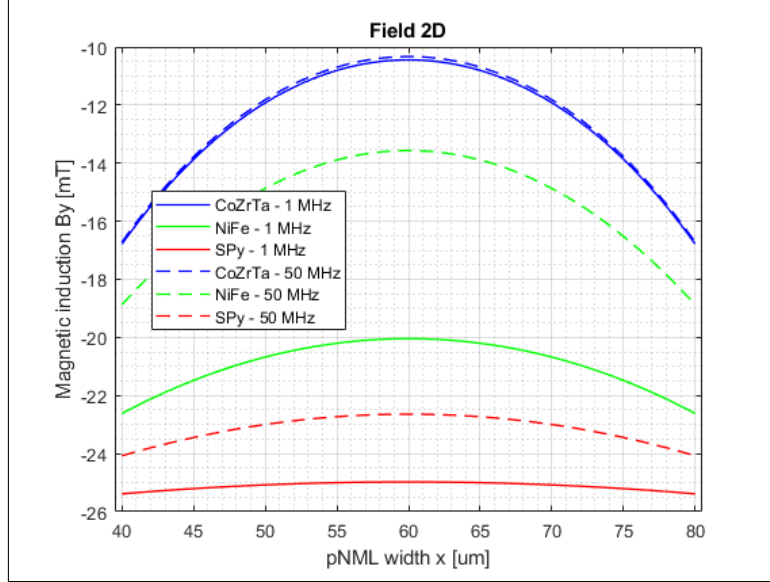


Figure 4.4: Perpendicular magnetic induction across the pNML region

In order to get a more realistic structure the next step is to build a 3D structure. To do so, a curve that joins the 2 wire faces was designed. Since the technological point of view is always to be taken into account, the curve is composed by 3 parts with the same width and length: 2 parts inclined at 45° and 1 horizontal part, because this is the best way to realize it. Furthermore, avoiding too sharp curves is important because it prevents the current (and in turn the field) from thickening in those points and enforces its uniformity in the whole domain. Around and above the curve dielectric and cladding are placed in a simple way to create a rectangular cover in the zone of the curve for the moment and in the other parts they merely follow the pattern and the shape of the 2D structure.

The new structure is shown from the top in fig.4.5 where the upper part of air domain is hidden and the structure is made transparent to see the internal domains and in particular the curve, and in fig.4.6 where the 3D view is preferred to have a complete sight of the model of the structure.

In fig.4.7 the 3D field, computed at $1MHz$ frequency and for CoZrTa, is depicted. The field is plotted only in the domain of the pNML so it is the only one visible while the others are blank. The current starts flowing from the left side of the wire, exits from the right one and turns back in a closed loop, therefore, following the right hand rule, the field is expected to be negative in the zone within the curve and positive outside and this is exactly what happens as can be seen from the color toolbar. Also, this means that the pNML within the curve is characterized by a

negative field and the other 2 by a positive one. The red arrows plotted represent the z component of the field that is perpendicular as expected and desired in a pNML.

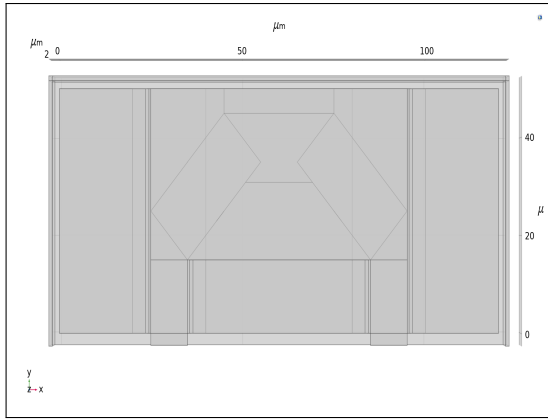


Figure 4.5: Top view of 3D structure

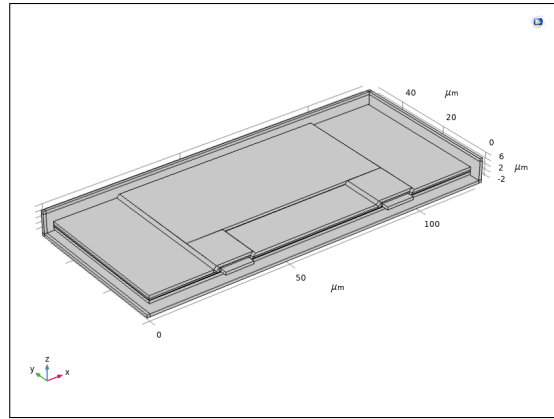


Figure 4.6: 3D view of the structure

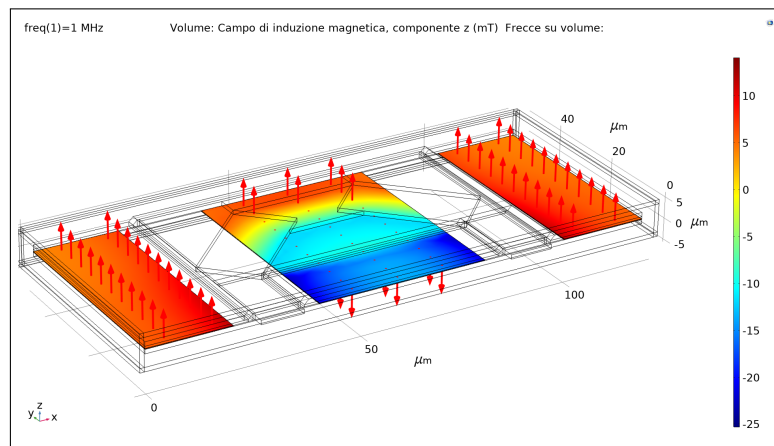


Figure 4.7: 3D view of the field

Now that the model in COMSOL is correct and working the analysis can go into detail. First of all this structure is just $50\mu m$ long but the idea is of pNML $1mm$ long so this length was increased to $120\mu m$ and $200\mu m$ for now in order not to burden the simulation too much, while the frequency is always kept fixed at $1MHz$ for these simulations.

The top views of the simulated structures for these lengths are reported in fig.4.8 and 4.9 where the considerations about the field distribution are confirmed. The following graphs represent the fields along the x and y axes through the red lines in fig.4.10 and 4.11, i.e. along x at $y = l/2$ and along y at $x = w/2$ so at the center of

structure and in particular the central pNML, because this is the pNML examined but it would be the same for the other 2 pNML obviously with the corrected coordinates. As regards the coordinate of the z axis, it is in the center of pNML too, $t_{cl}+t_{di}+t_{pnml}/2$ where there is no interlayer dielectric and $-t_{pl}-t_{cu}-t_{il}/2$ where it is present. The use of parameterized coordinates assures that even when some parameter is changed the reference coordinates are always the same and therefore the field is seen always at the same position, so these coordinates are used for all the simulations from now on.

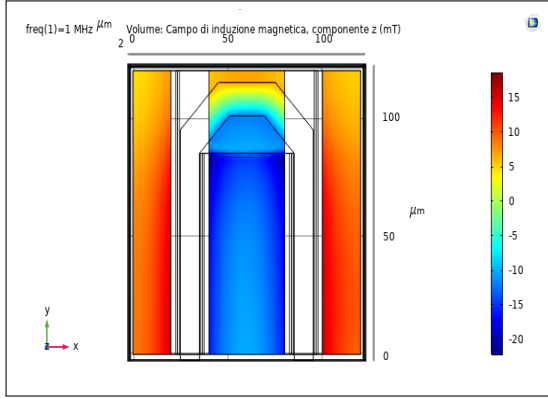


Figure 4.8: 3D field at $l = 120\mu m$

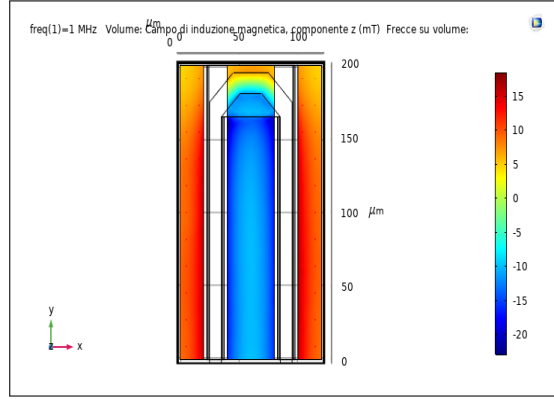


Figure 4.9: 3D field at $l = 200\mu m$

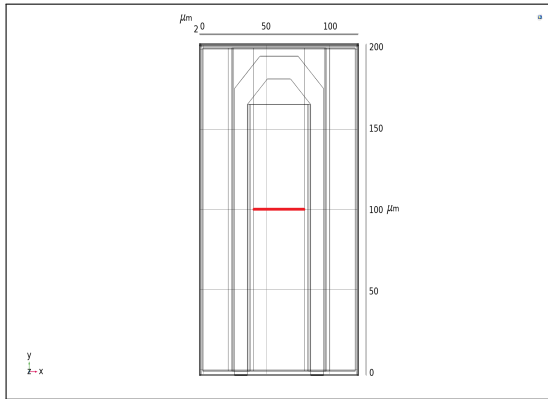


Figure 4.10: Cutline along x axis

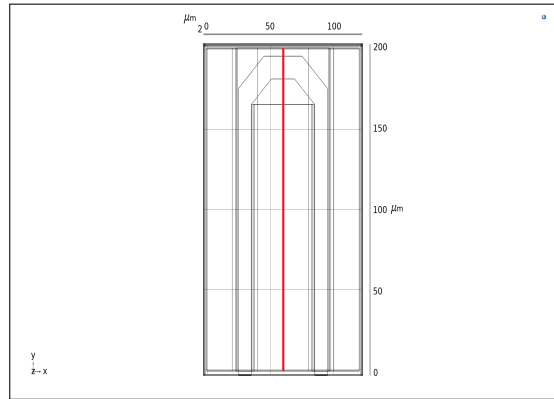


Figure 4.11: Cutline along y axis

All the lengths are compared in fig.4.12 and several things can be noted. First of all, the values on y axes are negative because the field in the central pNML is negative while the values on x axis in the second plot are negative simply for a visual effect because in this way the curve, since it is located at the end of the y axis, with a negative axis is the first thing met.

Along x the field decreases in the middle of the pNML because this is the most

distant point from the 2 parallel sections of the wire and so the field is weaker while its maximum is near the wire. Furthermore, as length increases there's a shift of the values towards smaller values because the red line moves away from the curve and goes where the field stabilizes at smaller amplitude value as can be seen in the plot along y. In this plot it is possible to see that the lengths 50 μm and 120 μm are not sufficient to appreciate the behaviour of the structure therefore the length 200 μm is chosen between these as length standard for the next simulations unless otherwise stated. Longer structures are not considered because of the computational cost and because the field is already stable at this point.

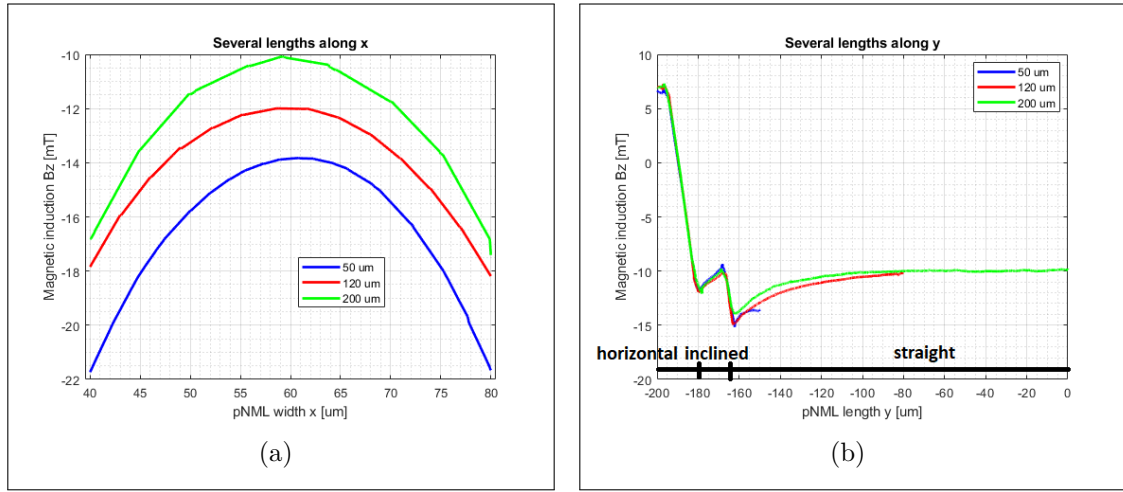


Figure 4.12: Comparison between different lengths: a) along x and b) along y

Another important thing to be analysed is the sudden decrease of the field just after the curve around 170 μm . In the figure the different wire sections met by the field along y are highlighted: after the first 5 μm there is the horizontal section of the curve that ends at 180 μm , then the inclined section of the curve follows which ends at 165 μm and the final part is the straight section of the wire that continues to the end. So the issue is limited where there is the inclined section of the curve. This is something that is not desired so a first little modification is done to the geometry in order to correct this issue.

In fig.4.13 the difference of the cladding and dielectric before and after the modification is shown. While before they just surround the curve of the wire, now they are always around the curve but, as regards in particular the sides, they are shaped around it, similarly to the straight sections of the wire, so that a uniform pattern is created all along the wire and there are no abrupt cuts in the domains.

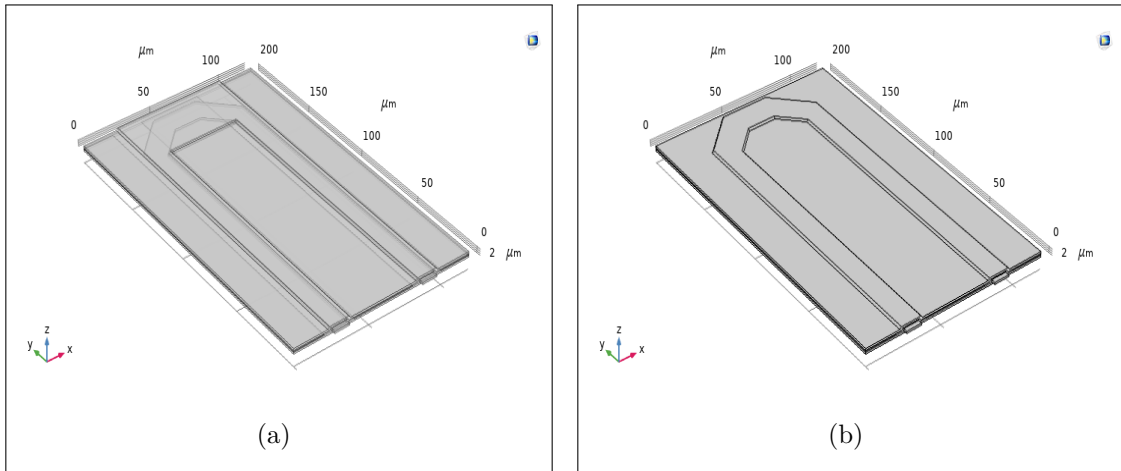


Figure 4.13: Comparison between structures: a) before shape modification and b) after shape modification

The fig.4.14, 4.15 and 4.16 depict the comparison of structures in terms of field. Along x nothing changes but along y the field flows continuously without breaks and in addition it reaches higher values across the curve. This is probably due to the fact that, since the dielectric and cladding are now closer to the wire, they are better able to confine the field.

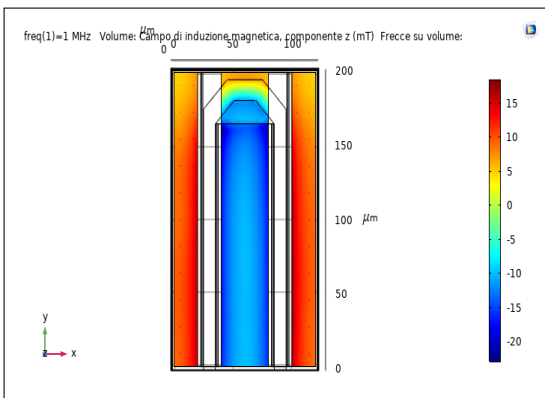


Figure 4.14: 3D field distribution without the shape modification

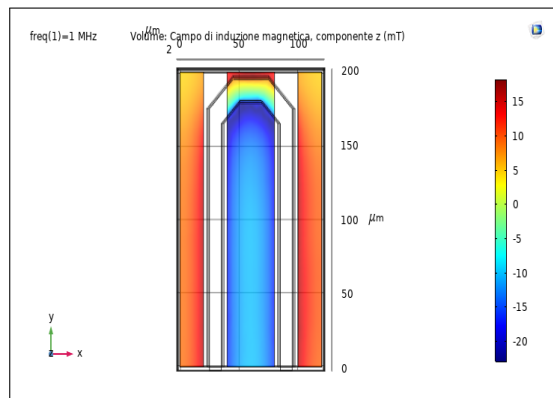


Figure 4.15: 3D field distribution with the shape modification

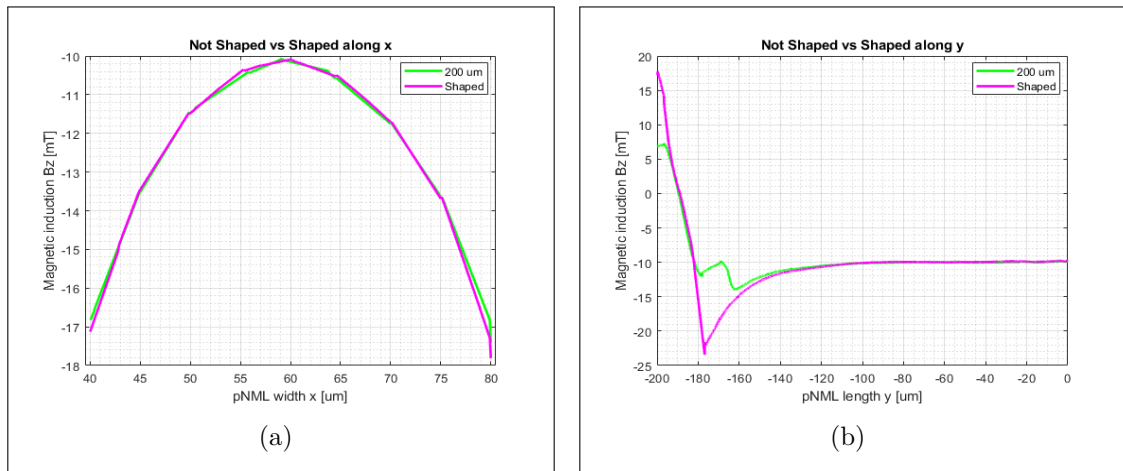


Figure 4.16: Comparison between 1D fields: a) before shape modification and b) after shape modification

Up to now the structure is considered "infinite" along y axis in the sense that in the wire is included just one curve. In a real device this wire has to magnetize many others pNML in a row so the straight sections can no longer be so straight and a second modification is needed. The idea is to virtually extend the wire by creating other curves which affect the lateral pNML like the one already simulated. Fig.4.17 and 4.18 show the comparison with a more real structure. The structure is now composed by 3 curves but is cut at half of the new curves because, for symmetry, this block could be a cell to be repeated n times based on how many pNML are wanted.

Observing the plots it can be noted that, since the 2 ends of the wire moves away from each other, the field in the zone of pNML in the middle of them decreases. The comparison is depicted in 1D in fig.4.19 to get a better understanding. The field begins to decrease and halves at the end and the same holds for the other 2 extremities of lateral pNML.

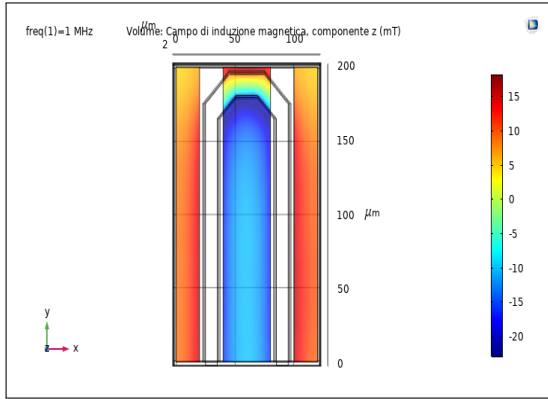


Figure 4.17: Structure with straight wire

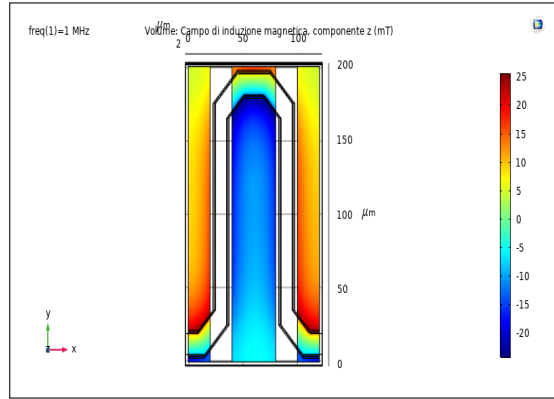
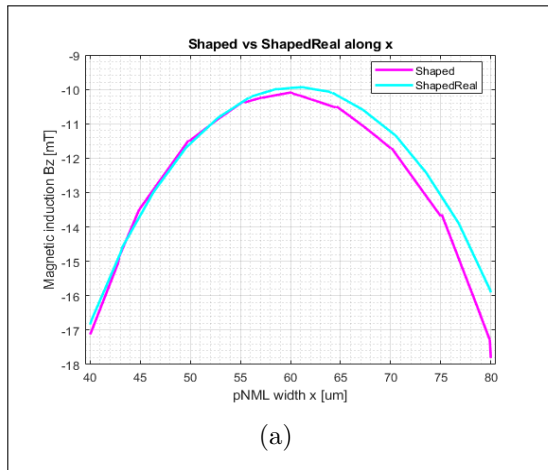
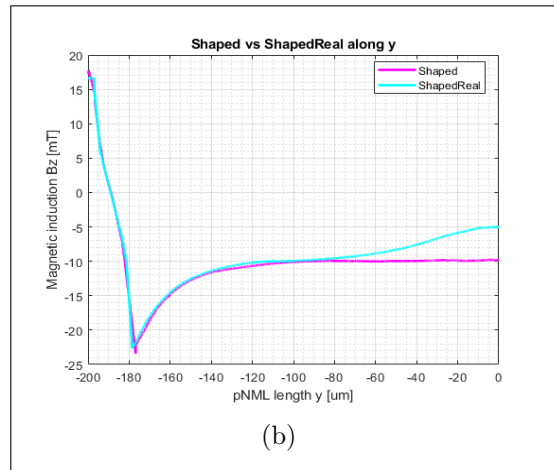


Figure 4.18: Structure with real wire



(a)



(b)

Figure 4.19: Comparison between structures: a) before wire modification and b) after wire modification

4.2 Material choice

In chapter 3 the argument of geometry was already discussed. Summing up, in order to reduce the load of simulation the symmetry of the structure was exploited. The structure can be halved along the y axis and so the result is the base cell of fig.3.7 which, from now, is used for the simulations and it is reported here for clarity from top view, fig.4.20. Basically the field along y is always the field at the center of pNML because the boundary conditions are always applied on the sides of the structure, so even if the pNML is halved now, the BC assure the correct flow of current and nothing changes. As regards the field along x it is the same, the only difference is that it is possible to see only half of the field so on the right at the end of the graph the field is at the central point of the pNML (where it decreases).

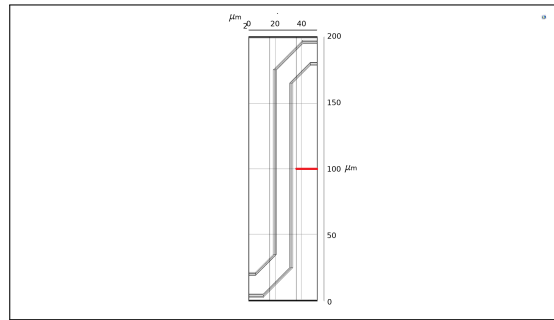
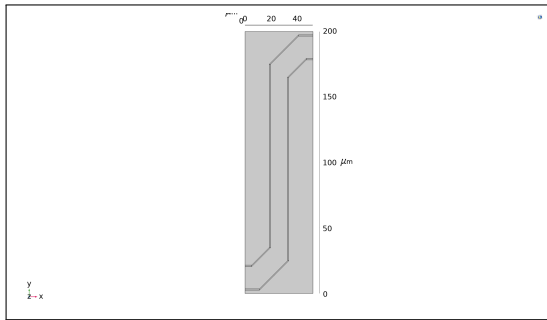


Figure 4.20: Top view of reference cell

Figure 4.21: Half cutline along x axis

Since it is not advantageous to carry out the simulations for 3 different materials a selection was made. Field amplitudes of 50mT [9, 51, 52] are necessary for clocking the pNML devices so a simulation that compares the materials with this field was done. This means increasing the current from the initial value i_0 of the 2D structure of a factor that depends on the material. The result is shown in fig.4.22 for x axis (through the red line in fig.4.21 which obviously is the same line in fig.4.10 so at $y = l/2$ but cut at half) and in table 4.1 the computed values of current are reported.

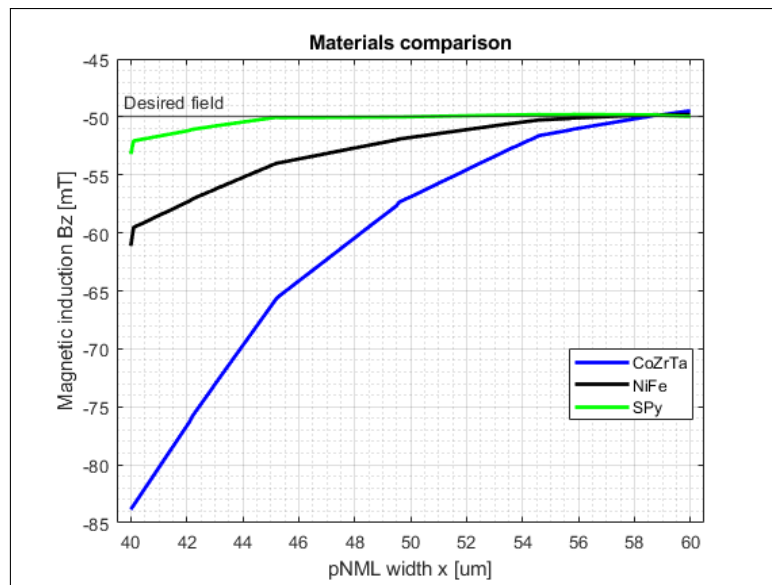


Figure 4.22: Comparison between soft magnetic materials with same current

Material	Current[A]
CoZrTa	$5 * i_0 = 0.14$
NiFe	$2.63 * i_0 = 0.07$
SPy	$2.03 * i_0 = 0.06$

Table 4.1: Current values for 50 mT for all the materials

The best material, i.e. the material which gives the value of $50mT$ with the lowest current, is the SPy as expected because it has the highest μ_r and therefore it will be the material standard.

4.3 Parametric analysis

The field of $50mT$ has to be very stable to guarantee the correct behaviour of the circuit and avoid parts of it that see different values of field. This is the reason why the simulations will be done respecting the 1% tolerance, that is $\pm 0.5mT$, in all the directions. To assure this feature, the first parametric analysis is for the w_s , so the width of pNML. The fig.4.23 shows the comparison from the starting value of $50\mu m$ up to the smallest of $44\mu m$, these values refer always to the complete structure even though the values used in simulation are the half. Moreover, the reason why the decrease is by $2\mu m$ at time is that, since the idea is to remove in every simulation $1\mu m$, the fact that the structure is halved must be taken into account because the decrease has to be divided in 2 and so the real decrease for the halved structure is $1\mu m$ as desired. The only value that complies with the constraints is $48\mu m$.

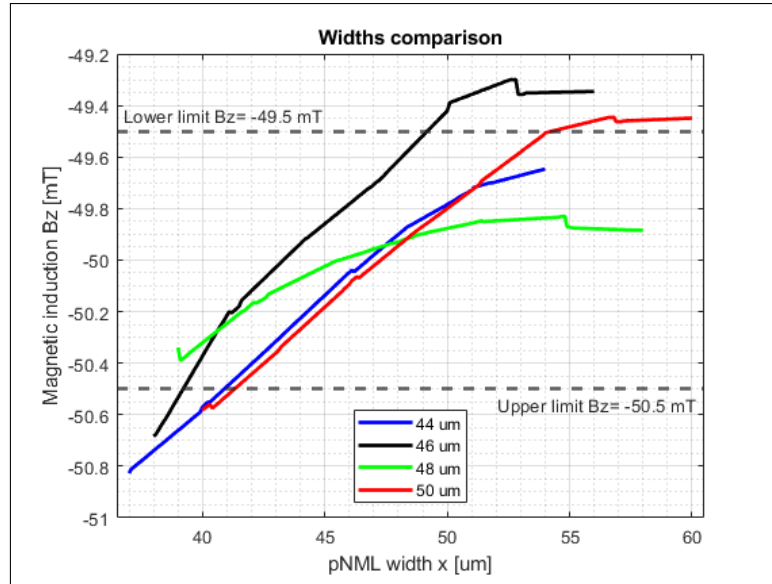


Figure 4.23: Comparison between different spacing widths

4.4 Cell field

From this first and simple analysis the results are: the use of the half structure for the simulations, the material that gives the lowest current and the width and the length of the pNML. These results give the field depicted in fig.4.24, which in the next chapter will be the reference field to be compared with.

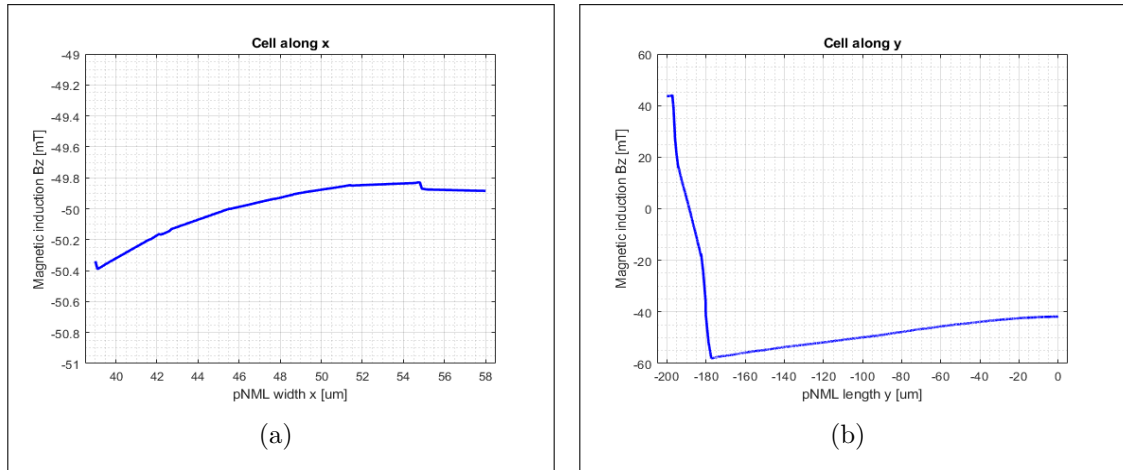


Figure 4.24: Field of the cell structure: a) along x and b) along y

Chapter 5

Structure design

In this chapter the structure is modified with the aim of enhance the amplitude and stability of magnetic field but keeping the current and in turn the power consumption as low as possible. This can be done following 2 similar but different approaches: exploiting the same current to get an higher field or getting the same field with lower current. In this thesis the first one is followed therefore any modification to the geometry focuses on this problem. Different structures are realized and discussed up to get the best one in terms of performance.

5.1 Array structures

In order to improve the field, the strategy used was to enclose the pNML domain in a structure crossed by more wires within the cladding. At first glance this modus operandi can seem counterproductive but the idea is to increase both the amplitude and the stability of the field to the point of compensating for the increase in dissipated power.

The confinement can be seen in all directions. Along x the whole curve itself confines the field along this direction so it is not necessary and even possible adding a new wire. On the contrary, as seen in fig.4.19 along y direction the field decays so it needs an improvement. Finally, up to now the z direction is not considered but the design of a structure must take advantage of all the possibilities.

In this thesis these structures are named array structures because from a global point of view the simulations are done for a base cell but, due to the strong symmetry of the structure, they could be repeated several times doubling the base cell in a similar way to what happens in a memory with a matricial organization where the pNML can represent the cells of memory and the wires can represent bitlines and wordlines.

5.2 Horizontal array

This section is called horizontal array because only the confinement along y is discussed. This means the wires are placed horizontally on the same plane.

5.2.1 Two wires array

The first wire added (that will be called bottom wire from now on) is placed at the bottom of the structure with one wire (original wire from now on), fig.5.1.

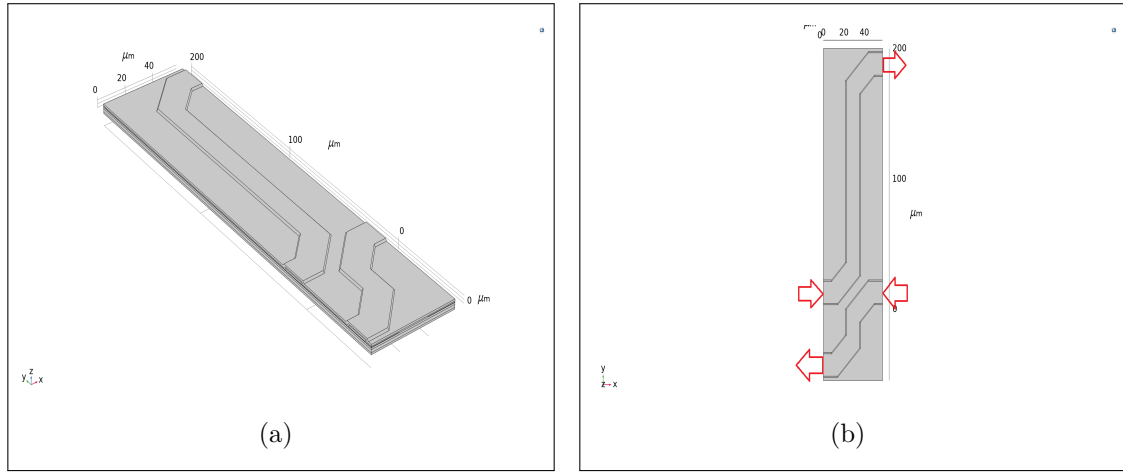


Figure 5.1: Horizontal array with bottom wire: a) 3D view and b) Top view

The only difference between these wires is the length that for the original wire is always $200\mu m$ and for the bottom wire is just $80\mu m$ to reduce the time of the simulation but every aspect is equal. The focus in the complete structure was on the central pNML and now in the array structure this is not changed, therefore the fields are plotted using the same red line in fig.4.11 at the center of pNML and the task of this bottom wire is to affect mainly this pNML, that is the right pNML in this new structure.

The position is not casual: the bottom wire along y is located at a point where the horizontal sections of the semicurves coincide. This is done because, considering the complete structure, the positioning of the bottom wire allows to create, at the final part of pNML where the field decreases, a second virtual curve and so to close ideally the pNML in a pseudo-wire that surrounds the pNML on the plane.

A consideration about the current must be done. The field in this pNML is negative (because of the direction of current in the original wire) and since the aim is to increase the field seen here the current in the bottom wire has to be opposite along x to the other current so it goes from right boundary to the left one; in this way both wires produce a negative field for this pNML and the effect is increased. From

the software standpoint this means that if the current enters from the left boundary of the original wire after it exits on the right, the same current enters in the bottom wire from the boundary on the right, flows into the wire, exits from the left and enters again in the original wire because the main thing to keep in mind is always the importance of creating a closed circuit. Arrows that indicate the direction of the current are added.

The field along y of the horizontal array with the bottom wire is reported in fig.5.2.

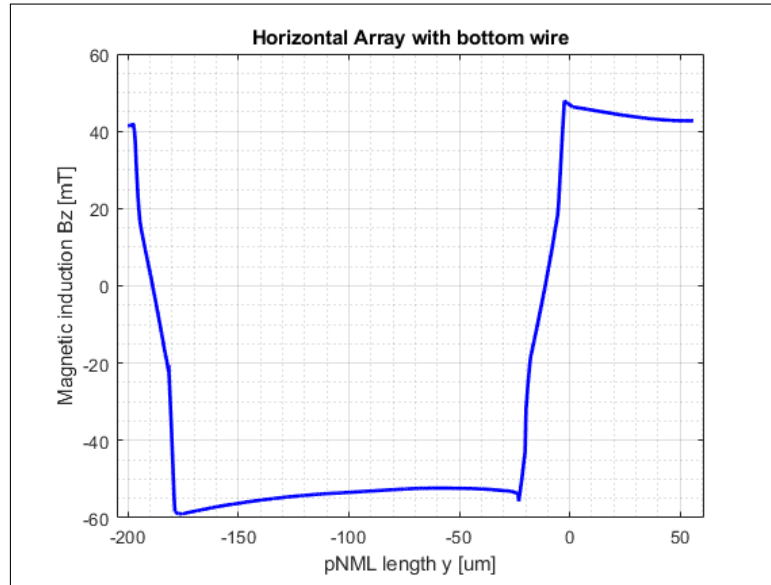


Figure 5.2: Field along y axis of horizontal array with bottom wire

The 2 vertical sections of the graph line represent the crossing of the curves when the field changes sign, in the middle it is negative because this is the pNML zone and then after the curve of the bottom wire it decreases to reach a more stable value; positive value because that zone of the pNML is characterized by a positive field given by the current direction. It can be noted that, with respect to the structure with one wire in fig.4.24, the field in pNML is now very more stable and there is a little increase of amplitude too.

All the considerations made so far can be repeated on the other side of the original wire, in the sense that, if the attention moves on the other pNML, the left pNML where the field is positive, the bottom wire is no longer suitable to affect this pNML and a top wire is needed, fig.5.3.

This top wire geometrically is identical to the bottom wire, with the same reasons in terms of length and in terms of position. As regards the current, as in the case of the bottom wire, the top wire has to have a current that flows in the opposite direction with respect to that of the original wire, so that the field that this current generates is positive in the left pNML and concatenates with the field of the original

wire.

For simplicity, the goal continues to be the improvement in the right pNML because each step can be mirrored for the left one. So, the field in the right pNML is plotted in fig.5.4.

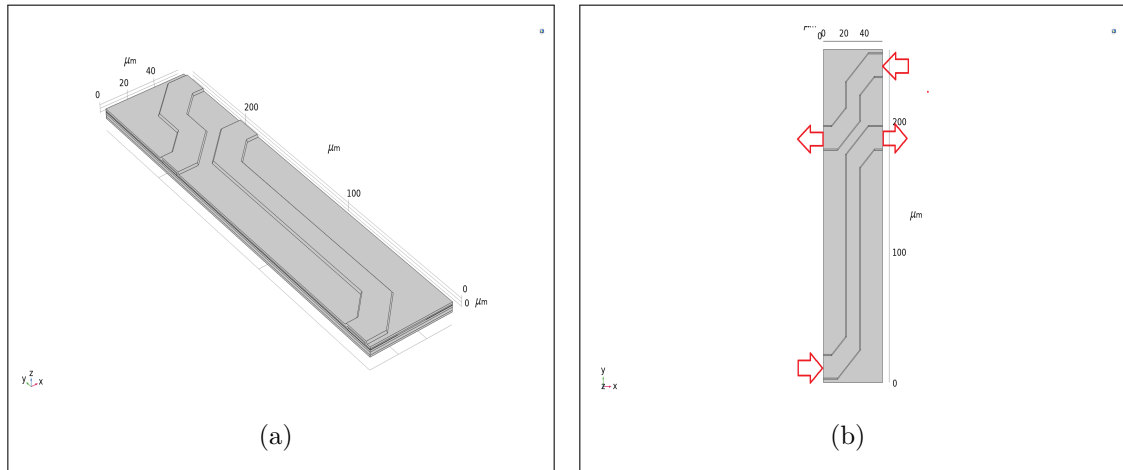


Figure 5.3: Horizontal array with top wire: a) 3D view and b) Top view

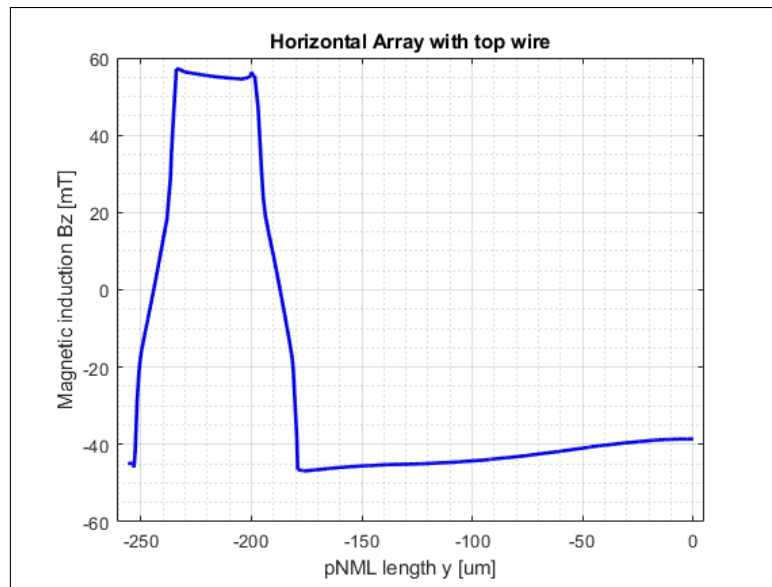


Figure 5.4: Field along y axis of horizontal array with top wire

This time the field is increased between the 2 curves that is before the curve of the original wire because of the interaction with the near top wire. This allows to understand that both the 2 wires structures are needed. This leads to a 3 wires structure.

5.2.2 Three wires array

The complete structure is depicted in fig.5.5 and the field in fig.5.6. Basically, along y it is the union of the previous fields but with the benefits of both, the pNML sees an higher field and for a bigger area. Along x instead, there is a worse behaviour with a loss of tolerance that leads to a smaller available area but it is compensated by the improvement along the other axis. As regards the coordinates of the field, they are always the same at the center of the central pNML, since the reference field is always the cell field and the aim is to improve the field in this pNML.

It is interesting to note that, since the currents flow in opposite direction in the wires that compose the structure, the pNML sees progressively zones of positive and negative stabilized field not only along the x axis where the single wire cross several pNML but also along y where several wires cross the same pNML in different positions. In addition, the constraint about the closed loop for the current is always valid so the current must exit and then enter again in the boundaries of the wires like the wire was just one, this is important to keep in mind when the BC are posed.

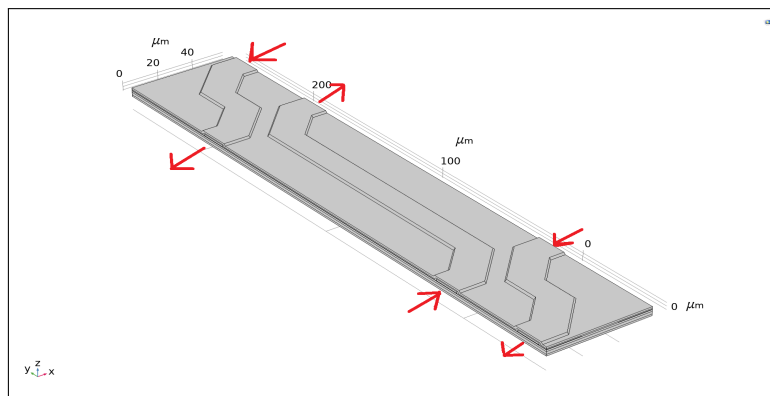


Figure 5.5: Complete horizontal array with $80\mu m$ additional wires

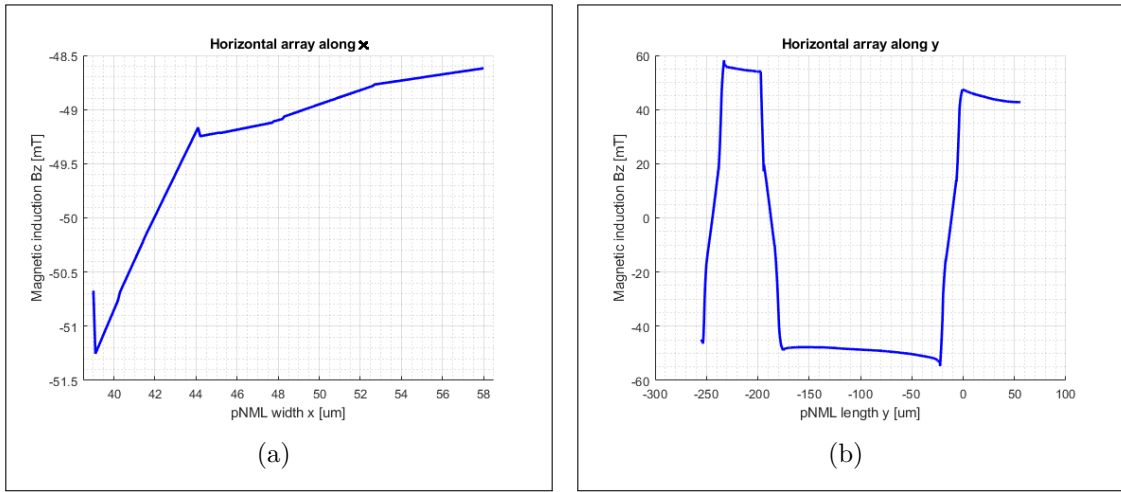


Figure 5.6: Field of complete horizontal array with $80\mu\text{m}$ additional wires: a) along x and b) along y

The doubt is that the length of the additional wires can play a role in this field (in particular the proximity of the top wire) and this cannot be neglected. For this reason the structure was modified, at a cost of computational load, with additional wires as long as the original to have a uniform structure that represents better a possible real circuit where all wires have to be equal and in turn to have a better idea of the behaviour of the structure, therefore the structure in fig.5.5 is abandoned in favor of this modification. It is depicted in fig.5.7 and called "ThreeWires". All the constraints are not changed, it is just a change in size of the additional wires. The field is reported in fig.5.8.

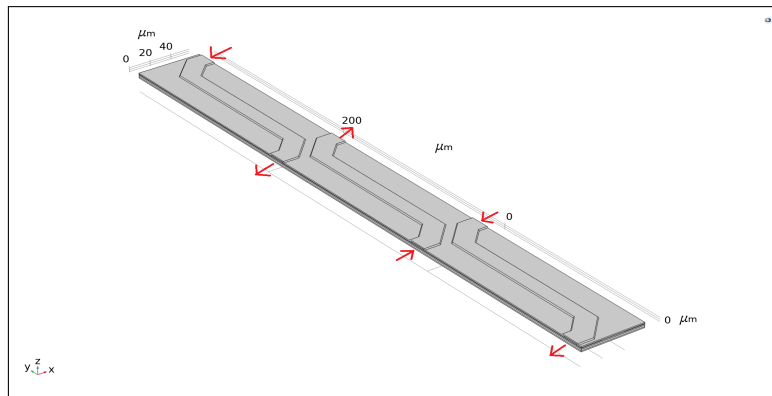


Figure 5.7: Complete horizontal array with $200\mu\text{m}$ additional wires

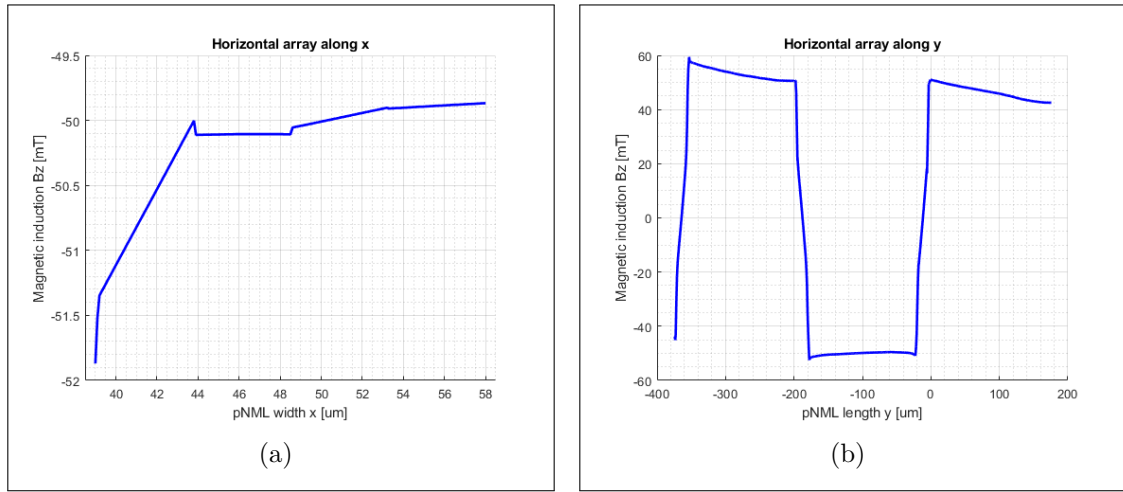


Figure 5.8: Field of complete horizontal array with 200 μm additional wires: a) along x and b) along y

It can be noted that the field is better along both axes. Along x the tolerance is almost always respected while along y the stability is the main benefit because the field has the same amplitude as in the case of one wire structure but for a wider area.

The comparison between these 2 structure in terms of field is reported in fig.5.9. In table 5.1 are reported the values for: the medium field, calculated from MATLAB along x; the available area, calculated as a rectangle where base and height are the zones where the tolerance is accomplished and is multiplied by 2 because the interest is in the whole structure; the dissipated power density, given by the ratio of peak power (extracted from COMSOL and multiplied by 2 to take into account the other half structure and multiplied for the number of the wires) over area. The goal is the continuous improvement of these parameters.

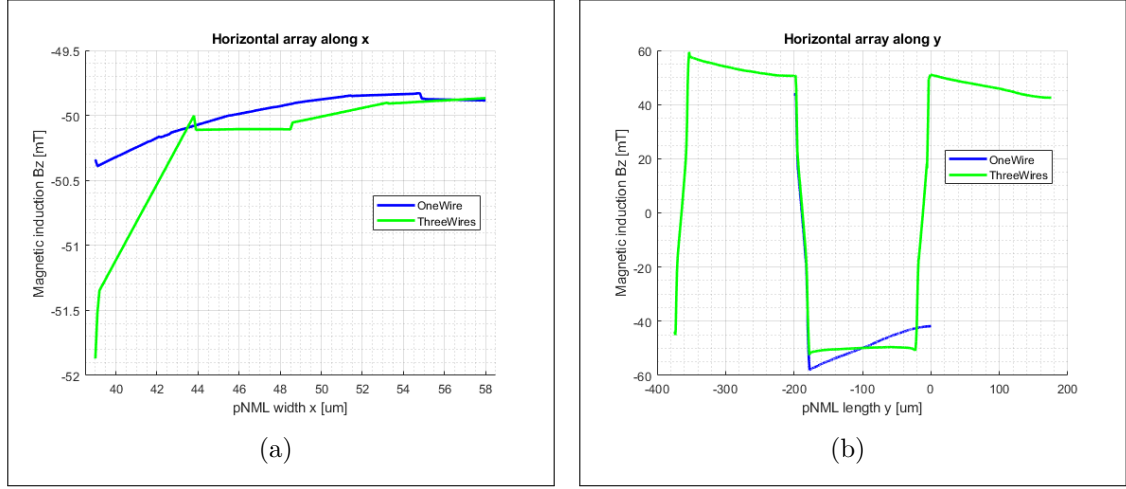


Figure 5.9: Comparison between structure with one wire and 3 wires: a) along x and b) along y

Structure	Medium field[mT]	Available area[μm^2]	Power density[$\mu W/\mu m^2$]
OneWire	-50.11	399	5.17
ThreeWires	-50.87	3962.28	1.56

Table 5.1: Comparison of values between OneWire and ThreeWires

The improvement is evident, the field is slightly higher but above all the area is tenfold greater and the power is dropped by more than 3 times. This means that the number of pNML can be tenfold increased in the same zone and at the same time it consumes less than one third of power.

The aim of increasing the field led to another modification for the structure. The position of the additional wires is calculated with precision for the reason already explained, summarizing, to create an ideal curve that encloses the pNML on the plane. The idea is to put the additional wires closer with the aim of improving the effect on the pNML. The structure thus modified called "SuperDense" with a shift of $10\mu m$ towards the original wire by both the additional wires is depicted in fig.5.11 compared to fig.5.7 and the field and the table of values follow in fig.5.12 and table 5.2. Nothing is changed about other parameters.

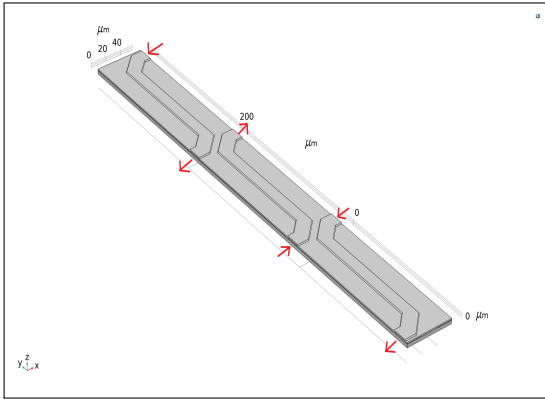


Figure 5.10: Structure with additional wires at the original position

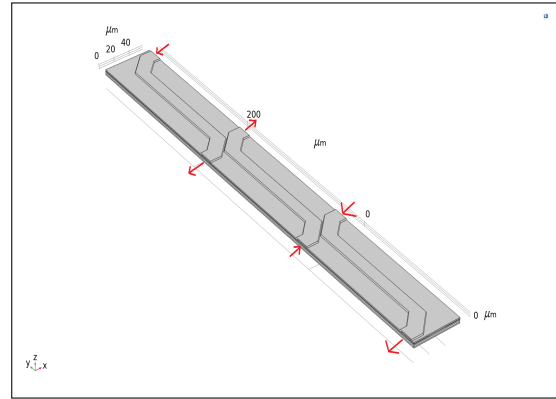


Figure 5.11: Structure with additional wires at the new position

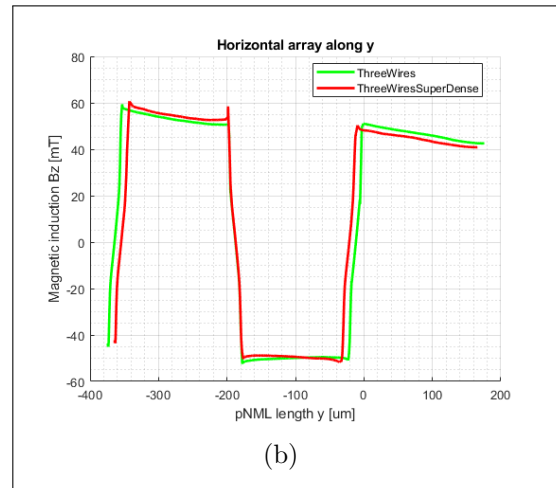
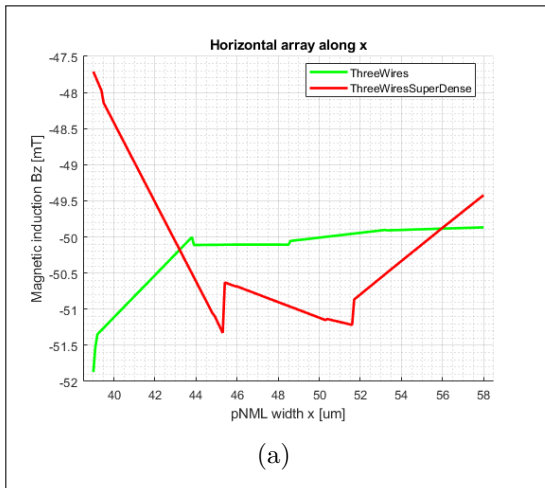


Figure 5.12: Comparison between fields with different position of additional wires: a) along x and b) along y

Structure	Medium field[mT]	Available area[μm^2]	Power density[uW/ μm^2]
ThreeWires	-50.87	3962.28	1.56
SuperDense	-49.52	208.26	29.67

Table 5.2: Comparison of values between ThreeWires and SuperDense

Every parameter is worsen so this structure no longer used and the original position of additional wires is the best one.

5.2.3 Five wires array

Since the additional wires show a less stable field in their zone of pNML it is possible to add 2 other additional wires in order to improve their stability and maybe the amplitude of the field in the central zone where the attention is always focused. The longer structure called "FiveWires" is depicted in fig.5.13 with again the original position of additional wires which is kept for the new ones and the comparison with the ThreeWires is in fig.5.14 and table 5.3, about always the central pNML of the original wire at $y = l/2$.

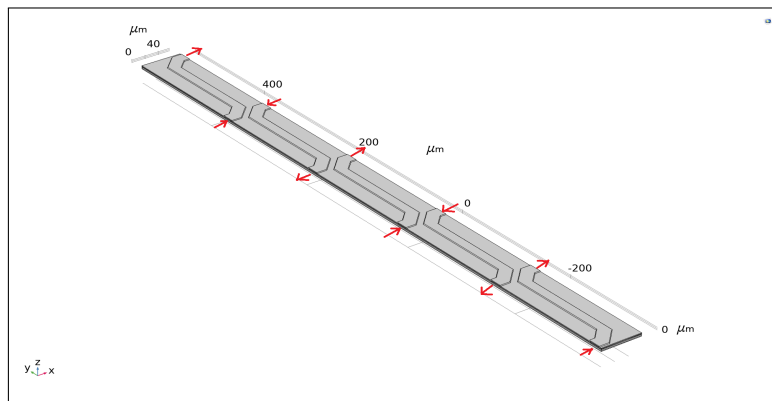


Figure 5.13: Complete horizontal array with 5 wires

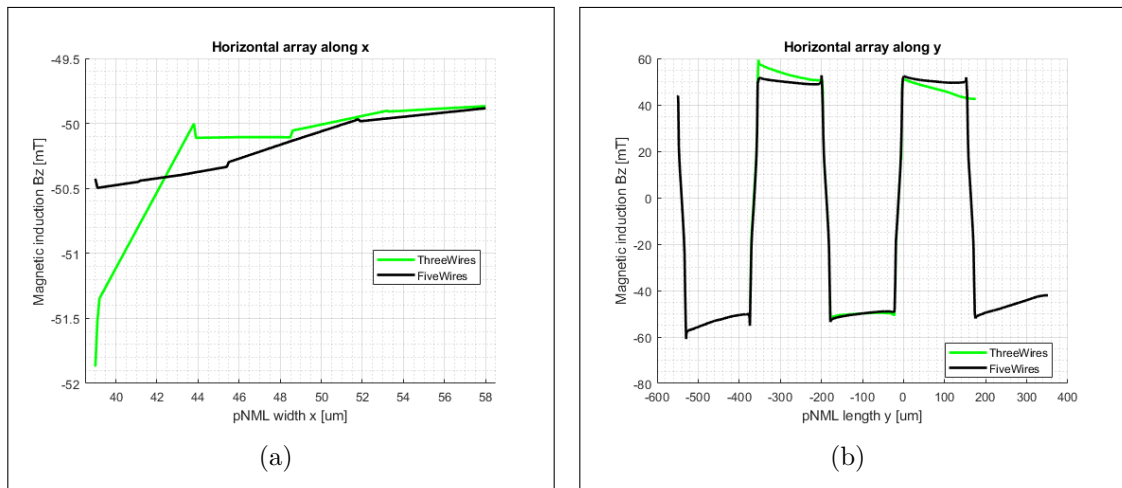


Figure 5.14: Comparison between fields with different number of additional wires: a) along x and b) along y

Structure	Medium field[mT]	Available area[μm^2]	Power density[uW/ μm^2]
ThreeWires	-50.87	3962.28	1.56
FiveWires	-50.19	1020.3	10.10

Table 5.3: Comparison of values between ThreeWires and FiveWires

The intuition was correct and the structure presents a better stability but there is a worsening of the values precisely where the goal is to maximize them and so the benefits of this structure are not useful.

Definitely, the best structure with this array structure is the ThreeWires. Even if there is no a big improvement in terms of field amplitude the big advantage is in terms of field stability, this leads to an big improvement in area and so power is dropped too.

5.3 Vertical Array

The array structure can be exploited to build a geometry that uses in a smarter way the third direction given by a pNML. So far the additional wires were always placed on the same plane so they influence the same pNML but in different zones along the length of the pNML layer but what happens when more wires affect the same zone of pNML will be investigated now.

5.3.1 Two wires array

The 3D structure called "NormalCladding" is in fig.5.15.

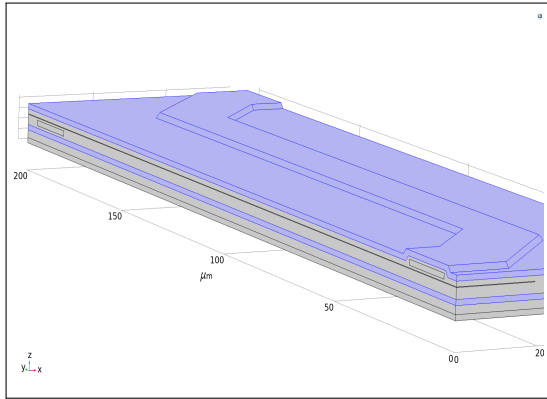


Figure 5.15: 3D view of array structure along z

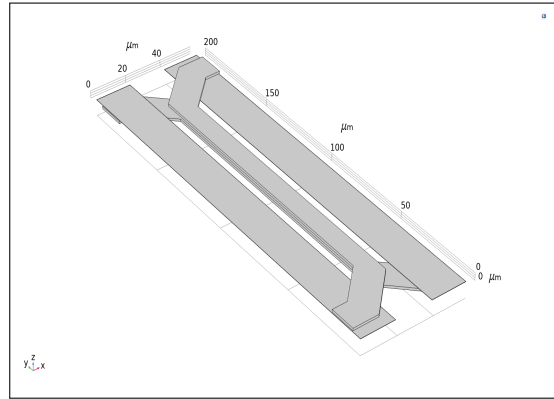


Figure 5.16: Internal view of array structure with 2 wires

The cladding is highlighted and the upper air domain is hidden. The 2 layers of wires can be seen and the pNML is in between. The fig.5.16 shows the internal

structure so just wires and pNML are visible. Going into the details, the 2 wires are the same length and are parallel in the central straight part but, while the upper one is the wire as seen in fig.3.7, the lower one present the curves at the opposite side with respect the upper wire so that, since the currents go in the opposite direction also this time, they produce concordant fields in every pNML they meet along x because this is always a cell but ideally the wires continue along x. The lower wire is surrounded by dielectric as the upper one and between the wires there is also dielectric with the block of interlayer dielectric already discussed in chapter 3. About the pNML, it is in the middle of the structure and of the interlayer dielectric because the goal is that it has to be irradiated by both wires in the same way. As regards the shape of the cladding, nothing is changed.

To understand even better the difference with the structure with one wire the profiles 2D of these structures with the highlighted cladding are compared. The fig.5.17 and 5.18 refer to the same line of fig.4.10 at $y = l/2$. The difference is in the distance of the cladding armors due to the presence of the second wire which moves away the lower armor from the center of the structure. Indeed, while before the distance between the armors was $0.7\mu m$ in this structure is $3\mu m$.

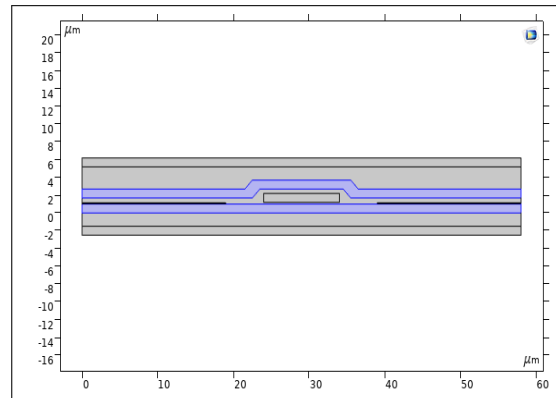
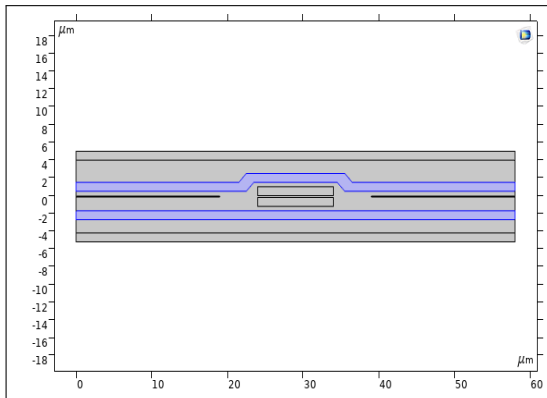


Figure 5.17: 2D view of array structure

Figure 5.18: 2D view of cell structure

The field produced by these structures is compared in fig.5.19. Interestingly, even though the field amplitude is less than half the other structure, it is completely flat both along x and along y. This means that the stability improved enormously and so that this structure deserves to be better analyzed. In addition, along y the field starts and ends at $0mT$ because the currents come from the curves, meet at the center and divide again but, since the currents are opposite where they are at the beginning or the end of the wires they generate fields of opposite sign. In this way, where the wires cross, the field is basically null and the field is perfectly contained in the internal side of the curves.

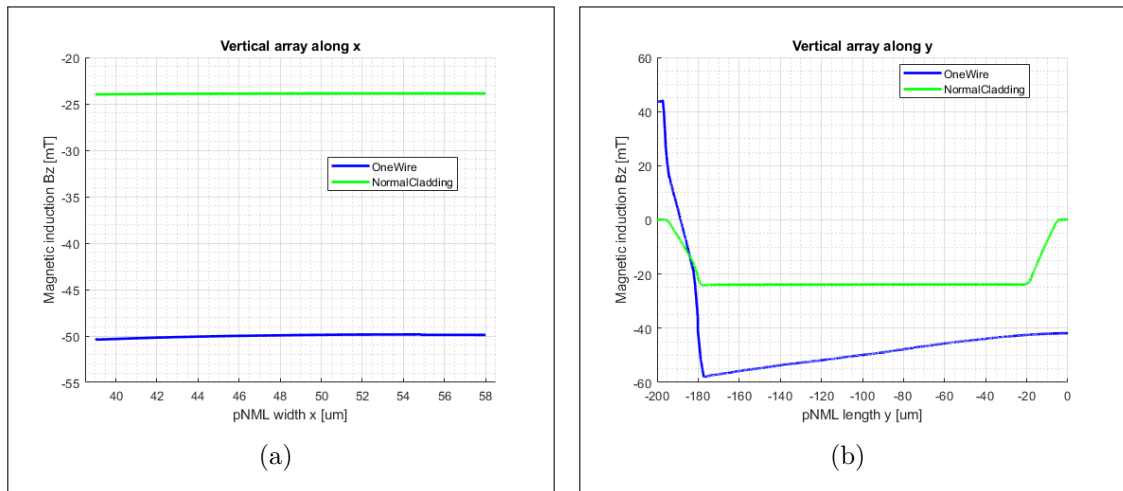


Figure 5.19: Comparison between fields with the array structure with the normal cladding: a) along x and b) along y

To verify which is the problem that causes this drop of field a structure called "FlatCladding" with flat cladding armors at the same distance from the pNML is simulated and at a distance between them of $3.2\mu m$. It is reported in fig.5.20 and again the 2D view in fig.5.21.

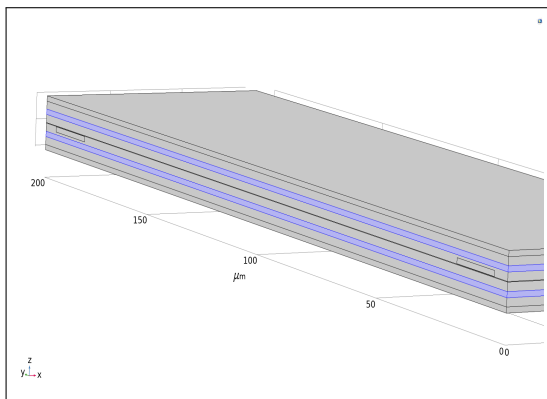


Figure 5.20: 3D view of array structure with flat cladding

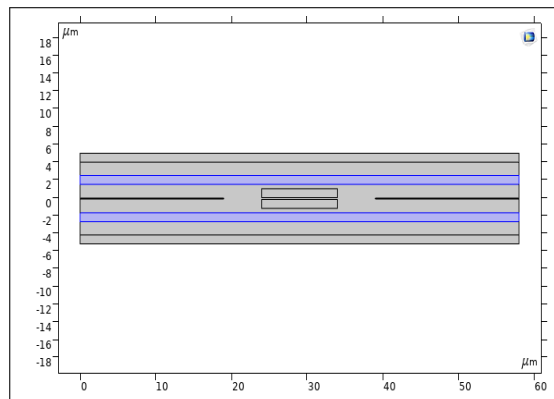


Figure 5.21: 2D view of array structure with flat cladding

The field is depicted in fig.5.22. It is even worse than the previous case due to larger distance between armors, so to have an improvement it is necessary put closer them. Since before the upper armor was made flat because it had to be equal to the lower one, the next step is to invert the modification.

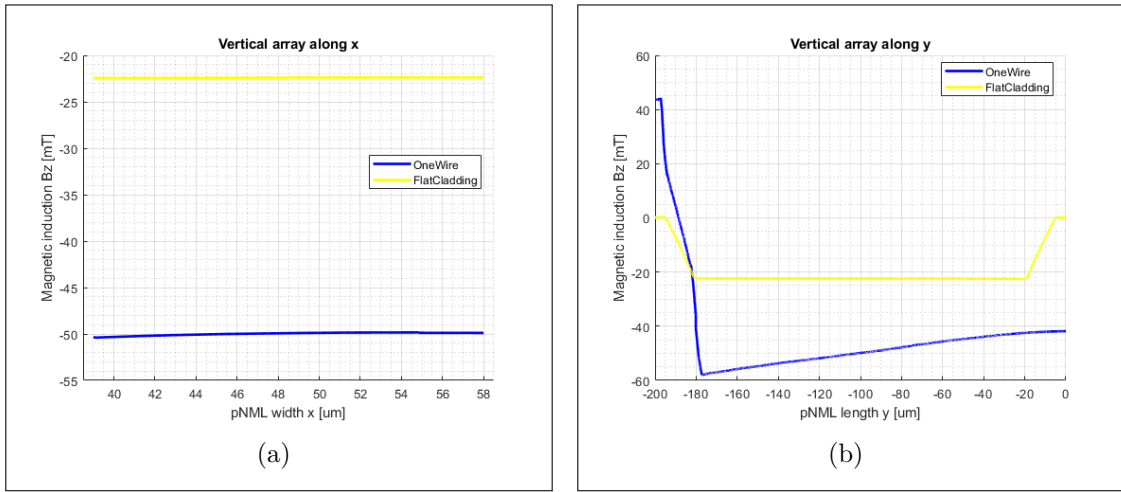


Figure 5.22: Comparison between fields with the array structure with the flat cladding: a) along x and b) along y

The new structure is called "ShapedCladding" since the lower cladding armor is shaped, like the upper one, around the lower wire both in terms of dielectric and in terms of cladding. This means that the pNML now is better enclosed by the cladding in a smaller region since the distance between the armors is $1.2\mu m$ and so the field itself is better conveyed towards the pNML. The following figures depict the structure (fig.5.27 and 5.29) and the field (fig.5.25). The table 5.4 reports the parameters of comparison with the structure OneWire.

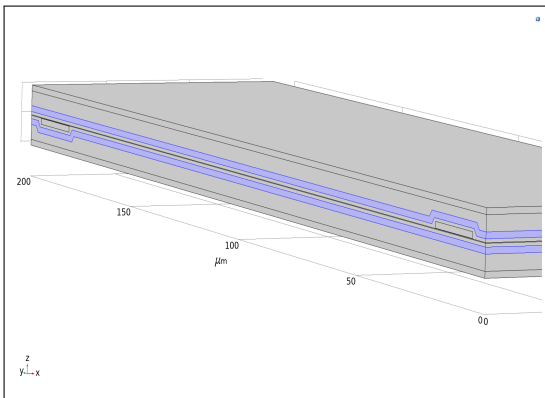


Figure 5.23: 3D view of array structure with shaped cladding

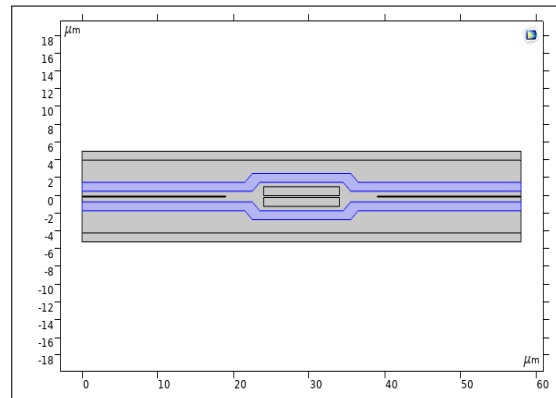


Figure 5.24: 2D view of array structure with shaped cladding

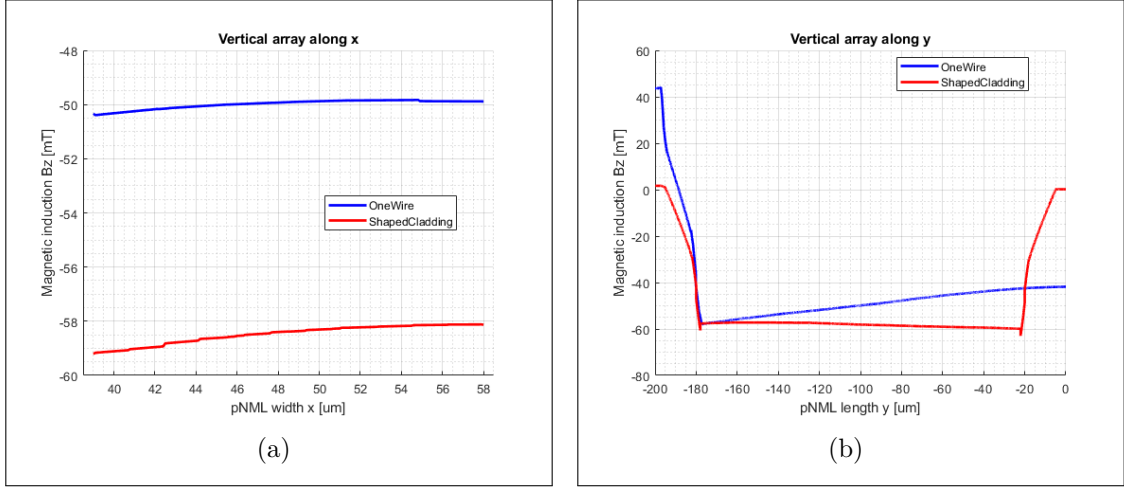


Figure 5.25: Comparison between fields with the array structure with the shaped cladding: a) along x and b) along y

Structure	Medium field[mT]	Available area[μm^2]	Power density[$\mu W/\mu m^2$]
OneWire	-50.11	399	5.17
ShapedCladding	-58.66	1960.8	2.10

Table 5.4: Comparison of values between OneWire and ShapedCladding

As expected, the field maintained the stability of the previous structures but improved the amplitude of the field of almost the 10%, the area is increased of almost 5 times and the power is almost halved.

It is possible to go even further and put closer the cladding armors even more. The structure "SuperShapedCladding" is designed reducing the dielectric thickness between the pNML and cladding from $0.55\mu m$ of the ShapedCladding to $0.05\mu m$ and the distance between the armors from $1.2\mu m$ to $0.5\mu m$, leaving all the other parameters equal to before. These 2 structures are compared in fig.5.26 and 5.27 from the 3D standpoint and in fig.5.28 and 5.29 from the 2D one so that it can be seen what means the reduction of the dielectric, now the cladding armors are almost touching the pNML. For the usual comparison with structure OneWire the field is plotted in fig.5.30 and the computed values in table 5.5.

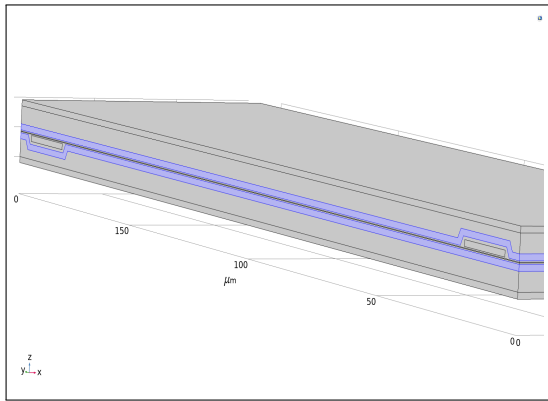


Figure 5.26: 3D view of array structure with supershaped cladding

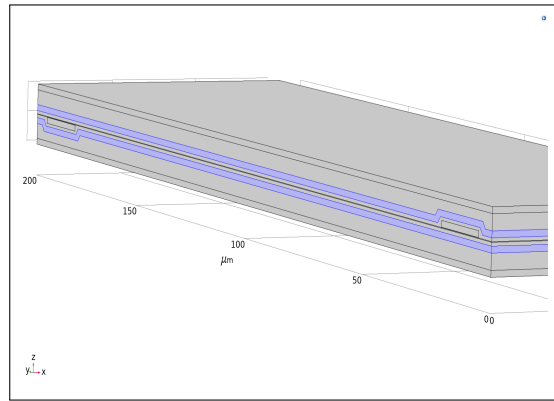


Figure 5.27: 3D view of array structure with shaped cladding

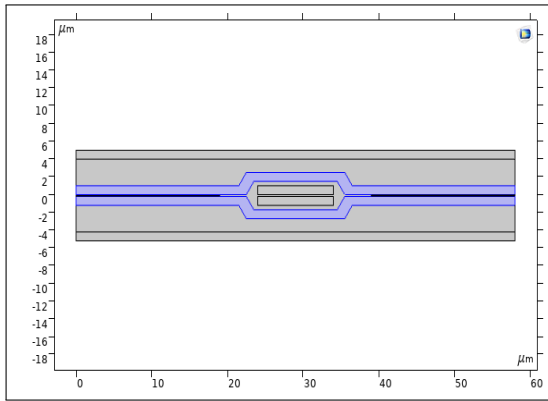


Figure 5.28: 2D view of array structure with supershaped cladding

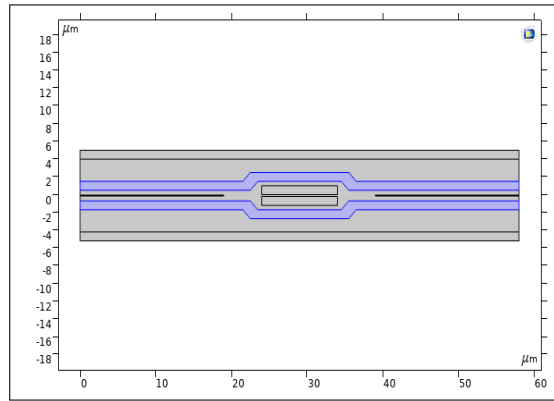
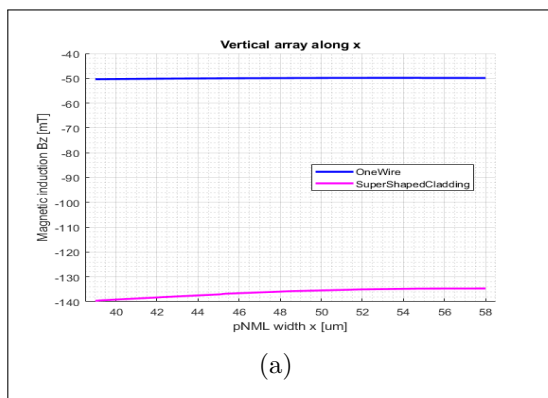
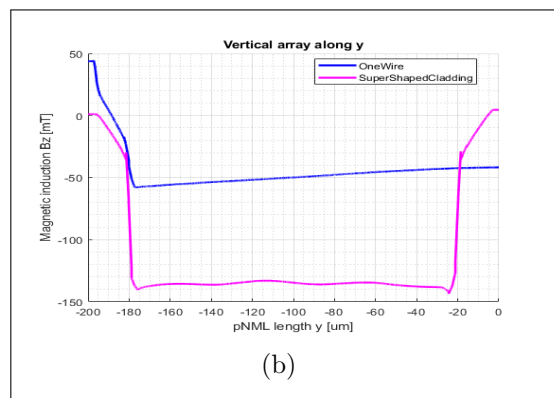


Figure 5.29: 2D view of array structure with shaped cladding



(a)



(b)

Figure 5.30: Comparison between fields with the array structure with the supershaped cladding: a) along x and b) along y

Structure	Medium field[mT]	Available area[μm^2]	Power density[uW/ μm^2]
OneWire	-50.11	399	5.17
SuperShapedCladding	-137.16	183.56	22.48

Table 5.5: Comparison of values between OneWire and SuperShapedCladding

It is true that there is an higher field but there is also an area more than halved and above all the power density is increased more than 4 times and this makes this structure unusable.

5.3.2 Four wires array

As in the horizontal array, it can be interesting and useful to investigate what happens when the number of wires still increases. Unlike that case, an odd number of wires should be avoided because it would create an asymmetry in the structure due to the fact that, since the pNML layer is located in the middle of the 2 wires, when a third wire is added it should be placed over or under the pNML but in that case the situation would turned out to be 2 wires above the pNML and 1 under the pNML or vice versa with the middle wire far from the cladding armor.

This is the reason why structures with 4 wires were simulated. In particular, since the best 2 wire structures were ShapedCladding and SuperShapedCladding an updated version of these ones is chosen.

The structure "ShapedCladding4Wires" (fig.5.31) contains within itself other 2 internal wires that are placed near the pNML. Inside the structure what happens is depicted in fig.5.32, where the wires are arranged alternately along the z axis like in fig.5.16 but this time for 4 wires, externally nothing changes because the cladding is shaped on the external wires. The 2D profile is in fig.5.33.

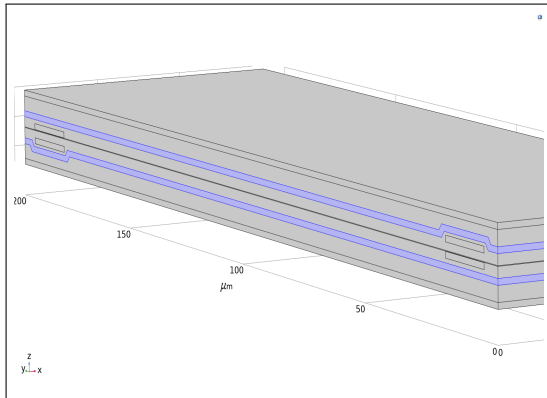


Figure 5.31: 3D view of array structure shaped cladding with 4 wires

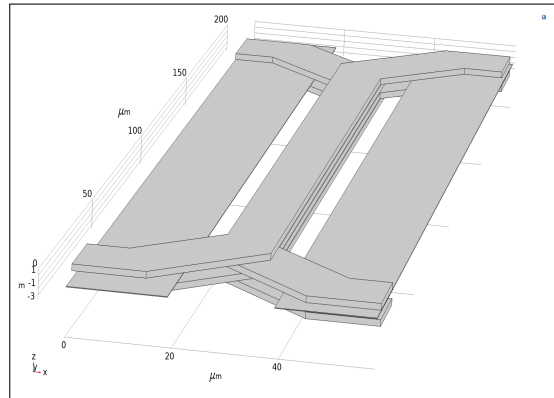


Figure 5.32: Internal view of array structure with 4 wires

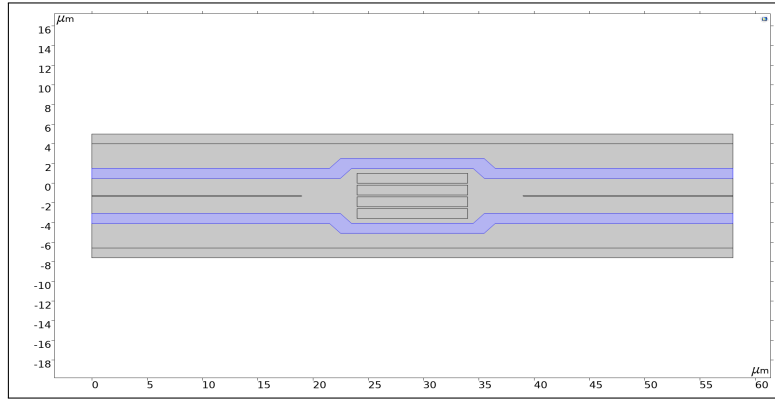


Figure 5.33: 2D view of array structure with shaped cladding with 4 wires

The field is reported in fig.5.34. It is decreased to $40mT$ so there was no improvement using 4 wires but rather a worsening because the cladding armors move away from each other at a distance of $3.6\mu m$.

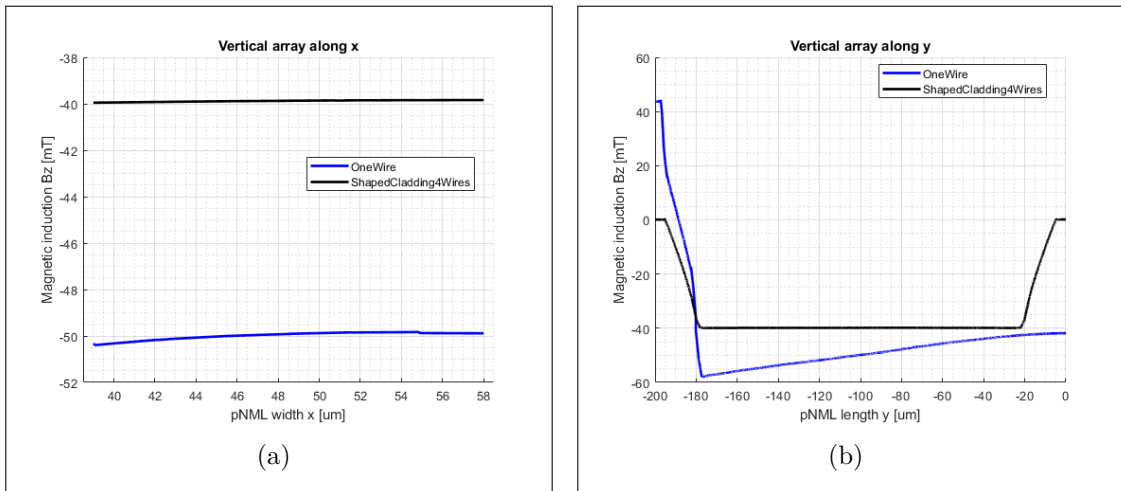


Figure 5.34: Comparison between fields with the array structure with the shaped cladding 4 wires: a) along x and b) along y

To get a better field the cladding has to be deeply modified. The cladding armors need to be closer to the pNML but also to the wires to better convey and direct the generated field towards the pNML layers. In order to do this the armors have to be shaped not only on the external wires but also on the internal ones, therefore this means that the structure becomes more complex because the cladding (and in turn the dielectric) presents a more scaled shape (the distance between the armors is again $0.5\mu m$ like in SuperShapedCladding but this time with 4 wires) that follows the internal order of the structure. This is the idea that led to the design of the structure "SuperShapedCladding4Wires" depicted in fig.5.35, where it is possible

to see the more complex shape of the cladding, and fig.5.37 compared to fig.5.33 for the 2D view for the clear difference.

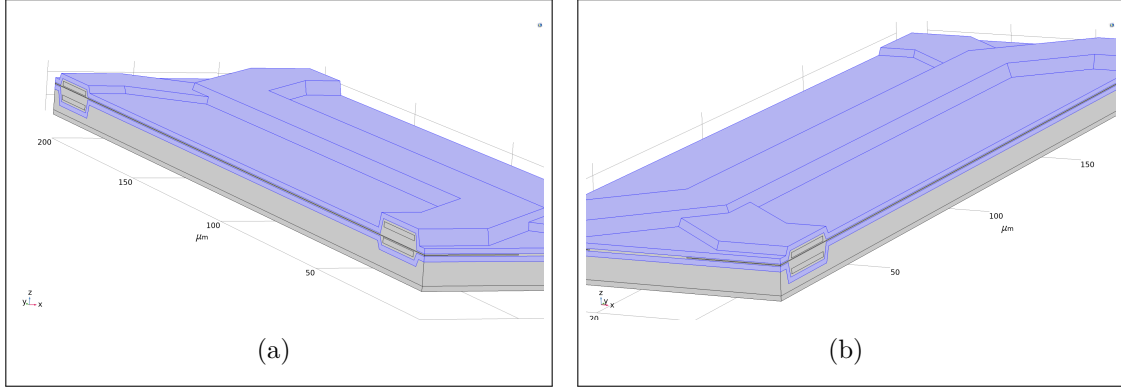


Figure 5.35: 3D structure with super shaped cladding 4 wires: a) from left and b) from right

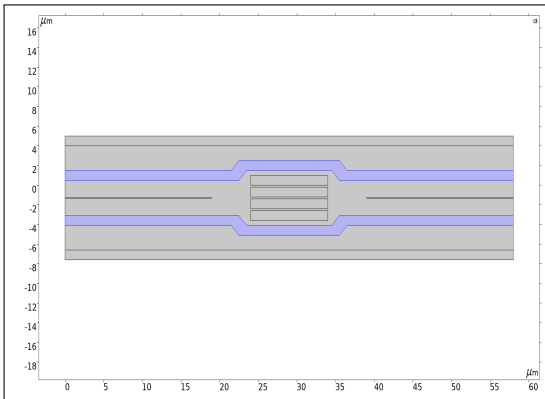


Figure 5.36: 2D view of array structure with shaped cladding 4 wires

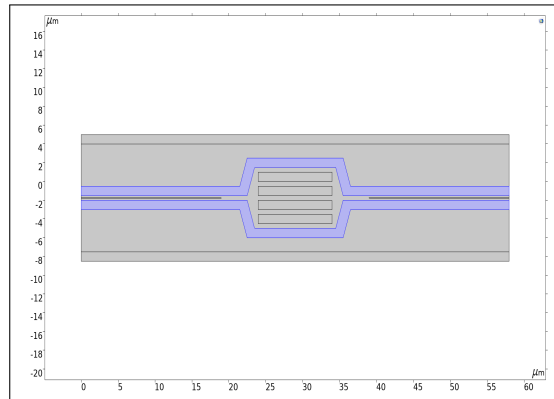


Figure 5.37: 2D view of array structure with super shaped cladding 4 wires

Finally, the field of this structure is compared to the OneWire in fig.5.38 and the values in table 5.6 are extracted. The results are excellent, each parameter is improved by several times: the field 5 times, the area more than 13 times and power density more than 3 times, making this structure the best one even with respect to the ThreeWires of the horizontal array, considering also that the use of even 4 wires is completely compensated and the other geometrical parameters are not changed. For this structure the magnetic component of the loss density Q_{ml} is extracted from COMSOL and its average value is $Q_{ml} = 0.22uW/m^3$, highlighting even more the stability of this structure. Other modifications are not necessary so this is the structure chosen as reference structure from now on.

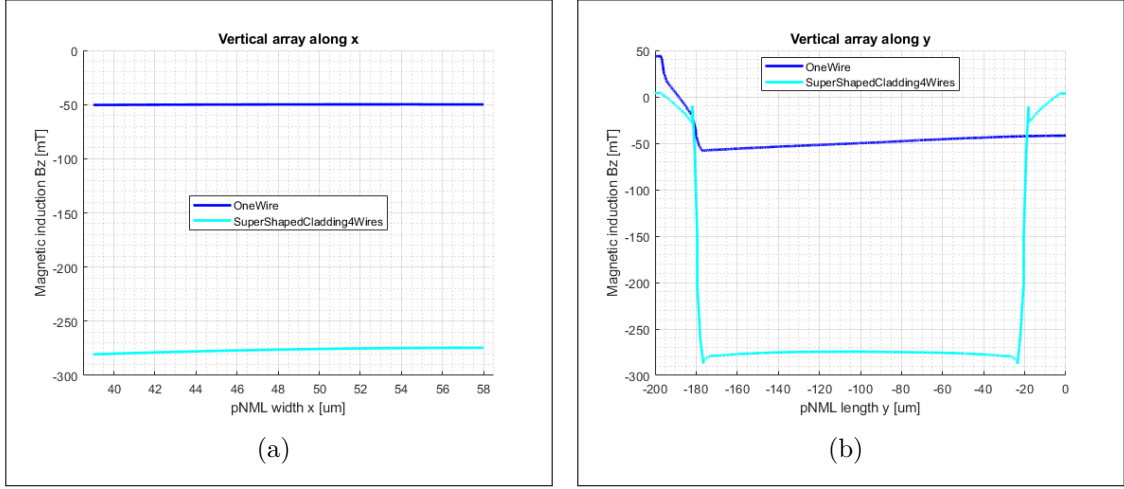


Figure 5.38: Comparison between fields with the array structure with the super shaped cladding 4 wires: a) along x and b) along y

Structure	Medium field[mT]	Available area[μm^2]	Power density[$\mu W/\mu m^2$]
OneWire	-50.11	399	5.17
SSC4	-277.50	5366.12	1.54

Table 5.6: Comparison of values between OneWire and SuperShaped-Cladding4Wires (SSC4)

Since the field obtained with this structure is so high it is possible to decrease the current to get back the original $50mT$ and save on power consumption. The table 5.7 compares the power values also with the first structure OneWire.

Structure	Medium field[mT]	Available area[μm^2]	Power density[$\mu W/\mu m^2$]
SSC4	-277.50	5366.12	1.54
SSC4Eco	-50.58	5366.12	0.05
OneWire	-50.11	399	5.17

Table 5.7: Comparison of values between SuperShapedCladding4Wires (SSC4) and SuperShapedCladding4WiresEco (SSC4Eco)

With respect to the OneWire, with the same field the area is increased more than 13 times and the power is decreased more than 103 times.

Chapter 6

Characterization

In this chapter the structure SuperShapedCladding4Wires is fully characterized since it turned out to be the best one from all points of view. The analysis involves the most important parameters of the structure on which the others depend and a range of usability is given for each of them, so that from a designer's point of view it is possible to know in advance the limits of functioning of the structure. These parameters are extracted from the previous chapters in table 6.1.

Name	Expression	Value	Description
f	1	1	frequency[MHz]
l	200	200	structure length[um]
t_{cl}	1	1	cladding thickness[um]
t_{il}	0.5	0.5	interlayer thickness[um]
t_{pnml}	0.1	0.1	pnml thickness[um]
w_s	48	48	spacing width[um]

Table 6.1: Parameters for the characterization

6.1 Frequency and cladding

The first parameter analyzed is the frequency. In [9] pNML magnets are studied up to $50MHz$ clocking frequency and in [6] and [40] up to $100MHz$ so it is decided to characterize this structure from the initial $1MHz$ up to $300MHz$ since having a working circuit at this high frequency would be an important result and a great step forward for the pNML technology. The frequency sweep is done every $50MHz$ and is depicted in fig.6.1. No other parameters are changed for now and the structure simulated is the last one analyzed, that is the SuperShapedCladding4Wires while the material is still SPy.

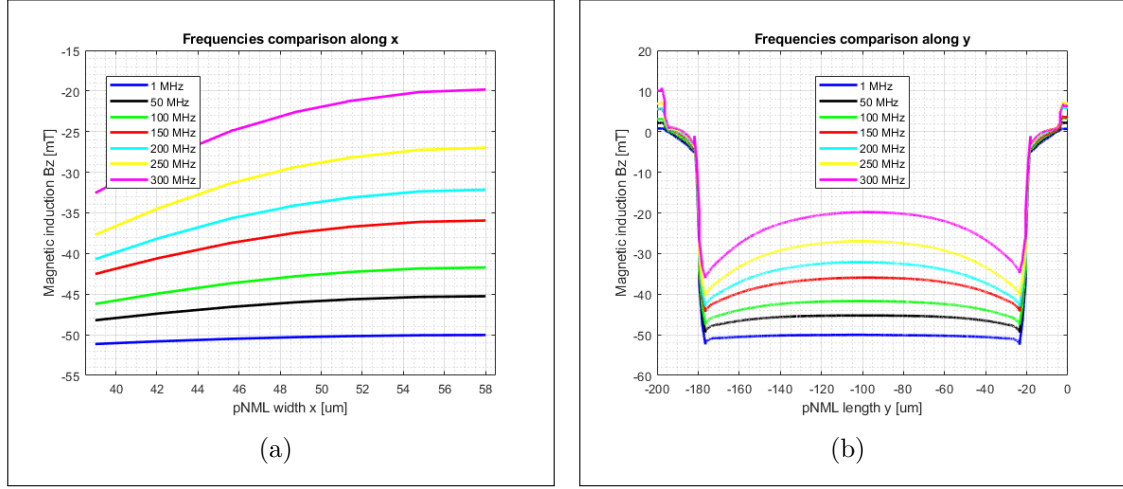


Figure 6.1: Frequency analysis with $t_{cl} = 1\mu m$: a) along x and b) along y

It can be seen that, as expected, as the frequency grows up the field decreases because the leakages increase in the material and it is no longer able to contain the field. In particular the field loses the stability and at last the amplitude becomes less than half. In [45] it is proved that, when the film thickness increases, the real component of the permeability decreases at higher frequencies due to the skin effect and eddy currents presence. So the solution proposed to improve the behaviour of these soft magnetic materials at high frequency is to increase the resistance of the magnetic film by reducing the thickness of the film itself. This means that the following simulations will cover the reduction of the cladding thickness, fig.6.2.

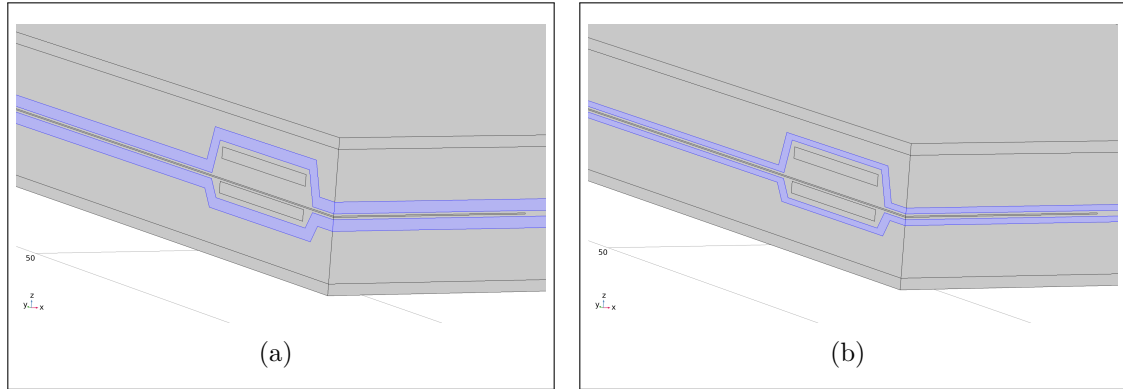


Figure 6.2: Cladding thickness reduction t_{cl} : a) $1\mu m$ and b) $0.5\mu m$

For this reason the frequency sweep is repeated for several values of t_{cl} , each time halving its value and they are reported in fig.6.3, 6.4 and 6.5. The parameterization stopped at $t_{cl} = 0.125\mu m$ because the field at $300MHz$ is practically equal to the

field at $t_{cl} = 0.25\mu m$, but it is interesting to note that the field at low frequencies started to decrease so going further it would be disadvantageous.

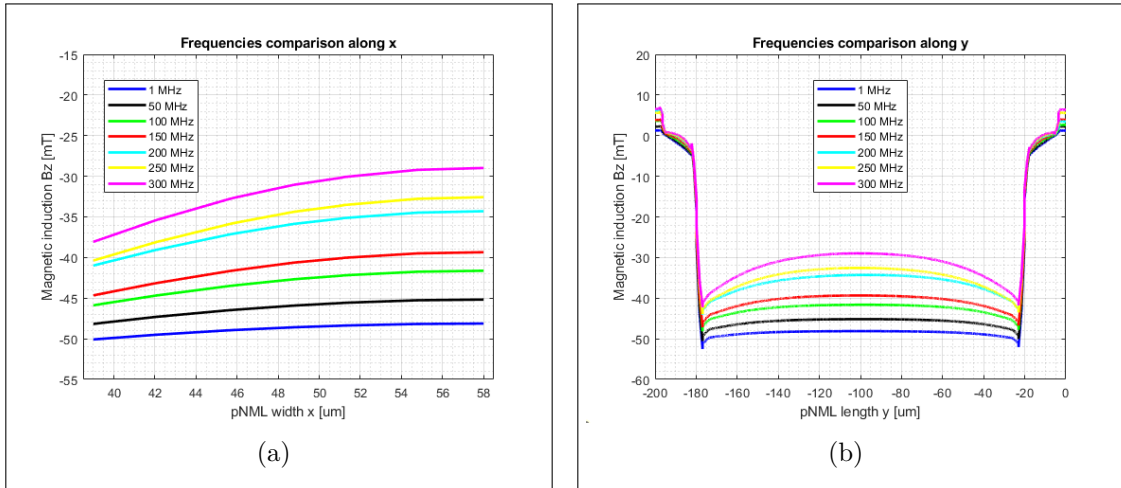


Figure 6.3: Frequency analysis with $t_{cl} = 0.5\mu m$: a) along x and b) along y

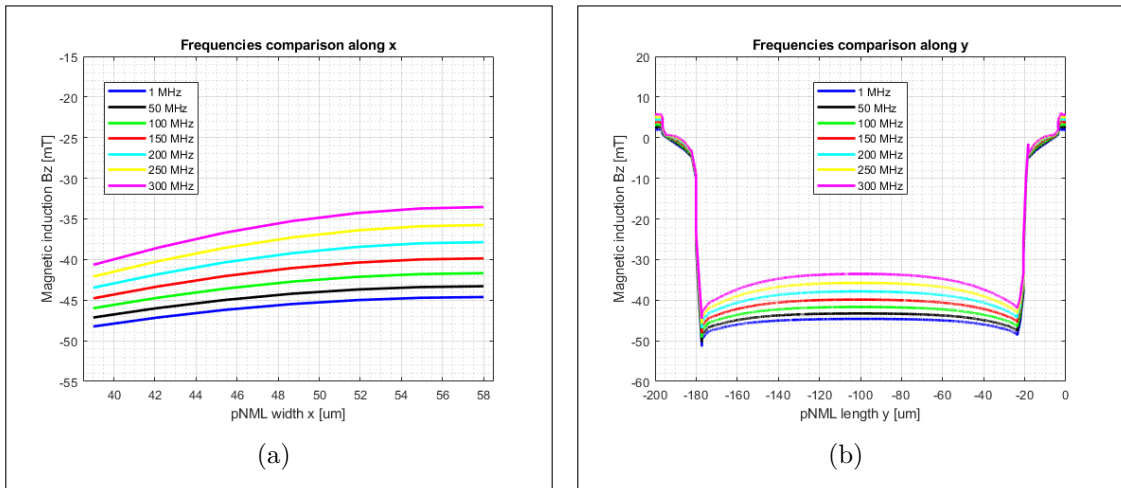


Figure 6.4: Frequency analysis with $t_{cl} = 0.25\mu m$: a) along x and b) along y

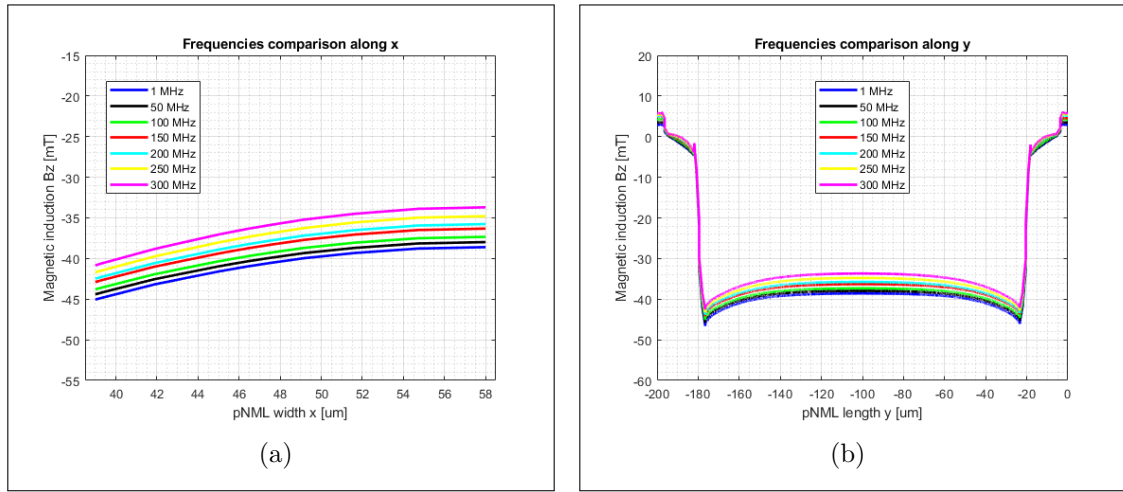


Figure 6.5: Frequency analysis with $t_{cl} = 0.125\mu\text{m}$: a) along x and b) along y

Since the aim is to characterize the 300MHz frequency in fig.6.6 the graphs at 300MHz for different thicknesses are reported together, where it is clear that there is no difference between the last 2 cladding thicknesses for this frequency so there is no reason to go towards smaller, and neither larger values because the field would keep to decrease.

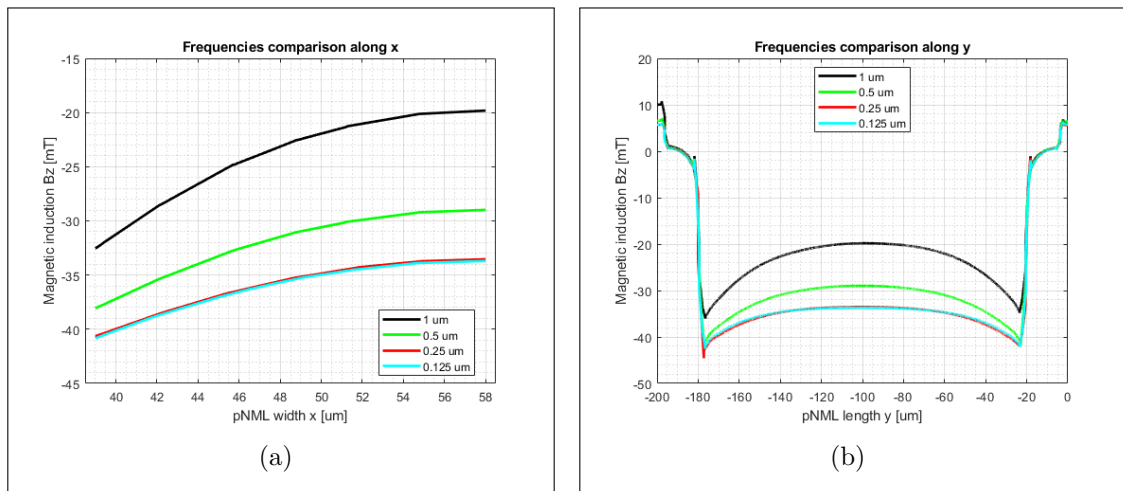


Figure 6.6: Comparison of different cladding thicknesses at 300MHz with the same current: a) along x and b) along y

A better visualization of these graphs can be done showing the several thicknesses with the correct values of current to get the standard 50mT . This is done in fig.6.7.

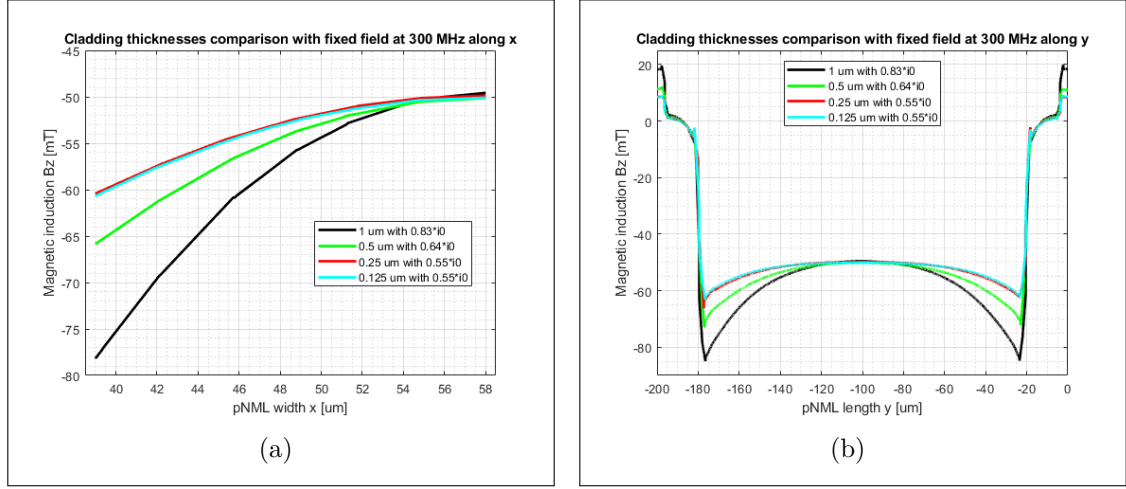


Figure 6.7: Comparison of different cladding thicknesses at 300 MHz with the same field: a) along x and b) along y

Obviously, it turned out that the current is the smallest for the smallest thicknesses because they are those thicknesses that best contain the field. Furthermore, it can be noted that the field is more flat since the leakages tend to decrease when the cladding thickness reduces. As usual, in table 6.2 the values for all the thicknesses are reported. In terms of area and power the best thickness is the last one so this is the value used for the cladding thickness from now on.

Thickness[um]	Available area[um ²]	Power density[uW/um ²]
1	1.97	30815.74
0.5	5.64	5590.78
0.25	10.9	1690.09
0.125	10.82	1204.81

Table 6.2: Comparison of different thicknesses

6.2 Interlayer dielectric

The next parameter analyzed is the thickness of the interlayer dielectric, this is very important because it corresponds to the distance between the cladding armors since the interlayer dielectric fills the space between the layers of wires around the pNML and the cladding armors begin at the level of the wires. This parameter is so important that makes the analysis of the almost all other thicknesses useless because modifying one of them actually means modifying it, therefore is modified by 0.1 at a time. In fig.6.8 it is red line.

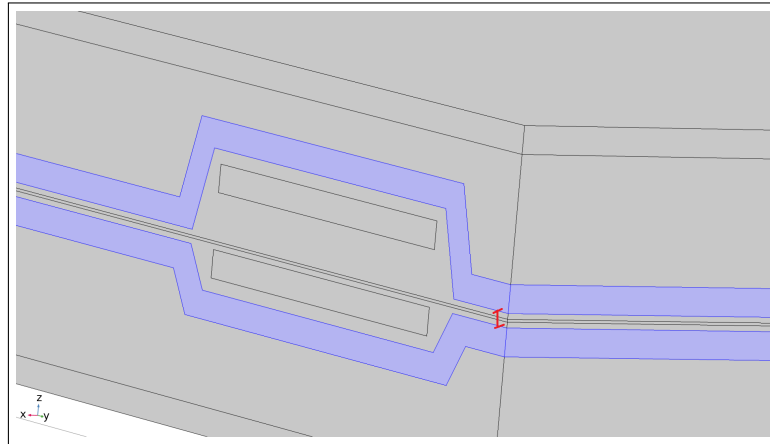


Figure 6.8: Thickness of interlayer dielectric t_{il}

Firstly it is reduced as depicted in fig.6.9 and then increased in fig.6.10 and 6.11. Decreasing the thickness the field increases as expected but there is a huge amplitude loss between the center of the pNML and the sides, this means that in order to respect the tolerance the area would be too small and so the circuit unusable. On the contrary, increasing the thickness leads to a decrease of field amplitude but also to an improvement of stability and so of area and power density. This is why the choice in this case is the $t_{il} = 1.3\mu m$, not beyond because the field is already halved.

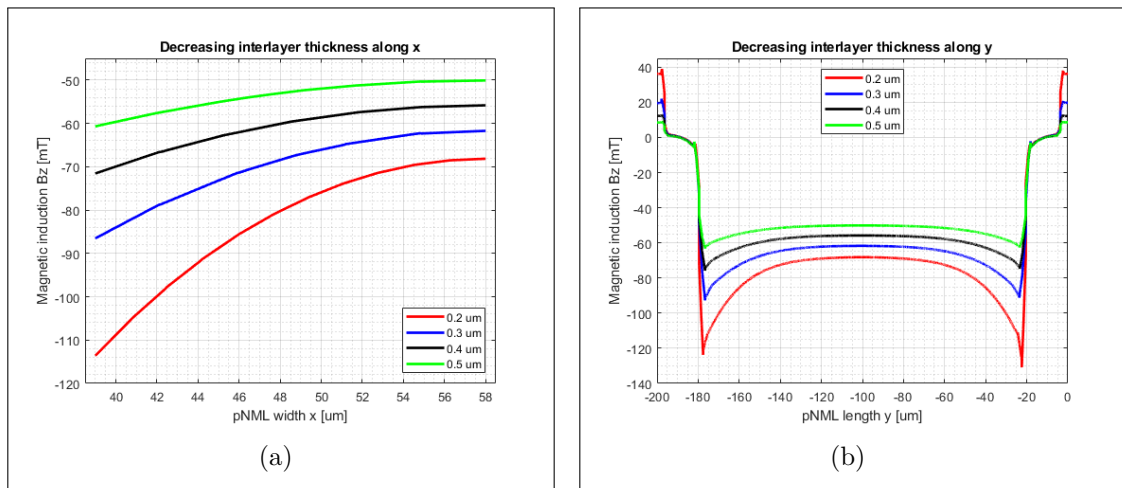


Figure 6.9: Decreasing of interlayer thickness: a) along x and b) along y

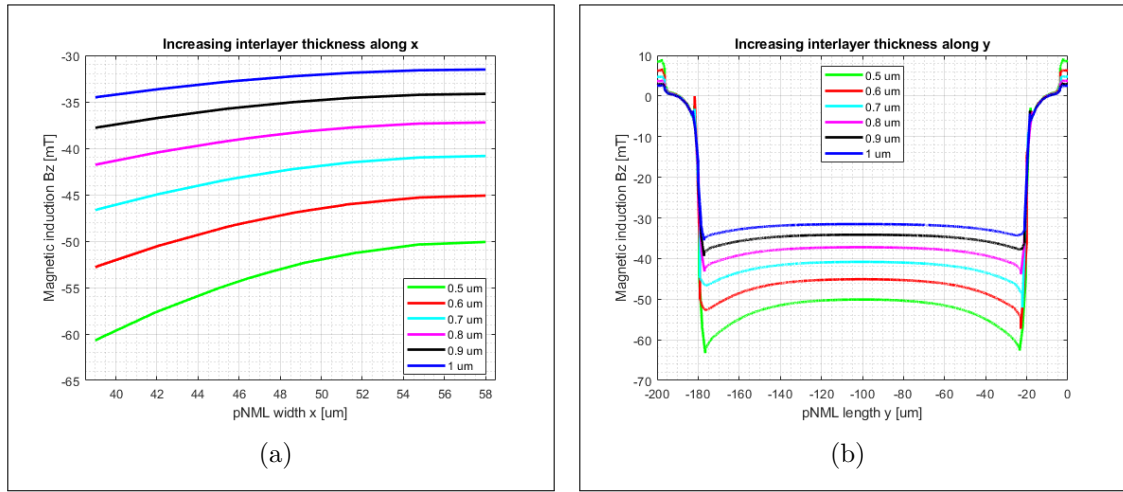


Figure 6.10: Increasing of interlayer thickness: a) along x and b) along y

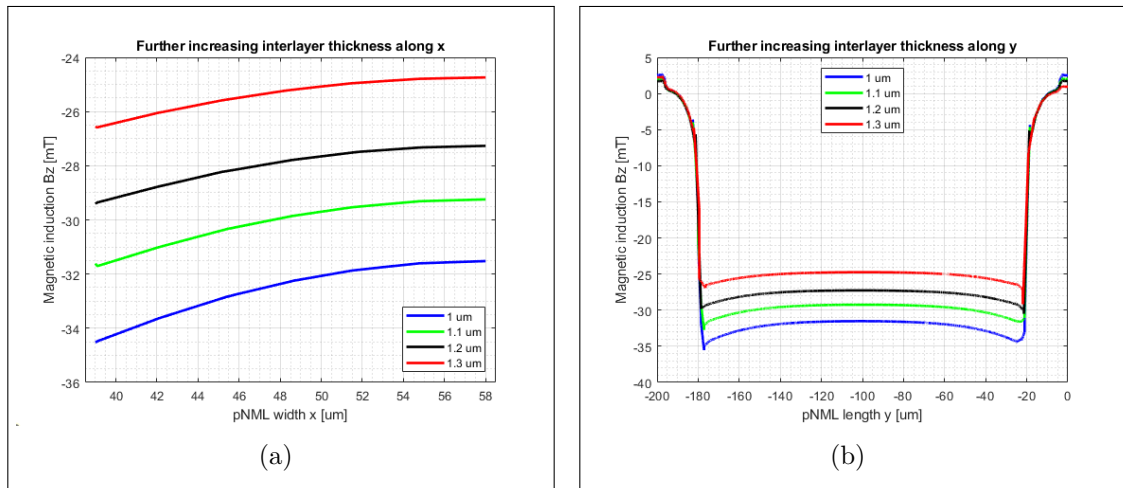


Figure 6.11: Further increasing of interlayer thickness: a) along x and b) along y

6.3 pNML thickness

The pNML thickness is another important parameter to be analyzed because this thickness is linked to the number of layers that can be used in this structure. This parameter should be the biggest possible since in this way more layers can be inserted. This means that it the pNML domain should occupy almost all the space given by the new interlayer thickness as in fig.6.12.

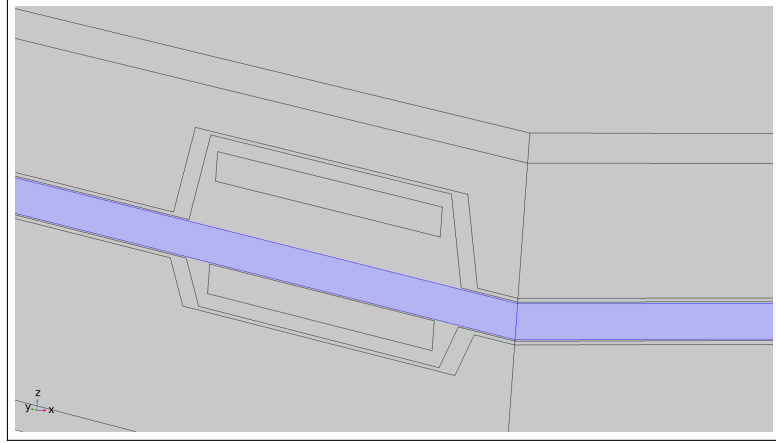


Figure 6.12: Thickness of pNML t_{pnml}

The simulation was done directly for the biggest value $t_{pnml} = 1.2\mu m$ and since the domain is much larger now along z , it is important that the field is the same for all the height of the domain because this means that each pNML layer sees the same field amplitude. The several lines through which the field is represented along z are shown in fig.6.13. In particular, they are located in the central point $-t_{pl} - t_{cu} - t_{il}/2$, at $-t_{pl} - t_{cu} - t_{il}/2 \pm 3\mu m$ in the middle of the upper and lower half and at $-t_{pl} - t_{cu} - t_{il}/2 \pm 6\mu m$ that is the beginning and the end of the domain.

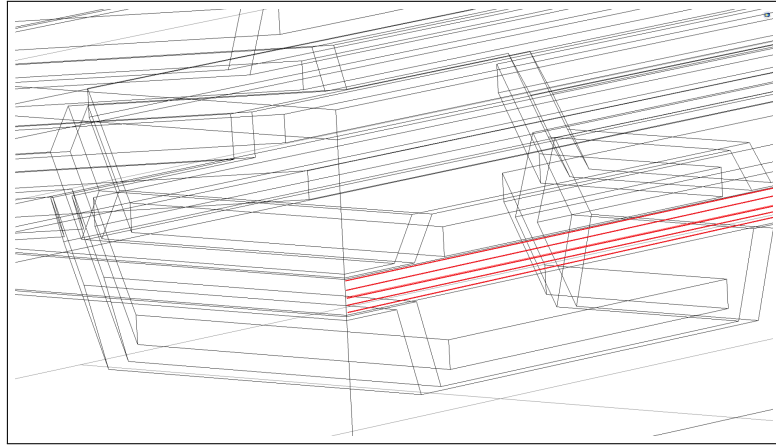


Figure 6.13: Cutlines along z

The field is depicted in fig.6.14. The graphs are almost superimposed and this is a great result because it assures that each pNML, located in any position inside the domain, can be magnetized in the same way with the same field. The starting value was $t_{pnml} = 0.1\mu m$ which means that for a thickness of pNML layer of $10nm$ and considering other $10nm$ of distance between one layer and another 5 layers

could be used in the structure before, now up to 60 layers can be inserted with the awareness that they work in the same way and at $300MHz$. In fig.6.15 the simulation is repeated to get the standard field.

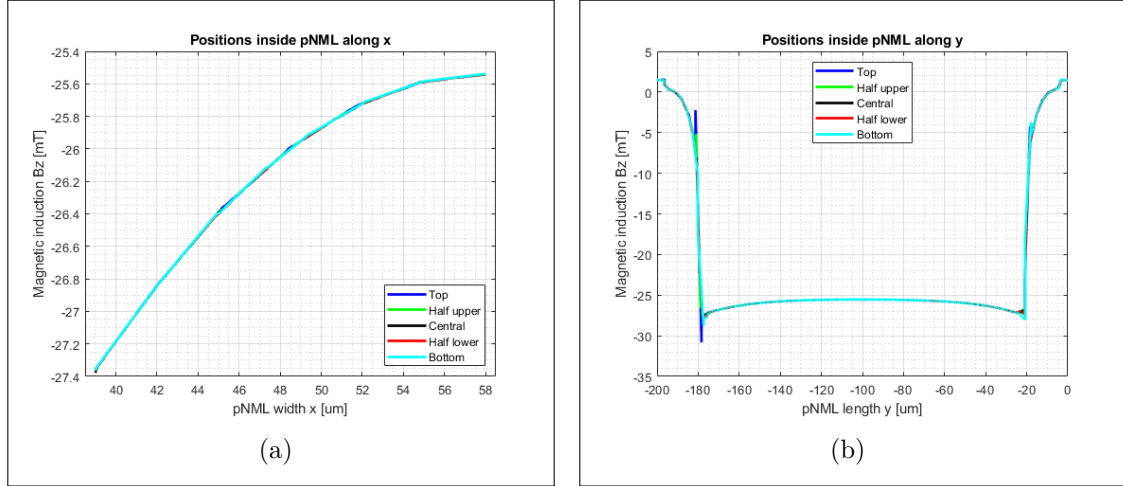


Figure 6.14: Comparison of different heights along z of the pNML thickness: a) along x and b) along y

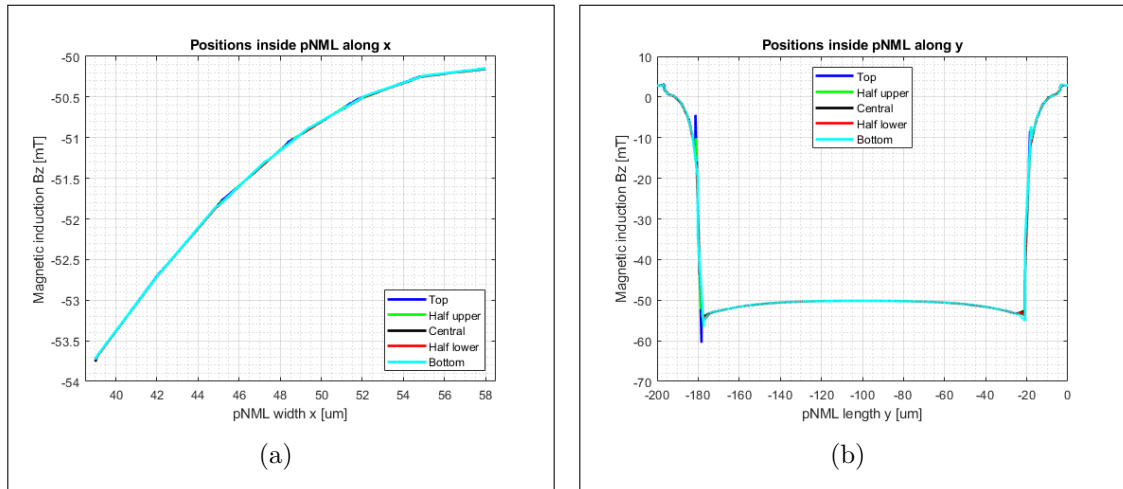


Figure 6.15: Comparison of different heights along z of the pNML thickness with $50mT$: a) along x and b) along y

6.4 pNML area

The last parameters are the other 2 dimensions of the pNML, w_s and l , x and y axes. They are important to understand how much large or long the pNML layer

can be done and consequently the area where the circuitry can be put, fig.6.16.

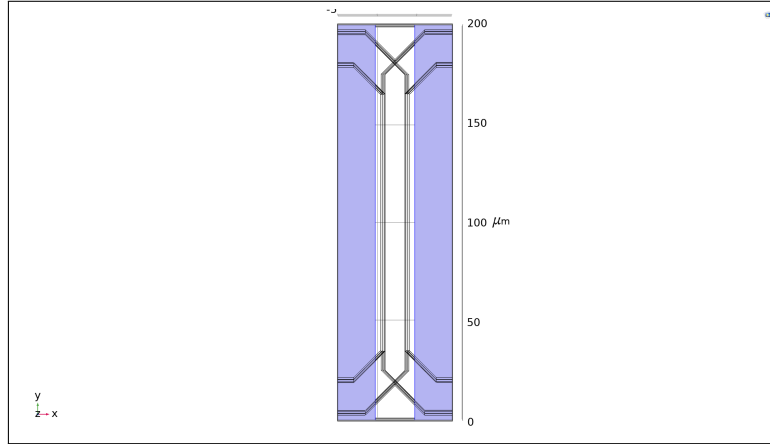


Figure 6.16: pNML area with w_s and l

Since these parameters each represent a reference direction 2 separate and parallel analysis are done so that one does not influence the other one. Starting from the w_s , the values increased and decreased by $2\mu m$ at a time, as in chapter 4 for the same reason, as depicted in fig.6.17 and 6.18 for $50mT$. The table 6.3 compares all these last widths, from the minimum possible $42\mu m$ to a too much big $52\mu m$. This time also the value rms of the power is inserted to see the medium value.

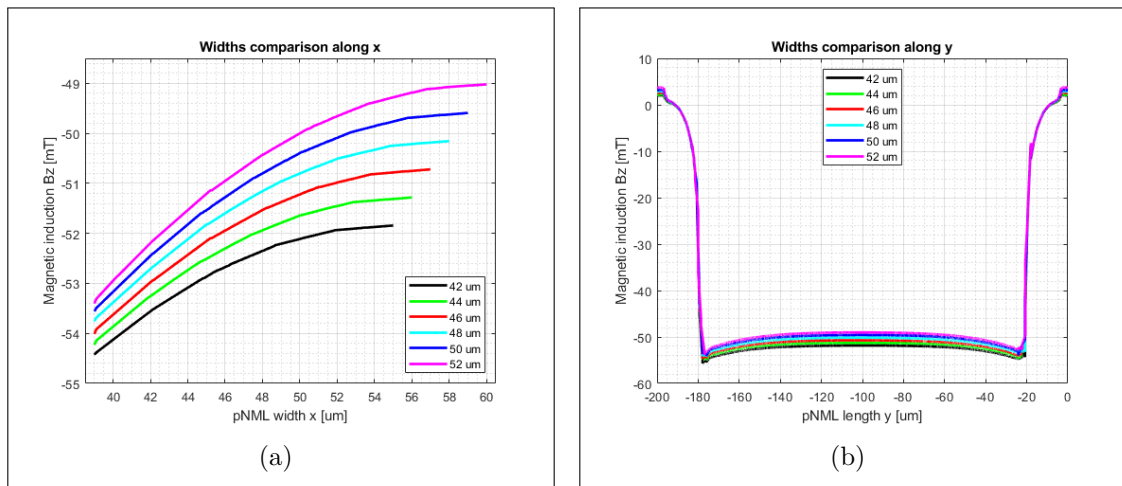


Figure 6.17: Comparison of different widths: a) along x and b) along y

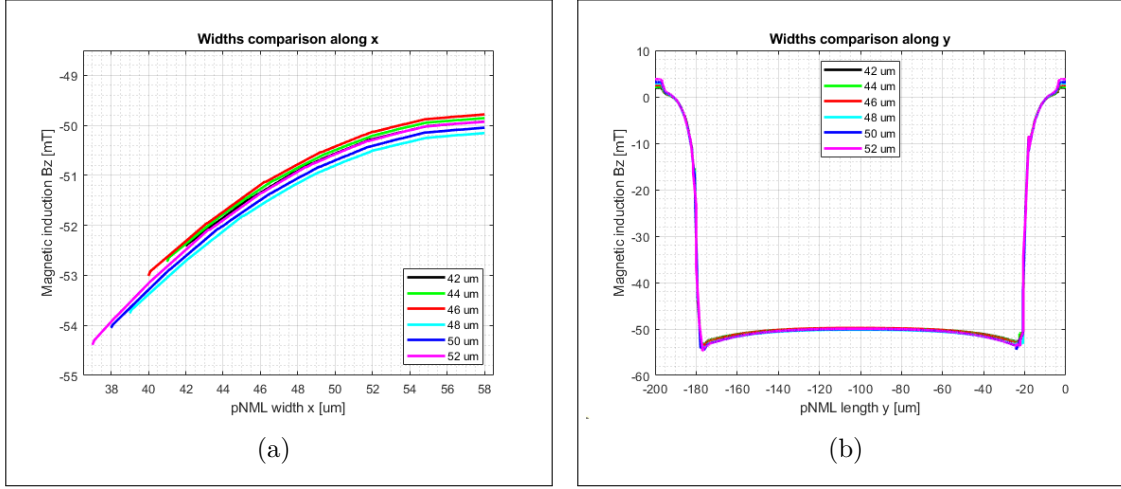


Figure 6.18: Comparison of different widths with 50mT : a) along x and b) along y

Width[μm]	Available area[μm^2]	Power density[$\mu\text{W}/\mu\text{m}^2$]	Power density rms[$\mu\text{W}/\mu\text{m}^2$]
42	287.13	34.68	17.34
44	259.92	42.02	21.01
46	198.65	60.25	30.12
48	176.85	75.29	37.65
50	155.58	93.12	46.56
52	136.42	115.30	57.65

Table 6.3: Comparison of different widths

There is not too much difference between $42\mu\text{m}$ and $44\mu\text{m}$ but the best width is clearly the smallest one.

As regards l , the same simulations were done but after setting the value of width to $48\mu\text{m}$ again, in this way the analysis on w_s is nullified. Decreasing the length by steps of $50\mu\text{m}$ leads to fig.6.19 and 6.20 for the fixed field. In tables 6.4 the values of comparison are reported. The lengths present less area than the starting value so they are neglected.

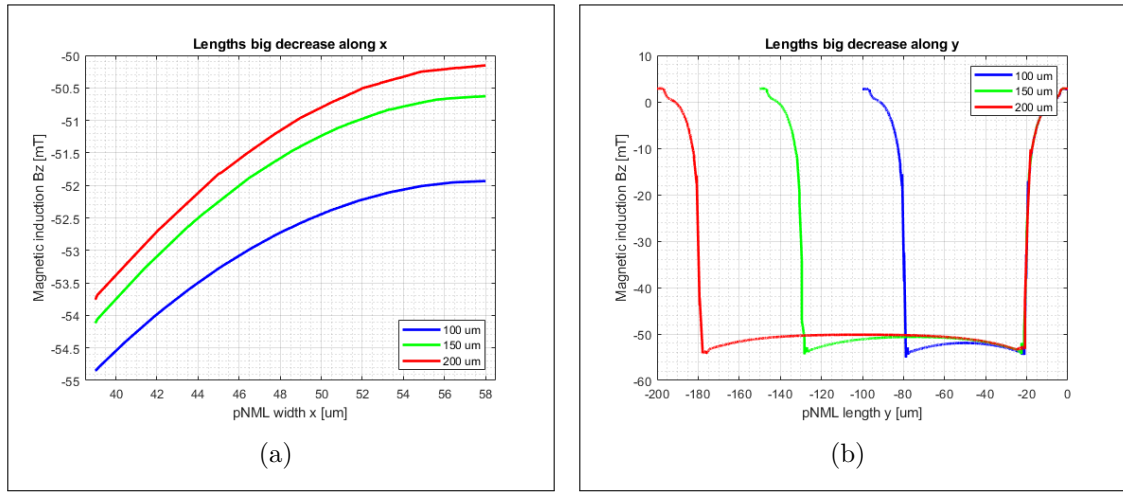


Figure 6.19: Decreasing of different lengths: a) along x and b) along y

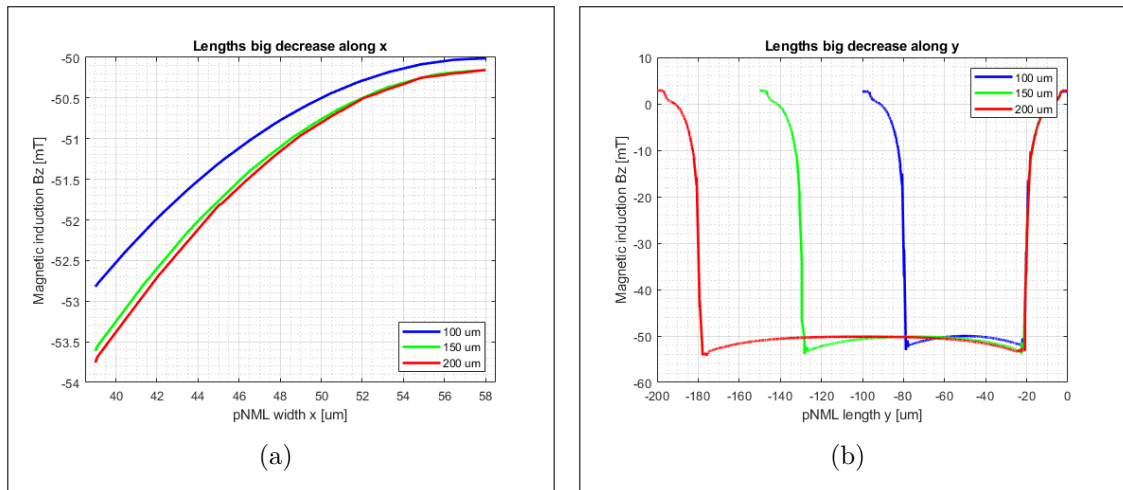


Figure 6.20: Decreasing of different lengths with 50mT: a) along x and b) along y

Width[um]	Available area[um ²]	Power density[uW/um ²]	Power density rms[uW/um ²]
100	169.06	22.43	11.22
150	162.81	51.65	25.82
200	177.69	74.94	37.47

Table 6.4: Comparison of different lengths decreasing

Increasing the length up to 450um turned out to be the confirmation that the best length was still 200um as can be shown in fig.6.21 and 6.22 and in table 6.5.

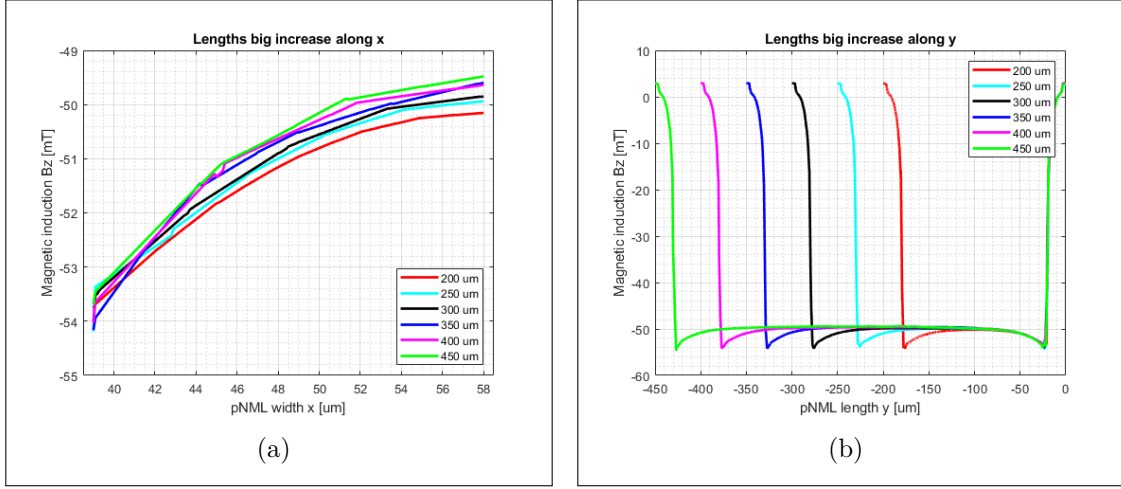


Figure 6.21: Increasing of different lengths: a) along x and b) along y

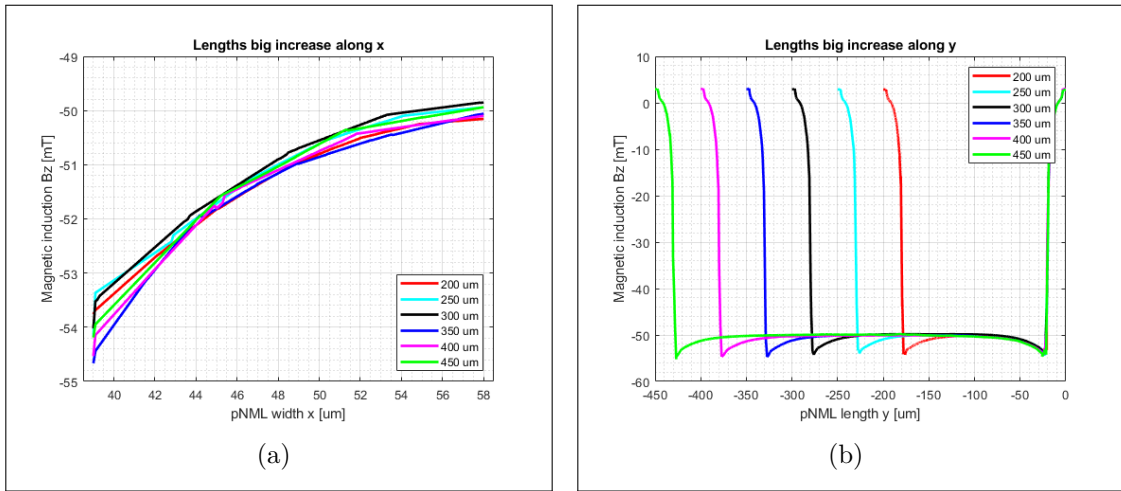


Figure 6.22: Increasing of different lengths with 50mT: a) along x and b) along y

Width[um]	Available area[um ²]	Power density[uW/um ²]	Power density rms[uW/um ²]
200	177.69	74.94	37.47
250	146.3	127.42	63.71
300	158.48	153.11	76.55
350	117.39	260.69	130.34
400	128.52	287.17	143.58
450	137.83	315.50	157.75

Table 6.5: Comparison of different lengths increasing

Since now all the parameters are investigated a final comparison before and after characterization can be done. Fig.6.23 shows the fields of the structure before and after characterization where it can be noted the general improvement of stability of the field and in table 6.6 the comparison between the parameters can be seen, in particularly the area increased more than 145 times and especially the power density dropped drastically.

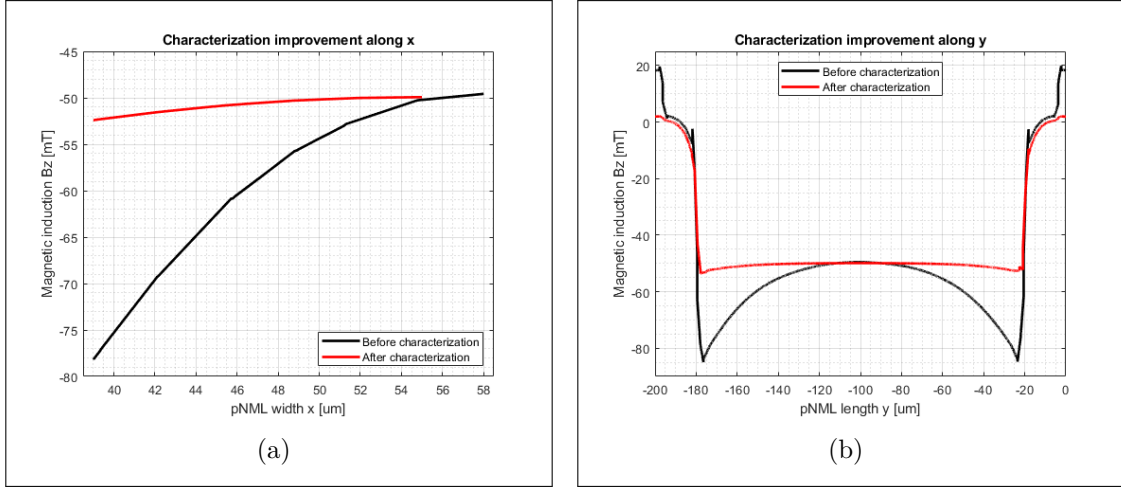


Figure 6.23: Final comparison before and after characterization: a) along x and b) along y

Parameter	Before characterization	After characterization
$f[MHz]$	300	300
$l[um]$	200	200
$t_{cl}[um]$	1	0.125
$t_{il}[um]$	0.5	1.3
$t_{pnml}[um]$	0.1	1.2
$w_s[um]$	48	42
Area[um^2]	1.97	287.13
Power density[uW/um^2]	30815.74	34.68

Table 6.6: Comparison of values before and after characterization

Chapter 7

Conclusions

In this thesis work an 3D pNML structure is discussed. The analysis begins from the state-of-art of pNML technology present in literature of a 2D structure of an on-chip inductor. The importance of clock signal is discussed in chapter 2 where a theoretical background of this new technology is introduced, highlighting the advantages of it with respect the CMOS technology.

The tools exploited to study and analyze this structure are explained in chapter 3, in particular a big attention is given to the geometry and the boundary conditions applied. Understanding the geometry is important to build a structure that works at the maximum of its possibilities and every item that composes this structure has to be carefully engineered before to be placed to avoid leakages. In addition, boundary conditions are needed to save computational time and memory resources. These periodic boundary conditions are based on the symmetry of the structure and are implemented to exploit this symmetry in the case characterized in this work but also, to have a reference cell that gives the possibility to study more general and more complex circuits without the necessity to simulate them.

In chapter 4 the analysis moves to 3D structure, some parameters (like length of the structure and width of pNML) are characterized. To assure a good stability of the field 1% tolerance was chosen as reference and this constraint is kept for all simulations. Good results were obtained and this led to a reference cell to be used as base, proving that it is not necessary to simulate the whole structure, saving computational cost and time.

The design of the structure is discussed in chapter 5 where several kinds of structures are investigated and analyzed. For each of them a power density estimation is given in order to understand which one is preferable in terms of available area also. It turned out that even if increasing the number of wires (up to 4 wires instead of 1) can be a negative solution to increase the field if the cladding is good engineered the results are excellent. Array structures showed that 2 approaches can be followed: equal current with higher field for applications where the amplitude of field is the aim or lower current with the same field when the goal is the saving on power

consumption. Structures for both approaches were obtained and this highlights the versatility of this structure.

Chapter 6 shows a characterization of the most critical parameters to have a complete description and control of the structure. Frequency was increased up to $300MHz$ because in literature the maximum frequency is around $100MHz$, so this allows to use the pNML circuitry at higher speeds, while every other parameter was tested for high range of values giving the behaviour in most cases up to the limits of working. In this way a designer can be aware of these limits and the pros and cons of each choice. The most important parameter was the distance between the cladding armors so much effort was put into studying this factor to get the best from this structure. The final comparison with the structure before characterization shows the goodness of the analysis and interesting results that may be can be the starting point for further investigations in the future.

Bibliography

- [1] Irina Eichwald. *Perpendicular Nanomagnetic Logic: Three-dimensional devices for non-volatile field-coupled computing*. PhD thesis, Technische Universität München, 2015.
- [2] *Soft Magnetic Applications Guide*.
- [3] João G. Nizer Rahmeier, Túlio G. Resende, Luiz G. C. Melo, and Omar P. Vilela Neto. A novel crossing device for in-plane nanomagnetic logic circuits. *IEEE*, 2018.
- [4] Marco Vacca. *Emerging Technologies - NanoMagnets Logic (NML)*. PhD thesis, Politecnico di Torino, April 2013.
- [5] Samira Sayedsalehi and Zeinab Azadi Motlagh. Characterisation of a perpendicular nanomagnetic cell and design of reversible xor gates based on perpendicular nanomagnetic cells. *IET*, 20 December 2019.
- [6] Mohmmad T. Alam, Jarett DeAngelis, Michael Putney, X. Sharon Hu, Wolfgang Porod, Michael Niemier, and Gary H. Bernstein. Clocking scheme for nanomagnet qca. *IEEE*, 2007.
- [7] Debanjan Bhowmik, Long You, and Sayeef Salahuddin. Spin hall effect clocking of nanomagnetic logic without a magnetic field. *Nature Nanotechnology*, 17 November 2013.
- [8] Qianchang Wang, Jin-Zhao Hu, Cheng-Yen Liang, Abdon Sepulveda, and Greg Carman. Voltage-induced strain clocking of nanomagnets with perpendicular magnetic anisotropies. *Nature*, 6 March 2019.
- [9] M. Becherer, J. Kiermaier, S. Breitzkreutz, I. Eichwald, G. Ziemys, G. Csaba, and D. Schmitt-Landsiedel. Towards on-chip clocking of perpendicular nanomagnetic logic. *ScienceDirect*, 4 July 2014.
- [10] M. Jeong, K. Guarini, V. Chan, K. Bernstein, R. Joshi, J. Kedzierski, and W. Haensch. Three dimensional cmos devices and integrated circuits. *IEEE*, September 2003.
- [11] The international technology roadmap for semiconductors. *IEEE*, 2012.
- [12] Michael Niemier, X. Sharon Hu, Aaron Dingler, M. Tanvir Alam, G. Bernstein, and W. Porod. Bridging the gap between nanomagnetic devices and circuits. *IEEE*, 2008.
- [13] Aaron Dingler, M. Jafar Siddiq, Michael Niemier, X. Sharon Hu, M. Tanvir

- Alam, Gary Bernstein, and Wolfgang Porod. Controlling magnetic circuits: How clock structure implementation will impact logical correctness and power. *IEEE*, 2009.
- [14] Mohammad Tanvir Alam, Mohammad Jafar Siddiq, Gary H. Bernstein, Michael Niemier, Wolfgang Porod, and Xiaobo Sharon Hu. On-chip clocking for nanomagnet logic devices. *IEEE*, 2010.
- [15] The international technology roadmap for semiconductors. *IEEE*, 2009.
- [16] The international technology roadmap for semiconductors. *IEEE*, 2013.
- [17] The international technology roadmap for semiconductors. *IEEE*, 2007.
- [18] L. Solymar and D. Walsh. Electrical properties of materials. *Oxford University Press*, 2003.
- [19] *Magnetic Materials: Soft Magnets*.
- [20] S. Lee and H. Chang. Magnetic bubble logic. *IEEE*, December 1974.
- [21] C. Lent, P. Tougaw, W. Porod, and G. Bernstein. Quantum cellular automata. *Nanotechnology*, 1993.
- [22] G. L. Snider et al. Quantum-dot cellular automata: Line and majority logic gate. *Japanese Journal of Applied Physics*, 1999.
- [23] G. Csaba, A. Imre, G. Bernstein, W. Porod, and V. Metlushko. Nanocomputing by field-coupled nanomagnets. *IEEE*, December 2002.
- [24] A. Imre, G. Csaba, L. Ji, A. Orlov, G. Bernstein, and W. Porod. Majority logic gate for magnetic quantum-dot cellular automata. *IEEE*, 2006.
- [25] Mohammad Tanvir Alam, Steven J. Kurtz, Mohammad Abu Jafar Siddiq, Michael T. Niemier, Gary H. Bernstein, Xiaobo Sharon Hu, and Wolfgang Porod. On-chip clocking of nanomagnet logic lines and gates. *IEEE*, March 2012.
- [26] M. Becherer et al. Focused ion beam structured co/pt multilayers for field-coupled magnetic computing. *MRS Proceedings*, 2007.
- [27] M. Becherer, G. Csaba, R. Emling, W. Porod, P. Lugli, and D. Schmitt-Landsiedel. Field-coupled nanomagnets for interconnect-free nonvolatile computing. *IEEE*, February 2009.
- [28] S. Breitzkreutz, J. Kiermaier, I. Eichwald, X. Ju, G. Csaba, D. Schmitt-Landsiedel, and M. Becherer. Majority gate for nanomagnetic logic with perpendicular magnetic anisotropy. *IEEE*, 2012.
- [29] M. Alam, G.H. Bernstein, J. Bokor, D. Carlton, X.S. Hu, S. Kurtz, B. Lambson, M.T. Niemier, W. Porod, M. Siddiq, and E. Varga. Experimental progress of and prospects for nanomagnet logic (nml). *IEEE*, 2009.
- [30] Simon Mendisch, Grazvydas Ziemys, Valentin Ahrens, Adam Papp, and Markus Becherer. Pt/co/w as a candidate for low power nanomagnetic logic. *ScienceDirect*, 2019.
- [31] Simon Mendisch, Valentin Ahrens, Martina Kiechle, Adam Papp, and Markus Becherer. Perpendicular nanomagnetic logic based on low anisotropy co/ni multilayer. *ScienceDirect*, 2020.

- [32] R. P. Cowburn and M. E. Welland. Room temperature magnetic quantum cellular automata. *Science*, 2000.
- [33] M. C. B. Parish and M. Forshaw. Physical constraints on magnetic quantum cellular automata. *Applied Physics Letters*, 2003.
- [34] Grazvydas Ziemys, Andrew Giebfried, Markus Becherer, Irina Eichwald, Doris Schmitt-Landsiedel, and Stephan Breitzkreutz v. Gamm. Modelling and simulation of nanomagnetic logic with cadence virtuoso using verilog-a. 2015.
- [35] G. Turvani, F. Riente, E. Plozner, M. Vacca, M. Graziano, and S. Breitzkreutz v. Gamm. A pnml compact model enabling the exploration of three-dimensional architectures. *IEEE*, May 2017.
- [36] M.T. Alam, S. Kurtz, M.T. Niemier, S.X. Hu, G.H. Bernstein, and W. Porod. Magnetic logic based on coupled nanomagnets: Clocking structures and power analysis. *IEEE*, 2008.
- [37] Mohammad T. Alam, Michael Niemier, Wolfgang Porod, Sharon Hu, Michael Putney, Jarett DeAngelis, and Gary H. Bernstein. On-chip clocking scheme for nanomagnet qca. *IEEE*, 2007.
- [38] M. Becherer, J. Kiermaier, S. Breitzkreutz, G. Csaba, X. Ju, J. Rezgani, T. Kießling, C. Yilmaz, P. Osswald, P. Lugli, and D. Schmitt-Landsiedel. On-chip extraordinary hall-effect sensors for characterization of nanomagnetic logic devices. *ScienceDirect*, 23 May 2010.
- [39] Grazvydas Ziemys, Andrew Giebfried, Markus Becherer, Irina Eichwald, Doris Schmitt-Landsiedel, and Stephan Breitzkreutz v. Gamm. Modeling and simulation of nanomagnetic logic with cadence virtuoso using verilog-a. *ScienceDirect*, 9 June 2016.
- [40] M.T. Niemier, X.S. Hu, M. Alam, G. Bernstein, W. Porod, M. Putney, and J. DeAngelis. Clocking structures and power analysis for nanomagnet-based logic devices. *IEEE*, 2007.
- [41] Ruan Evangelista Formigoni, Omar P. Vilela Neto, and José Augusto M. Nacif. Bancs: Bidirectional alternating nanomagnetic clocking scheme. *IEEE*, 2018.
- [42] Yabo Chen, Xiaokuo Yang, Bo Wei, Huanqing Cui, and Mingxu Song. Proposal of global strain clocking scheme for majority logic gate. *IEEE Access*, 8 May 2020.
- [43] Luqiao Liu, Chi-Feng Pai, Y. Li, H.W. Tseng, D.C. Ralph, and R.A. Buhrman. Spin-torque switching with the giant spin hall effect of tantalum. *Science*, 4 May 2012.
- [44] Michael Niemier. Clocking with no field. *Nature Nanotechnology*, January 2014.
- [45] Donald S.Gardner, Gerhard Schrom, Fabrice Paillet, Brice Jamieson, Tanay Karnik, and Shekhar Borkar. Review of on-chip inductor structures with magnetic films. *IEEE*, October 2009.
- [46] *COMSOL Multiphysics Reference Manual*.
- [47] *AC/DC Module User's Guide*.

- [48] D. Meeker. *AC/DC Module User's Guide*.
- [49] Michael Glickman, Trevor Niblock, Jere Harrison, Ira B. Goldberg, Peter Tseng, and Jack W. Judy. High permeability permalloy for mems. *Research-Gate*, June 2010.
- [50] M. Becherer, J. Kiermaier, S. Breitzkreutz, I. Eichwald, G. Csaba, and D. Schmitt-Landsiedel. Nanomagnetic logic clocked in the mhz regime. *IEEE*, 2013.
- [51] F. Riente, S. Mendisch, L. Gnoli, V. Ahrens, M. Ruo Roch, and M. Becherer. Ta/cofeb/mgo analysis for low power nanomagnetic devices. *IEEE*, 1 November 2020.
- [52] Stephan Breitzkreutz, Irina Eichwald, Josef Kiermaier, Adam Papp, György Csaba, Michael Niemier, Wolfgang Porod, Doris Schmitt-Landsiedel, and Markus Becherer. 1-bit full adder in perpendicular nanomagnetic logic using a novel 5-input majority gate. *EPJ Web of Conferences*, 2014.

Appendix

In this appendix MATLAB scripts are placed following the order of the chapters where they are used.

From 2D to 3D

-B-H curves

```
clc
clear
close all

%CoZrTa
bhcurve_CoZrTa=[0.000000,0.232000,0.435000,0.667000,0.841000,1.102000,1.276000,...
    1.450000,1.508000,1.509000,1.510000,1.511000,1.512000,1.513000,1.514;
    0.000000,159.200000,318.300000,477.460000,636.600000,795.800000,954.900000,...
    1114.000000,1273.000000,1432.000000,1590.000000,1750.000000,1910.000000,...
    2069.000000,20690;]';

%NiFe
bhcurve_NiFe=[0,0.25,0.5,0.75,1,1.15,1.25,1.3,1.31,1.315,1.325;
    0,39.75,79.5,119.25,159,238,318,397,477,4770,47777;]';

%SPy
bhcurve_SPy=[0.000000,0.454790,0.474194,0.476662,0.523547,0.605839,0.687046,...
    0.732109,0.740117,0.741382,0.741924,0.750889,0.753982,0.758531,0.770701,...
    0.776870,0.780475,0.783693,0.783821,0.784761,0.786834,0.787085,0.790164,...
    0.807171,0.811842,0.818476,0.822949,0.853249,0.863568,0.912163,0.926391,...
    0.956031,0.967205,1.193458;
    0.000000,0.892768,0.969937,0.980041,1.205765,2.067835,5.839935,13.972584,...
    17.198823,17.743181,17.928453,23.487712,26.883885,31.417053,70.652864,...
    201.802675,508.838971,820.672016,829.243992,1337.462140,2683.272428,...
    2855.915226,5057.828807,20147.658436,23792.111111,28985.489712,...
    32495.773663,56366.695473,64519.666667,102985.740741,114262.716049,...
    137768.312757,146633.374486,326330.000000;]';

figure(1)
plot(bhcurve_CoZrTa(:,2),bhcurve_CoZrTa(:,1),'b')
hold on
plot(bhcurve_NiFe(:,2),bhcurve_NiFe(:,1),'g')
hold on
plot(bhcurve_SPy(:,2),bhcurve_SPy(:,1),'r')
grid on, grid MINOR
xlim([0 1500])
ylim([0 1.6])
```

Appendix

```
title('BH curves')
xlabel('Magnetic field H [kA/m]')
ylabel('Magnetic induction B [mT]')
legend('CoZrTa', 'NiFe', 'SPy', 'Location', 'best')
```

-Field of 2D structure

```

clc
clear
close all

%%x component
x=readmatrix('Field2D.xlsx','Sheet',1,'Range','A2:A402');
x=x/1000;

xCoZrTa1=real(readmatrix('Field2D.xlsx','Sheet',1,'Range','B2:B402'));
xNiFe1=real(readmatrix('Field2D.xlsx','Sheet',2,'Range','B2:B402'));
xSPy1=real(readmatrix('Field2D.xlsx','Sheet',3,'Range','B2:B402'));

xCoZrTa50=real(readmatrix('Field2D.xlsx','Sheet',1,'Range','D2:D402'));
xNiFe50=real(readmatrix('Field2D.xlsx','Sheet',2,'Range','D2:D402'));
xSPy50=real(readmatrix('Field2D.xlsx','Sheet',3,'Range','D2:D402'));

figure(1)
plot(x,xCoZrTa1,'b','Linewidth',1)
hold on
plot(x,xNiFe1,'g','Linewidth',1)
hold on
plot(x,xSPy1,'r','Linewidth',1)
hold on
plot(x,xCoZrTa50,'b--','Linewidth',1)
hold on
plot(x,xNiFe50,'g--','Linewidth',1)
hold on
plot(x,xSPy50,'r--','Linewidth',1)
grid on, grid MINOR
xlim([39.5 80.5])
title('Field 2D')
xlabel('pNML width x [um]')
ylabel('Magnetic induction By [mT]')
legend('CoZrTa - 1 MHz','NiFe - 1 MHz','SPy - 1 MHz',...
       'CoZrTa - 50 MHz','NiFe - 50 MHz','SPy - 50 MHz','Location','best')

```

-3D analysis

```

clc
clear
close all

%%x component
x=readmatrix('FirstAnalysis.xlsx','Sheet',1,'Range','A2:A402');
x=x/1000;

x50=real(readmatrix('FirstAnalysis.xlsx','Sheet',1,'Range','B2:B402'));
x120=real(readmatrix('FirstAnalysis.xlsx','Sheet',2,'Range','B2:B402'));
x200=real(readmatrix('FirstAnalysis.xlsx','Sheet',3,'Range','B2:B402'));
xShaped=real(readmatrix('FirstAnalysis.xlsx','Sheet',4,'Range','B2:B402'));
xShapedReal=real(readmatrix('FirstAnalysis.xlsx','Sheet',5,'Range','B2:B402'));

%%y component
y501=readmatrix('FirstAnalysis.xlsx','Sheet',1,'Range','C2:C4002');
y502=readmatrix('FirstAnalysis.xlsx','Sheet',1,'Range','C4003:C4902');
y503=readmatrix('FirstAnalysis.xlsx','Sheet',1,'Range','C4903:C5002');
y50=[y501/1000; y502/10000; y503];

Bzy_501=real(readmatrix('FirstAnalysis.xlsx','Sheet',1,'Range','D2:D4002'));
Bzy_502=real(readmatrix('FirstAnalysis.xlsx','Sheet',1,'Range','D4003:D4902'));
Bzy_503=real(readmatrix('FirstAnalysis.xlsx','Sheet',1,'Range','D4903:D5002'));
Bzy_50=[Bzy_501; Bzy_502; Bzy_503];

y1201=readmatrix('FirstAnalysis.xlsx','Sheet',2,'Range','C2:C2002');
y1202=readmatrix('FirstAnalysis.xlsx','Sheet',2,'Range','C2003:C11002');
y1203=readmatrix('FirstAnalysis.xlsx','Sheet',2,'Range','C11003:C11902');
y1204=readmatrix('FirstAnalysis.xlsx','Sheet',2,'Range','C11903:C12002');
y120=[y1201; y1202/1000; y1203/10000; y1204];

Bzy_1201=real(readmatrix('FirstAnalysis.xlsx','Sheet',2,'Range','D2:D2002'));
Bzy_1202=real(readmatrix('FirstAnalysis.xlsx','Sheet',2,'Range','D2003:D11002'));
Bzy_1203=real(readmatrix('FirstAnalysis.xlsx','Sheet',2,'Range','D11003:D11902'));
Bzy_1204=real(readmatrix('FirstAnalysis.xlsx','Sheet',2,'Range','D11903:D12002'));
Bzy_120=[Bzy_1201; Bzy_1202; Bzy_1203; Bzy_1204];

y2001=readmatrix('FirstAnalysis.xlsx','Sheet',3,'Range','C2:C10002');
y2002=readmatrix('FirstAnalysis.xlsx','Sheet',3,'Range','C10003:C19002');
y2003=readmatrix('FirstAnalysis.xlsx','Sheet',3,'Range','C19003:C20002');
y200=[y2001; y2002/1000; y2003/10000];

Bzy_2001=real(readmatrix('FirstAnalysis.xlsx','Sheet',3,'Range','D2:D10002'));
Bzy_2002=real(readmatrix('FirstAnalysis.xlsx','Sheet',3,'Range','D10003:D19002'));
Bzy_2003=real(readmatrix('FirstAnalysis.xlsx','Sheet',3,'Range','D19003:D20002'));
Bzy_200=[Bzy_2001; Bzy_2002; Bzy_2003];

Bzy_Shaped1=real(readmatrix('FirstAnalysis.xlsx','Sheet',4,'Range','D2:D10002'));
Bzy_Shaped2=real(readmatrix('FirstAnalysis.xlsx','Sheet',4,'Range','D10003:D19002'));
Bzy_Shaped3=real(readmatrix('FirstAnalysis.xlsx','Sheet',4,'Range','D19003:D20002'));
Bzy_Shaped=[Bzy_Shaped1; Bzy_Shaped2; Bzy_Shaped3];

Bzy_ShapedReal1=real(readmatrix('FirstAnalysis.xlsx','Sheet',5,'Range','D2:D10002'));
Bzy_ShapedReal2=real(readmatrix('FirstAnalysis.xlsx','Sheet',5,'Range','D10003:D19002'));
Bzy_ShapedReal3=real(readmatrix('FirstAnalysis.xlsx','Sheet',5,'Range','D19003:D20002'));
Bzy_ShapedReal=[Bzy_ShapedReal1; Bzy_ShapedReal2; Bzy_ShapedReal3];

figure(1)
plot(x,x50,'b','Linewidth',2)
hold on

```

```

plot(x,x120,'r','Linewidth',2)
hold on
plot(x,x200,'g','Linewidth',2)
grid on, grid MINOR
title('Several lengths along x')
xlim([39.5 80.5])
xlabel('pNML width x [um]')
ylabel('Magnetic induction Bz [mT]')
legend('50 um','120 um','200 um','Location','best')

figure(2)
plot(-y50-150,Bzy_50,'b','Linewidth',2)
hold on
plot(-y120-80,Bzy_120,'r','Linewidth',2)
hold on
plot(-y200,Bzy_200,'g','Linewidth',2)
grid on, grid MINOR
title('Several lengths along y')
xlabel('pNML length y [um]')
ylabel('Magnetic induction Bz [mT]')
legend('50 um','120 um','200 um','Location','best')

figure(3)
plot(x,x200,'g','Linewidth',2)
hold on
plot(x,xShaped,'m','Linewidth',2)
grid on, grid MINOR
title('Not Shaped vs Shaped along x')
xlim([39.5 80.5])
xlabel('pNML width x [um]')
ylabel('Magnetic induction Bz [mT]')
legend('200 um','Shaped','Location','best')

figure(4)
plot(-y200,Bzy_200,'g','Linewidth',2)
hold on
plot(-y200,Bzy_Shaped,'m','Linewidth',2)
grid on, grid MINOR
title('Not Shaped vs Shaped along y')
xlabel('pNML length y [um]')
ylabel('Magnetic induction Bz [mT]')
legend('200 um','Shaped','Location','best')

figure(5)
plot(x,xShaped,'m','Linewidth',2)
hold on
plot(x,xShapedReal,'c','Linewidth',2)
grid on, grid MINOR
title('Shaped vs ShapedReal along x')
xlim([39.5 80.5])
xlabel('pNML width x [um]')
ylabel('Magnetic induction Bz [mT]')
legend('Shaped','ShapedReal','Location','best')

figure(6)
plot(-y200,Bzy_Shaped,'m','Linewidth',2)

```

```
hold on
plot(-y200,Bzy_ShapedReal,'c','Linewidth',2)
grid on, grid MINOR
title('Shaped vs ShapedReal along y')
xlabel('pNML length y [um]')
ylabel('Magnetic induction Bz [mT]')
legend('Shaped','ShapedReal','Location','best')
```

Material choice

```
clc
clear
close all

%%x component
xCoZrTa=readmatrix('Current.xlsx','Sheet',1,'Range','A2:A202');
xCoZrTa=xCoZrTa/1000;

xNiFe=readmatrix('Current.xlsx','Sheet',2,'Range','A2:A202');
xNiFe=xNiFe/1000;

xSPy=readmatrix('Current.xlsx','Sheet',3,'Range','A2:A202');
xSPy=xSPy/1000;

%%y component
yCoZrTa=real(readmatrix('Current.xlsx','Sheet',1,'Range','B2:B202'));

yNiFe=real(readmatrix('Current.xlsx','Sheet',2,'Range','B2:B202'));

ySPy=real(readmatrix('Current.xlsx','Sheet',3,'Range','B2:B202'));

figure(1)
plot(xCoZrTa,yCoZrTa,'b','Linewidth',2)
hold on
plot(xNiFe,yNiFe,'k','Linewidth',2)
hold on
plot(xSPy,ySPy,'g','Linewidth',2)
yline(-50,'-','Desired field','LineWidth',1,'LabelHorizontalAlignment','left')
title('Materials comparison')
xlim([39.5 60.5])
grid on, grid MINOR
xlabel('pNML width x [um]')
ylabel('Magnetic induction Bz [mT]')
legend('CoZrTa','NiFe','SPy','Location','best')
```

Parametric analysis

```

clc
clear
close all

%%x component
x44=readmatrix('SpacingWidth.xlsx','Sheet',1,'Range','A2:A172');
x44=x44/1000;

x46=readmatrix('SpacingWidth.xlsx','Sheet',2,'Range','A2:A182');
x46=x46/1000;

x48=readmatrix('SpacingWidth.xlsx','Sheet',3,'Range','A2:A192');
x48=x48/1000;

x50=readmatrix('SpacingWidth.xlsx','Sheet',4,'Range','A2:A202');
x50=x50/1000;

%%y component
y44=real(readmatrix('SpacingWidth.xlsx','Sheet',1,'Range','B2:B172'));
y46=real(readmatrix('SpacingWidth.xlsx','Sheet',2,'Range','B2:B182'));
y48=real(readmatrix('SpacingWidth.xlsx','Sheet',3,'Range','B2:B192'));
y50=real(readmatrix('SpacingWidth.xlsx','Sheet',4,'Range','B2:B202'));

figure(1)
plot(x44,y44,'b','Linewidth',2)
hold on
plot(x46,y46,'k','Linewidth',2)
hold on
plot(x48,y48,'g','Linewidth',2)
hold on
plot(x50,y50,'r','Linewidth',2)
yline(-49.5,'--','Lower limit Bz= -49.5 mT','LineWidth',2,'LabelHorizontalAlignment','left')
yline(-50.5,'--','Upper limit Bz= -50.5 mT','LineWidth',2,'LabelVerticalAlignment','bottom')
title('Widths comparison')
xlim([36.5 60.5])
grid on, grid MINOR
xlabel('pNML width x [um]')
ylabel('Magnetic induction Bz [mT]')
legend('44 um','46 um','48 um','50 um','Location','south')

```

Cell field

```
clc
clear
close all

%x component
x=readmatrix('VerticalArray_Structures.xlsx','Sheet',1,'Range','A2:A192');
x=x/1000;

Bzx=real(readmatrix('VerticalArray_Structures.xlsx','Sheet',1,'Range','B2:B192'));

%y component
y1=readmatrix('VerticalArray_Structures.xlsx','Sheet',1,'Range','C2:C10002');
y2=readmatrix('VerticalArray_Structures.xlsx','Sheet',1,'Range','C10003:C19002');
y3=readmatrix('VerticalArray_Structures.xlsx','Sheet',1,'Range','C19003:C20002');
y=[y1; y2/1000; y3/10000];

Bzy1=real(readmatrix('VerticalArray_Structures.xlsx','Sheet',1,'Range','D2:D10002'));
Bzy2=real(readmatrix('VerticalArray_Structures.xlsx','Sheet',1,'Range','D10003:D19002'));
Bzy3=real(readmatrix('VerticalArray_Structures.xlsx','Sheet',1,'Range','D19003:D20002'));
Bzy=[Bzy1; Bzy2; Bzy3];

figure(1)
plot(x,Bzx,'b','Linewidth',2)
title('Cell along x')
grid on, grid MINOR
xlim([38.5 58.5])
ylim([-51 -49])
xlabel('pNML width x [um]')
ylabel('Magnetic induction Bz [mT]')

figure(2)
plot(-y,Bzy,'b','Linewidth',2)
title('Cell along y')
grid on, grid MINOR
xlim([-205 5])
xlabel('pNML length y [um]')
ylabel('Magnetic induction Bz [mT]')
```

Two wires array

```

clc
clear
close all

%y component
yBottom1=readmatrix('TwoWires.xlsx','Sheet',1,'Range','A2:A10002');
yBottom2=readmatrix('TwoWires.xlsx','Sheet',1,'Range','A10003:A19002');
yBottom3=readmatrix('TwoWires.xlsx','Sheet',1,'Range','A19003:A19902');
yBottom4=readmatrix('TwoWires.xlsx','Sheet',1,'Range','A19903:A20101');
yBottom5=readmatrix('TwoWires.xlsx','Sheet',1,'Range','A20102:A21001');
yBottom6=readmatrix('TwoWires.xlsx','Sheet',1,'Range','A21002:A25587');
yBottom=[yBottom1; yBottom2/1000; yBottom3/10000; yBottom4; yBottom5/10000; yBottom6/1000];

Bzy_Bottom=real(readmatrix('TwoWires.xlsx','Sheet',1,'Range','B2:B25587'));

yTop1=readmatrix('TwoWires.xlsx','Sheet',2,'Range','A2:A15587');
yTop2=readmatrix('TwoWires.xlsx','Sheet',2,'Range','A15588:A24587');
yTop3=readmatrix('TwoWires.xlsx','Sheet',2,'Range','A24588:A25587');
yTop=[yTop1; yTop2/1000; yTop3/10000];

Bzy_Top=real(readmatrix('TwoWires.xlsx','Sheet',2,'Range','B2:B25587'));

figure(1)
plot(-yBottom,Bzy_Bottom,'b','Linewidth',2)
title('Horizontal Array with bottom wire')
grid on, grid MINOR
xlim([-205 60.85])
xlabel('pNML length y [um]')
ylabel('Magnetic induction Bz [mT]')

figure(2)
plot(-yTop,Bzy_Top,'r','Linewidth',2)
title('Horizontal Array with top wire')
grid on, grid MINOR
xlim([-260.9 5])
xlabel('pNML length y [um]')
ylabel('Magnetic induction Bz [mT]')

```

Array structures

The code is written so that from the main the structures are chosen and one function plots the fields and the values for the comparison, therefore the code is one for both the array types.

```
clc
clear
close all

%Choose the type of array: Horizontal or Vertical
array='Vertical';

%For Horizontal
%Choose up to 3 types of structures:
%OneWire, ThreeWires, ThreeWiresSuperDense, FiveWires

%For Vertical
%Choose up to 3 types of structures:
%OneWire, FlatCladding, NormalCladding, ShapedCladding, ShapedCladding4Wires,
%SuperShapedCladding, SuperShapedCladding4Wires, SuperShapedCladding4WiresEco

struc1='OneWire';
struc2='';
struc3='';

StructuresComparison(array, struc1, struc2, struc3)
```

Frequency and cladding

```

clc
clear
close all

%%x component
x=readmatrix('Frequency_tcl1.xlsx','Sheet',8,'Range','A2:A192');
x=x/1000;

Bzx_3001=real(readmatrix('Frequency_tcl1.xlsx','Sheet',8,'Range','B2:B192'));
Bzx_30005=real(readmatrix('Frequency_tcl05.xlsx','Sheet',8,'Range','B2:B192'));
Bzx_300025=real(readmatrix('Frequency_tcl025.xlsx','Sheet',8,'Range','B2:B192'));
Bzx_3000125=real(readmatrix('Frequency_tcl0125.xlsx','Sheet',8,'Range','B2:B192'));

%%y component
y1=real(readmatrix('Frequency_tcl1.xlsx','Sheet',8,'Range','C2:C10002'));
y2=real(readmatrix('Frequency_tcl1.xlsx','Sheet',8,'Range','C10003:C19002'));
y3=real(readmatrix('Frequency_tcl1.xlsx','Sheet',8,'Range','C19003:C20002'));
y=[y1; y2/1000; y3/10000];

Bzy_30011p=real(readmatrix('Frequency_tcl1.xlsx','Sheet',8,'Range','D2:D10002'));
Bzy_30012p=real(readmatrix('Frequency_tcl1.xlsx','Sheet',8,'Range','D10003:D19002'));
Bzy_30013p=real(readmatrix('Frequency_tcl1.xlsx','Sheet',8,'Range','D19003:D20002'));
Bzy_3001=[Bzy_30011p; Bzy_30012p; Bzy_30013p];

Bzy_300051p=real(readmatrix('Frequency_tcl05.xlsx','Sheet',8,'Range','D2:D10002'));
Bzy_300052p=real(readmatrix('Frequency_tcl05.xlsx','Sheet',8,'Range','D10003:D19002'));
Bzy_300053p=real(readmatrix('Frequency_tcl05.xlsx','Sheet',8,'Range','D19003:D20002'));
Bzy_30005=[Bzy_300051p; Bzy_300052p; Bzy_300053p];

Bzy_3000251p=real(readmatrix('Frequency_tcl025.xlsx','Sheet',8,'Range','D2:D10002'));
Bzy_3000252p=real(readmatrix('Frequency_tcl025.xlsx','Sheet',8,'Range','D10003:D19002'));
Bzy_3000253p=real(readmatrix('Frequency_tcl025.xlsx','Sheet',8,'Range','D19003:D20002'));
Bzy_300025=[Bzy_3000251p; Bzy_3000252p; Bzy_3000253p];

Bzy_30001251p=real(readmatrix('Frequency_tcl0125.xlsx','Sheet',8,'Range','D2:D10002'));
Bzy_30001252p=real(readmatrix('Frequency_tcl0125.xlsx','Sheet',8,'Range','D10003:D19002'));
Bzy_30001253p=real(readmatrix('Frequency_tcl0125.xlsx','Sheet',8,'Range','D19003:D20002'));
Bzy_3000125=[Bzy_30001251p; Bzy_30001252p; Bzy_30001253p];

figure(1)
plot(x,Bzx_3001,'k','Linewidth',2)
hold on
plot(x,Bzx_30005,'g','Linewidth',2)
hold on
plot(x,Bzx_300025,'r','Linewidth',2)
hold on
plot(x,Bzx_3000125,'c','Linewidth',2)
title('Cladding thicknesses comparison with fixed field at 300 MHz along x')
xlim([38.5 58.5])
grid on, grid MINOR
xlabel('pNML width x [um]')
ylabel('Magnetic induction Bz [mT]')
legend('1 um with 0.83*i0','0.5 um with 0.64*i0','0.25 um with 0.55*i0',...
      '0.125 um with 0.55*i0','Location','best')

```

```

figure(2)
plot(-y,Bzy_3001,'k','Linewidth',2)
hold on
plot(-y,Bzy_30005,'g','Linewidth',2)
hold on
plot(-y,Bzy_300025,'r','Linewidth',2)
hold on
plot(-y,Bzy_3000125,'c','Linewidth',2)
title('Cladding thicknesses comparison with fixed field at 300 MHz along y')
ylim([-90 25])
grid on, grid MINOR
xlabel('pNML length y [um]')
ylabel('Magnetic induction Bz [mT]')
legend('1 um with 0.83*i0','0.5 um with 0.64*i0','0.25 um with 0.55*i0',...
       '0.125 um with 0.55*i0','Location','north')

disp('Cladding thickness t_cl=1 um')
disp(' ')
Area=readmatrix('Frequency_tcl1.xlsx','Sheet',8,'Range','E2:E2');
disp(['The available area of pNML is ',num2str(Area),' um^2'])
disp(' ')
Power=readmatrix('Frequency_tcl1.xlsx','Sheet',8,'Range','F2:F2');
Power_density=Power/Area;
disp(['The dissipated power density is ',num2str(Power_density),' uW/um^2'])
disp('-----')

disp('Cladding thickness t_cl=0.5 um')
disp(' ')
Area=readmatrix('Frequency_tcl05.xlsx','Sheet',8,'Range','E2:E2');
disp(['The available area of pNML is ',num2str(Area),' um^2'])
disp(' ')
Power=readmatrix('Frequency_tcl05.xlsx','Sheet',8,'Range','F2:F2');
Power_density=Power/Area;
disp(['The dissipated power density is ',num2str(Power_density),' uW/um^2'])
disp('-----')

disp('Cladding thickness t_cl=0.25 um')
disp(' ')
Area=readmatrix('Frequency_tcl025.xlsx','Sheet',8,'Range','E2:E2');
disp(['The available area of pNML is ',num2str(Area),' um^2'])
disp(' ')
Power=readmatrix('Frequency_tcl025.xlsx','Sheet',8,'Range','F2:F2');
Power_density=Power/Area;
disp(['The dissipated power density is ',num2str(Power_density),' uW/um^2'])
disp('-----')

disp('Cladding thickness t_cl=0.125 um')
disp(' ')
Area=readmatrix('Frequency_tcl0125.xlsx','Sheet',8,'Range','E2:E2');
disp(['The available area of pNML is ',num2str(Area),' um^2'])
disp(' ')
Power=readmatrix('Frequency_tcl0125.xlsx','Sheet',8,'Range','F2:F2');
Power_density=Power/Area;
disp(['The dissipated power density is ',num2str(Power_density),' uW/um^2'])
disp('-----')

```